Neutronic Characterization of a Molybdenum-99-Producing CANDU Fuel Bundle and Implications for Reactivity-Device Worth and Refuelling Strategies

by

Jawad Haroon

A thesis submitted to the
School of Graduate and Postdoctoral Studies in partial
fulfillment of the requirements for the degree of

Doctor of Philosophy in Nuclear Engineering

Faculty of Engineering & Applied Science

University of Ontario Institute of Technology (Ontario Tech University)

Oshawa, Ontario, Canada

August 2023

THESIS EXAMINATION INFORMATION

Submitted by: **Jawad Haroon**

Doctor of Philosophy in Nuclear Engineering

Thesis title:

Neutronic Characterization of a Molybdenum-99-Producing CANDU Fuel Bundle and Implications for Reactivity-Device Worth and Refuelling Strategies

An oral defense of this thesis took place on July 19, 2023 in front of the following examining committee:

Examining Committee:

Chair of Examining Committee	Dr. Jennifer McKellar
Research Supervisor	Dr. Eleodor Nichita
Examining Committee Member	Dr. Igor Pioro
Examining Committee Member	Dr. Benjamin Rouben
University Examiner	Dr. Markus Piro
External Examiner	Dr. Adriaan Buijs

The above committee determined that the thesis is acceptable in form and content and that a satisfactory knowledge of the field covered by the thesis was demonstrated by the candidate during an oral examination. A signed copy of the Certificate of Approval is available from the School of Graduate and Postdoctoral Studies.

ABSTRACT

Operating CANDU reactors can potentially produce significant quantities of Molybdenum-99 due to their ability to be refuelled online, high thermal neutron flux and fuel-design flexibility. A *Molybdenum-producing bundle* (MPB) has previously been designed for that purpose and shown to be equivalent to the standard CANDU bundle (SCB) under normal, steady-state, conditions. However, before an MPB can be employed inside a CANDU reactor, steady-state characterization of MPB needs to be supplemented by additional neutronic evaluations.

This study therefore evaluates the neutronic characteristics of the MPB relevant to transient behaviour and refuelling, and compares the results to those of the SCB. This includes derivation of reactivity coefficients, incremental macroscopic cross sections for reactivity devices and refuelling strategies for the MPB. The evaluations are made using well-established analysis methods and models where applicable, and new or improved methods and models are developed and used where necessary. In particular, a perturbation-theory approach is employed for evaluating the differences between the reactivity coefficients of the MPB and the SCB, and high-resolution 2D and 3D supercell lattice models are developed in the neutron transport code DRAGON. The high-resolution lattice models incorporate a large number of spatial and spectral subdivisions and account for the radial variation of fuel temperature.

The study of the reactivity feedback effects shows that the MPB and the SCB have almost identical (within 1.5 mk) reactivity feedback when key reactor parameters are perturbed over wide ranges. The study of the reactivity device incremental cross sections for CANDU reactivity devices shows that these cross sections are very similar for MPB and SCB with a maximum difference of less than 2% for any given device. At the same time, this study finds that the 3D supercell model currently used in the industry underestimates the reactivity worth of adjuster and shutoff rods by 7%-11%.

Finally, a full-core 3D model is constructed in the diffusion code DONJON and a fuelling strategy for achieving the desired weekly yield of Molybdenum-99 is developed. The adequacy of the proposed refuelling scheme is evaluated using a series of time-average calculations, which show that a small increase in the core reactivity (< 0.4 mk) results from employing a set of 4 MPBs in three different fuel channels in the inner region of the core. The small increase in the core reactivity can be managed by slightly increasing the discharge burnup in the non-MPB-bearing fuel channels, thus also improving slightly the fuel utilization in the reactor.

Keywords: molybdenum-producing bundle; reactivity coefficients; incremental macroscopic cross section; supercell; neutron transport; diffusion; time-average calculation

AUTHOR'S DECLARATION

I hereby declare that this thesis consists of original work of which I have authored or co-authored: see Statement of Contributions included in the thesis. This is a true copy of the thesis, including any required final revisions, as accepted by my examiners.

I authorize the University of Ontario Institute of Technology (Ontario Tech University) to lend this thesis to other institutions or individuals for the purpose of scholarly research. I further authorize University of Ontario Institute of Technology (Ontario Tech University) to reproduce this thesis by photocopying or by other means, in total or in part, at the request of other institutions or individuals for the purpose of scholarly research. I understand that my thesis will be made electronically available to the public.

Jawad Haroon

STATEMENT OF CONTRIBUTIONS

The form of the doctoral dissertation presentation used herein is that of a standard monograph as accepted by the Faculty of Engineering and Applied Science.

Findings from this dissertation research are reported in three co-authored journal and conference papers (chapters Four, Five, and Six). Content of Chapter 4 and Chapter 5 has been previously published in peered-reviewed journals. Content of Chapter 6 has been published in a refereed conference proceeding.

Co-author and Research Advisor, Dr. E. Nichita, conceptualized the original idea for a novel fuel design for molybdenum production. The introductory work describing the new molybdenum-producing bundle was published as:

E. Nichita, J. Haroon, "Molybdenum-99-Producing 37-Element Fuel Bundle Neutronically and Thermal-Hydraulically Equivalent to a Standard CANDU Fuel Bundle," Nuclear Engineering and Design, vol. 307 (2016), pp. 86-95. doi.org/10.1016/j.nucengdes.2016.06.036

It bears mentioning that research conducted for this paper was performed prior to commencing of the author's PhD program. The author performed the majority of the ground investigation, simulation preparation, simulation execution, analysis and writing of the manuscript. Limited content from the above publication has been included in this dissertation solely for information purposes.

Content of the paper introduces the new fuel bundle design which undergoes further neutronic evaluations in this dissertation. The paper provides a foundation to

the overall neutronic assessment performed herein and is integral to form a coherent dissertation.

The work described in Chapter 4 has been published as:

J. Haroon, E. Nichita, "A comparative study of reactivity feedback effects for a HALEU molybdenum-producing PHWR fuel bundle and a standard PHWR fuel bundle," Nuclear Engineering and Design, vol 361 (2020) 110545. doi.org/10.1016/j.nucengdes.2020.110545

The work described in Chapter 5 has been published as:

J. Haroon, E. Nichita, "PHWR-Reactivity-Device Incremental Macroscopic Cross Sections and Reactivities for a Molybdenum-Producing Bundle and a Standard Bundle," Nuclear Technology, Nuclear Technology, vol 208 (2022), pp 246-267.

doi.org/10.1080/00295450.2021.1929768

The work described in Chapter 6 has been published as:

J. Haroon, E. Nichita, "Preliminary Refuelling Considerations for Molybdenum Production in a Pressurized Heavy Water Reactor," Proceedings of the American Nuclear Society Annual Meeting, vol. 126 (2022), pp. 704-707.

I testify that I am the primary author of the manuscripts in my dissertation, and that the work was dominated by my intellectual efforts.

Jawad Haroon

ACKNOWLEDGEMENTS

First and foremost, I would like to express my sincere gratitude to my research supervisor, Dr. Eleodor Nichita, for his steadfast support throughout my graduate studies. His extensive knowledge and expertise have been indispensable in shaping my research. His constructive feedback and suggestions have helped me improve my research work and have guided me towards new avenues of analysis.

I am also deeply grateful for Dr. Nichita's support in granting numerous developmental opportunities throughout my graduate studies. Most notably of which was the opportunity to attend the World Nuclear University's Summer Institute in Sweden for six weeks. The program helped me develop the critical skills needed for effective leadership and strategic decision-making, as well as extended my understanding of issues affecting the nuclear industry from a global perspective. A massive 'thank you' to Dr. Akira Tokuhiro, who was instrumental in arranging the financial means to attend this program.

In addition, I am grateful for the unconditional support that I have received from my entire family, especially my parents. Their unwavering belief in my abilities and their encouragement have been a source of constant motivation during many challenging phases. They have always been available to offer their 'non-technical' yet much needed advice and encouragement.

Finally, I want to acknowledge the support of my wife, who has been a pillar of strength throughout my graduate studies. Her steadfast support, encouragement, and

understanding have helped me balance my personal, professional and academic lives. Thank you for the countless hours you spent proofreading my manuscripts.

I also want to thank my wife profusely for giving us the most precious gift of all – our beautiful daughter. Throughout the challenges of balancing parenthood and graduate studies, she has shown tremendous strength, love, and care for our little one. Her tireless efforts in raising our daughter and supporting me in my professional career and academic pursuits, all while trailblazing through her own professional journey, have been nothing short of remarkable. I am eternally grateful for her devotion to our family and the joy that our daughter has brought to our lives.

Dedicated to my mother, **Sarwat Siddiqa**, and my father, **Haroon-ur-Rashid**. Your love, support, and encouragement during my formative years instilled in me the drive and determination to pursue my academic aspirations and many other life endeavours.

Dedicated to the loving memory of my brother, **Waqas Haroon**, who passed away in a tragic accident at the onset of my undergraduate studies. Although you are no longer with us, big brother and childhood roommate, you have been with me every step of the way and I will forever cherish the invaluable childhood lessons you imparted. I am grateful for the time we had together, and I will always hold your memories dear to my heart.

TABLE OF CONTENTS

LIST OF TABLES

LIST OF FIGURES

LIST OF ABBREVIATIONS

AA	Adjuster Absorbers
ACR	Advanced CANDU Reactor
AECL	Atomic Energy of Canada Limited
CANDU	CANada Deuterium Uranium
CP	Collision Probabilities
DU	Depleted Uranium
DUPIC	Direct Use of spent PWR fuel In CANDU
FEAS	Faculty of Engineering and Applied Science
ENDF	Evaluated Nuclear Data File
HALEU	High-Assay Low Enriched Uranium
HEU	Highly-Enriched Uranium
HFR	High Flux Reactor
IAEA	International Atomic Energy Agency
IST	Industry Standard Toolset
JEFF	Joint Evaluated Fission and Fusion
LEU	Low-Enriched Uranium
LVRF	Low Void Reactivity Fuels
LWR	Light Water Reactor
LZC	Liquid Zone Controllers
MOC	Method of Characteristics
MOX	Mixed Oxide Fuel
MPB	Molybdenum-Producing Bundle
NRU	National Research Universal
NU	Natural Uranium
NUE	Natural Uranium Equivalent
OPAL	Open Pool Australian Light-Water Reactor
RFSP	Reactor Fuelling Simulation Program

RU	Recovered-Uranium
SA	Shutoff Absorbers
SCB	Standard CANDU Bundle
SEU	Slightly Enriched Uranium
SS	Stainless Steel
TRUMOX	Transuranic Mixed Oxide Fuel
WIMS	Winfrith Improved Multigroup Scheme
WLUP	WIMS-D Library Update Project
ZED	Zero Energy Deuterium

LIST OF SYMBOLS

r	Position vector
$\mathbf{v}_n$	Velocity vector
$\mathbf{\Omega}$	Direction unit vector
J	Neutron current
n	Neutron density
N	Neucli density
t	Time
ϕ	Flux
ϕ^*	Adjoint
σ	Microscopic cross section
Σ	Macroscopic cross section
x	Reaction type
Σ_x	Macroscopic cross section for reaction x
E	Energy
∇	Divergence operator
∞	Infinity limit
Q	Source term
Q^*	Adjoint source term
m	Neutron mass
χ	Fission spectrum
ν	Neutrons per fission event
k	Multiplication factor
k_{eff}	Effective multiplication factor
k_{inf}	Infinite multiplication factor
μ	Lethargy
G	Total number of energy groups
V	Volume

$N(r_s)$	Normal vector
γ	Gamma photons
D_g	Diffusion coefficient for group g
α	Albedo factor
ρ	Reactivity
$\Delta\rho$	Reactivity change
ω	Fuel irradiation
$P(t)$	Amplitude function
ψ	Factorized flux
w	Weighting vector
p	Lattice parameter
ε	Fast fission factor
$\wp$	Resonance escape probability
f	Thermal utilization factor
η	Thermal reproduction factor
δ	Perturbation delta
$\delta_{g,g'}$	Kronecker delta
D	Density
T	Temperature
C	Poison concentration
$\overline{R}$	Refuelling frequency
N_p	Number of channels in a pool

Chapter 1: Introduction

1.1 Preamble

Nuclear medicine uses the radiation emitted from unstable nuclei to study the function of specific organs in the body. In diagnostic nuclear medicine, a radiopharmaceutical consisting of radioisotope bound to a substrate is administered to a patient. The substrate is what controls the distribution of the radiopharmaceutical in the body and is chosen such that it is predominantly accumulated in the organ of interest. The amount of accumulation in the specific organ gives information about the health and function of the organ. The gamma-emitting radioactive isotope is what allows the distribution of the radiopharmaceutical to be visualized using an external detection device (e.g., gamma camera) which produces a diagnostic image. Images are then analyzed to detect partial or excessive absorption of the isotope as an indication of organ malfunction.

Medical isotopes are used routinely in the diagnosis and treatment of various diseases at hospitals and radiation clinics. Some of the health conditions where various medical isotopes are used for monitoring and evaluation, reproduced from [1], are listed below:

- Heart disease
- Level of functioning of brain, lungs, kidneys and other organs
- Tumours
- Progression of cancer particularly when spreading to bones

- Hormonal disorders, e.g., thyroid disease

The most commonly used radioisotope in diagnostic nuclear medicine is technetium-99m (^{99m}Tc), which is produced from the radioactive decay of molybdenum-99 (^{99}Mo). ^{99m}Tc is used in approximately 30 million procedures per year, accounting for 80% of all nuclear medicine procedures worldwide [1]. ^{99m}Tc is an ideal radioisotope for diagnostic nuclear medicine because of its physical and chemical properties. ^{99m}Tc decays by isomeric transition to its ground state ^{99}Tc. The 6.01-hour half-life of ^{99m}Tc is neither too long nor too short for a medical procedure. The principal gamma-emission associated with the transition from the meta-stable state to the ground state emits a 140-keV photon that is energetic enough to pass through the human body without significant attenuation, thus keeping the total dose administered to patients low. Its parent radionuclide, ^{99}Mo, has a 66-hour half-life which provides sufficient time for processing and long-distance transportation, and thus permits shipping under the form of a ^{99}Mo /^{99m}Tc generator. Conversely, due to its short half-life, ^{99m}Tc cannot be stockpiled or produced directly in nuclear reactors or through neutron activation as a final product.

^{99}Mo is most commonly and efficiently generated in a nuclear reactor from the fission of uranium-235 (^{235}U) with a fission yield of 6.1% [2]. The reaction shown in Eq. (1.1) corresponds to the production of ^{99}Mo from the fission of ^{235}U, which occurs for approximately 6.1% of all fission reactions. ^{99}Mo is formed from the nuclear fission and consequently exists as a fission by-product in the uranium fuel matrix.

$$^{235}_{92}U + n \rightarrow \, ^{99}_{42}Mo + \, ^{133}_{50}Sn + 4n \quad\quad\quad (1.1)$$

1.2 Problem Statement

As mentioned, ^{99m}Tc is the most widely used radiopharmaceutical in diagnostic nuclear medicine. Over the last decade, there have been a number of supply shortages of ^{99}Mo. The situation has deteriorated further with the permanent shutdown of the French OSIRIS reactor in 2015 and the Canadian National Research Universal (NRU) reactor in 2018.

CANDU (<u>CAN</u>ada <u>D</u>euterium <u>U</u>ranium) reactors, the majority of which are operating in Canada, can potentially play a large role in ensuring a stable supply of ^{99}Mo. The ability to refuel online and a good thermal neutron economy in the core give CANDUs a unique advantage in terms of producing and harvesting significant quantities of ^{99}Mo to meet the global demand of medical isotopes.

Researchers at Ontario Tech University have proposed a new 37-element fuel bundle where each fuel pin is radially separated into two regions, one consisting of enriched uranium fuel and another consisting of depleted uranium fuel [3]. This modified 37-element fuel bundle is referred to in this dissertation as the 'Molybdenum Producing Bundle' or 'MPB' and the standard CANDU fuel bundle is referred to as 'SCB'.

The new MPB has been optimized to be neutronically and thermal-hydraulically equivalent to the SCB for steady-state scenarios. Overall, the study in Reference [3] demonstrated that the MPB and the SCB are neutronically and thermal-hydraulically equivalent under normal, steady state, conditions. Consequently, for normal,

steady-state operation, the adoption of the proposed MPB is expected to require only few, mostly confirmatory, supplemental analyses.

However, steady state characterization of MPB is not sufficient and additional neutronic investigations are needed before an MPB can be employed in a CANDU reactor. The behaviour of the proposed MPB design under transient conditions, including possible similarity to the SCB behaviour, requires additional evaluations. This includes derivation of reactivity coefficients, incremental reactivity device worths and refuelling strategies for the new bundle.

1.3 Research Objective

The objective of this work is to evaluate the neutronic characteristics of the new MPB design relevant to transient behaviour and refuelling and compare them to those of the SCB. When appropriate, the evaluations are to be made using well-established analysis methods and simulation schemes used in the industry. Additionally, when desirable, the existing methodology and models are to be improved to make them more appropriate for the bundle under study.

1.4 Research Scope

The main research areas covered by this study are:

- Study of the MPB reactivity feedback effects for fuel temperature, coolant temperature, moderator temperature, coolant density, moderator density and

moderator poison concentration, and comparison with their respective counterparts for the SCB

- Application of linear perturbation theory to better understand reactivity feedback effects

- Study of the MPB reactivity-device incremental macroscopic cross sections and comparison with their respective counterparts for the SCB

- Development of a detailed lattice model incorporating a high number of spatial and spectral subdivisions and variation of radial fuel pin temperatures and study of its effect on reactivity feedback effects and incremental reactivity device macroscopic cross sections

- Comparison of fully explicit and stylized 3D supercell lattice models

- Study of refuelling features of a core partially fuelled with MPBs and development of a feasible fuelling scheme based on a full-core time average model

1.5 Organization of Thesis

Chapter 2 provides the theoretical background necessary for the presentation of the performed work, as well as the description of the MPB. Chapter 3 provides a literature review which covers both ^{99}Mo production methods and advances in analysis of lattice and core properties for advanced CANDU fuels, since the MPB is an example of such advanced fuel.

Chapters 4, 5 and 6 cover the performed research, corresponding to the three main areas of work. Each area covers a segment of research work typically conducted for advanced fuel developments. The consolidated whole ensures the comprehensiveness of the research work and reflects a consistent overall foundation supporting the feasibility of the MPB in a manner consistent with standard industry practices.

The multi-phase analysis begins in Chapter 4 with presenting the neutronic characterization of the MPB and its counterpart, the SCB, by looking at additional bundle neutronics beyond what has been presented in Reference [3], which mainly looked at geometries, the fuel composition, lattice reactivity and average two-group macroscopic cross sections. Chapter 4 compares the reactivity effects of the two bundles over a wide range of perturbations in coolant density, moderator density, coolant temperature, moderator temperature, fuel temperature and moderator poison concentration (boron and gadolinium), for burnups ranging from zero to discharge burnup. For each reactivity feedback effect calculation, the subject parameter under consideration is perturbed over a range of values around its reference, operating conditions, and at specified intervals.

The preliminary assessment of the fuel pin radial temperatures between the two fuel types was calculated and found to be significantly different. Therefore, the models used for assessment employ a high-resolution lattice model incorporating the distributed fuel pin temperature for more accurate predictions of the reactivity

coefficient. The same methodology for high resolution models is used later in Chapter 5 for calculating incremental macroscopic cross sections.

A detailed explanation of reactivity feedback effects using the linear perturbation theory is also presented in Chapter 4.

Chapter 5 builds on Reference [3] to develop a full set of burnup-dependent incremental macroscopic lattice cross sections for reactivity devices in the vicinity of both standard and modified fuel bundles. The homogenized incremental cross sections for the two bundles are calculated at zero burnup and 20-day burnup, which corresponds to the maximum residence time of the MPB inside the core.

In this chapter, the single lattice transport models are advanced to produce 3D super-cell type configurations in order to determine the incremental effect of the interaction of reactor control devices on the lattice cell cross sections. Two geometrical representations of fuel bundles are used: a detailed, cluster, representation, whereby all fuel pins are modelled explicitly, and a stylized annular representation, whereby each ring of fuel pins and corresponding coolant is represented as a homogeneous annulus. The latter model is the one customarily used in production calculations for finding cross-section increments for reactivity devices.

Chapter 6 involves a three-dimensional, two group neutron diffusion code that is used to model the full core of a CANDU reactor with all relevant structures, devices and geometry. The full set of burnup-dependent homogenized macroscopic lattice cross sections are incorporated as building blocks to this full-core reactor model. The full-core model uses a detailed 3D representation of an existing CANDU-6 reactor

design in all of its specifications, operational parameters and safety limits. This full-core model partially fuelled with ^{99}Mo producing bundles is used to determine a 'modified' time-average configuration and properties at each bundle location in the core accounting for the short residence time of the MPB in the core.

The time-average calculations employing MPBs in a small number of fuel channels are used to define a suitable fuelling strategy that is appropriate for achieving the desired ^{99}Mo yield while ensuring that core reactivity, channel powers and flux profiles are maintained within the reference operational envelope.

Chapter 2:   Background

2.1 Overview of Methodology for Neutronics Core Analysis

2.1.1 The Particle Flux

In a reactor, each particle is defined by a set of seven variables. These quantities are:

- Three position co-ordinates: $\mathbf{r} = x\mathbf{i} + y\mathbf{j} + z\mathbf{k}$

- Three velocity co-ordinates: the velocity magnitude (speed) $v_n = |\mathbf{v_n}|$ and the two independent components of the direction $\mathbf{\Omega} = \frac{\mathbf{v_n}}{|v_n|}$

- The time: t

The neutron population is described by its density $n(\mathbf{r}, v_n, \mathbf{\Omega}, t)$ where $n(\mathbf{r}, v_n, \mathbf{\Omega}, t)d^3r dv_n d^2\Omega$ is the number of particles at time t, in the volume element d^3r surrounding $\mathbf{r}$, in the velocity element dv_n surrounding $\mathbf{v_n}$ and in the solid angle $d^2\Omega$ surrounding $\mathbf{\Omega}$. From this definition, we can introduce the particle angular flux as:

$$\phi(\mathbf{r}, v_n, \mathbf{\Omega}, t) = v_n \, n(\mathbf{r}, v_n, \mathbf{\Omega}, t) \tag{2.1}$$

In many applications, knowing the angular dependence is not important so the flux distribution can be reduced by integrating Eq. (2.1) to get the integrated flux as:

$$\phi(\boldsymbol{r}, v_n, t) = \int_{4\pi} d^2\Omega \phi(\boldsymbol{r}, v_n, \boldsymbol{\Omega}, t) \tag{2.2}$$

Another fundamental quantity is the angular current. The current is a distribution defined as:

$$\boldsymbol{J}(\boldsymbol{r}, v_n, \boldsymbol{\Omega}, t) = \boldsymbol{\Omega}\, \phi(\boldsymbol{r}, v_n, \boldsymbol{\Omega}, t) \tag{2.3}$$

In a similar manner to flux, the angular current is integrated to dispose of the angular dependence in Eq.(2.3).

$$\boldsymbol{J}(\boldsymbol{r}, v_n, t) = \int_{4\pi} d^2\Omega\, \boldsymbol{J}(\boldsymbol{r}, v_n, \boldsymbol{\Omega}, t) = \int_{4\pi} d^2\Omega\, \boldsymbol{\Omega}\, \phi(\boldsymbol{r}, v_n, \boldsymbol{\Omega}, t) \tag{2.4}$$

2.1.2 Cross Sections and Reaction Rates

When fission of ^{235}U nuclei occurs, prompt high-energy neutrons are emitted. In thermal reactors, in order to take advantage of the higher neutron-nuclear interaction probability, these neutrons are moderated to energies of less than 1 eV. This neutron-nuclear interaction probability is known as 'cross-section' and is measured in units of barns (1b = 10^{-24} cm^2) and is dependent on incident neutron energy.

We can define the macroscopic cross sections of a reaction x for isotope i with a number density, N_i, given in target nuclei per unit volume:

$$\Sigma_{x,i}(E) = \sigma_{x,i}(E)N_i \tag{2.5}$$

For a material composed of different isotopes, the resulting macroscopic cross section is:

$$\Sigma_x(E) = \sum_i \Sigma_{x,i}(E) \tag{2.6}$$

The total macroscopic cross section of a region taking into account all nuclear reactions is:

$$\Sigma(E) = \sum_x \Sigma_x(E) \tag{2.7}$$

Neutron cross sections are used to characterize the neutron-nuclide interaction at different neutron energies, which occurs when a neutron collides with a nucleus. The most important of all neutron-nuclide interactions in reactor physics is the interaction resulting in fission of the target nuclide. Figure 2-1 and Figure 2-2 show the energy-dependent fission cross sections for the two most important fissile isotopes in nuclear reactor fuel, which are ^{235}U and plutonium-239 (^{239}Pu), respectively.

Knowledge of neutron-nuclide cross section, nuclide density, neutron population and neutron velocity lead to determining neutron reaction rates.
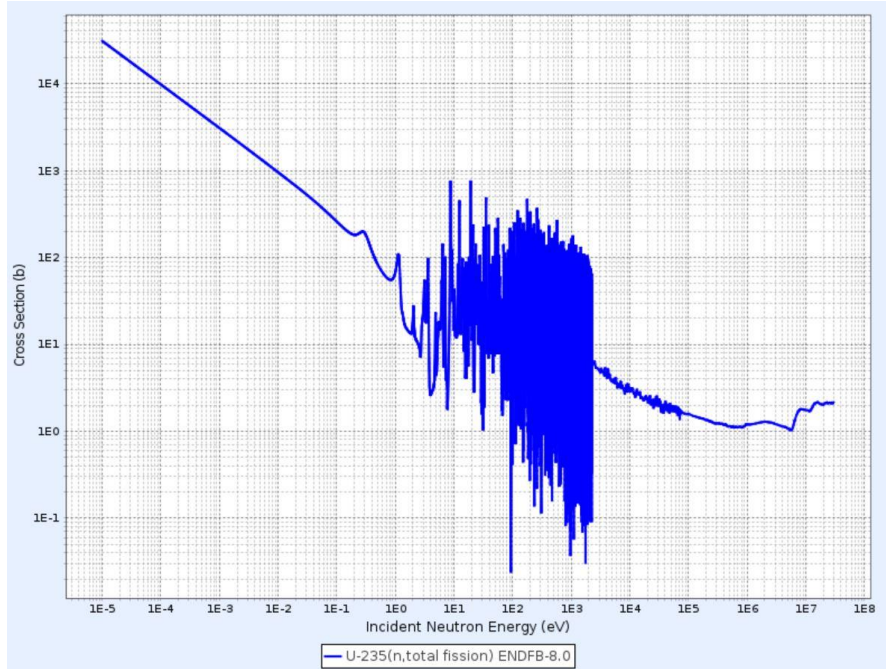
Figure 2-1: Neutron fission cross section for ^{235}U [4]
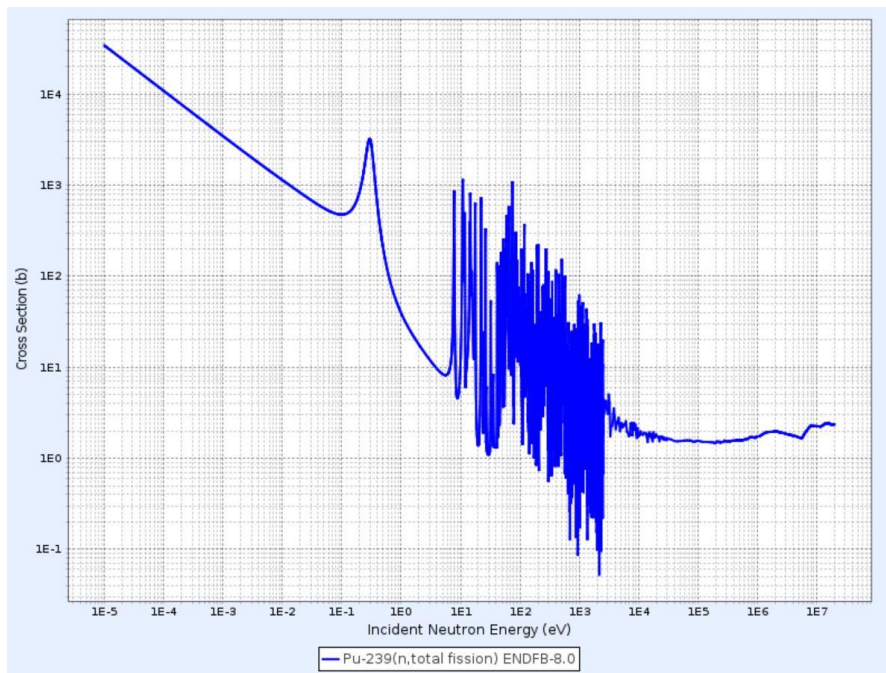
Figure 2-2: Neutron fission cross section for ^{239}Pu [4]

2.1.3 CANDU Neutronics Calculations

CANDU reactors are pressurized heavy water reactors using heavy water as coolant and moderator and natural uranium as fuel. The moderator is contained in a large horizontal cylindrical tank called the calandria. The calandria is penetrated by hundreds of horizontal fuel channels which contain natural uranium oxide fuel in the form of fuel bundles.

The basic building block of a CANDU pressure tube type reactor is the fuel channel. The fuel channels are arranged in a rectangular lattice with a lattice pitch of 28.575 cm. Since there is a repeating array of these assemblies throughout the core, the fundamental neutronic characteristics can be determined by considering only one channel surrounded by the appropriate volume of heavy water moderator. This constitutes the 'lattice cell'. A lattice cell is thereby a small section of the reactor that can be translated multiple times in order to produce a full reactor core. The neutronic characteristics of a lattice cell are called lattice parameters. A lattice cell is typically analyzed using the multigroup transport equation with specular reflective boundary conditions.

A CANDU reactor core is most commonly analyzed in a full-core representation of the reactor using a neutron diffusion code that derives its few-group homogenized macroscopic cross-sections from two-dimensional (2D) lattice cell calculations. Reactivity devices are modelled using macroscopic cross-section increments based on a few-neutron energy groups, which are added to the lattice-homogenized macroscopic cross-sections in the volumetric representations that include reactivity

devices. The macroscopic cross-section increments are determined from three-dimensional (3D) supercell calculations using the multigroup transport equation. The full set of macroscopic cross sections required to solve the neutron diffusion equation for a full-core CANDU model are depicted in the computational scheme in Figure 2-3.

Use of a 2D single lattice-cell transport calculations for bare-lattice cross sections generation

Use of a 3D supercell transport calculation for macroscopic cross section increments for reactivity devices located between fuel channels and perpendicular to reactor axis

Use of the cross-section increments and bare lattice few group cross sections for appropriate burnup values as building blocks to construct a full-core neutron-diffusion model

Figure 2-3: Standard computational scheme

2.1.4 Lattice Calculations

A lattice calculation is a collection of numerical algorithms and models capable of representing the neutronic behaviour of a unit cell. For CANDU, a unit cell is the lattice cell that contains explicit representation of all fuel pins arranged in concentric rings contained within a coolant region surrounded by a pressure tube, an annulus gas gap, a calandria tube and a rectangular area of moderator.

The lattice calculation provides neutronic properties of the fuel channel. One aspect of lattice calculations is determination of the many-group neutron flux. In addition to the flux, the lattice calculations can provide information on variation of cross sections and isotopic compositions with fuel burnup, the lattice reactivity coefficients, the power distribution across the fuel bundle, and the set of fewer group macroscopic cross sections to be used in full-core calculations.

The neutron flux is the solution of a transport equation defined over the lattice cell. The transport equation is a balance relation of the neutron population in a finite volume $dv_n d^3r d^2\Omega$ surrounding $\{v_n, \boldsymbol{r}, \boldsymbol{\Omega}\}$. The time-dependent transport equation is given as:

$$
\frac{1}{v_n}\frac{\partial}{\partial t}\phi(\boldsymbol{r}, v_n, \boldsymbol{\Omega}, t) + \nabla \cdot \boldsymbol{\Omega}\phi(\boldsymbol{r}, v_n, \boldsymbol{\Omega}, t) + \Sigma(\boldsymbol{r}, v_n, \boldsymbol{\Omega}, t)\phi(\boldsymbol{r}, v_n, \boldsymbol{\Omega}, t)
$$
$$
= Q(\boldsymbol{r}, v_n, \boldsymbol{\Omega}, t) \tag{2.8}
$$

where

$\frac{1}{v_n}\frac{\partial}{\partial t}\phi(\boldsymbol{r}, v_n, \boldsymbol{\Omega}, t)$ represents the time-rate of change in the neutron density. This term is absent in steady-state conditions.

$\nabla \cdot \boldsymbol{\Omega}\phi(\boldsymbol{r}, v_n, \boldsymbol{\Omega}, t)$ represents the neutron streaming (transport term).

$\Sigma(\boldsymbol{r}, v_n, \boldsymbol{\Omega}, t)\phi(\boldsymbol{r}, v_n, \boldsymbol{\Omega}, t)$ represents all interactions that cause the loss of neutrons.

$Q(\boldsymbol{r}, v_n, \boldsymbol{\Omega}, t)$ represents the source term. This term is composed of fission, scattering and delayed neutron production terms.

In steady-state conditions, the first term of the left-hand side of the transport equation disappears to obtain the following equation:

$$\mathbf{\Omega} \cdot \nabla \phi(\mathbf{r}, \mathrm{v}_n, \mathbf{\Omega}) + \Sigma(\mathbf{r}, \mathrm{v}_n, \mathbf{\Omega})\phi(\mathbf{r}, \mathrm{v}_n, \mathbf{\Omega}) = Q(\mathbf{r}, \mathrm{v}_n, \mathbf{\Omega}) \qquad (2.9)$$

Here, the neutron energy $E = \frac{1}{2}m\mathrm{v}_n^2$ can be used instead of the neutron speed v_n:

$$\mathbf{\Omega} \cdot \nabla \phi(\mathbf{r}, E, \mathbf{\Omega}) + \Sigma(\mathbf{r}, E, \mathbf{\Omega}) \, \phi(\mathbf{r}, E, \mathbf{\Omega}) = Q(\mathbf{r}, E, \mathbf{\Omega}) \qquad (2.10)$$

The source term Q is composed of fission and scattering terms. The scattering terms are composed of elastic or inelastic collisions, and (n,xn) reactions. To write the terms of source, we consider that the scattering cross section Σ_s takes into account the different phenomena. Generally, this cross section is not isotropic and depends on incident neutron energy and direction.

$$Q_{scat}(\mathbf{r}, E, \mathbf{\Omega}) = \int_{4\pi} d^2\Omega' \int_0^{+\infty} dE' \, \Sigma_s(\mathbf{r}, E' \longrightarrow E, \mathbf{\Omega}' \longrightarrow \mathbf{\Omega}) \, \phi(\mathbf{r}, E', \mathbf{\Omega}') \qquad (2.11)$$

where

$\Sigma_s(\mathbf{r}, E' \longrightarrow E, \mathbf{\Omega}' \longrightarrow \mathbf{\Omega})$ is the macroscopic differential scattering cross section from energy E' to energy E and from direction $\mathbf{\Omega}'$ to direction $\mathbf{\Omega}$. Isotropy of materials is assumed, so the scattering cross sections depend only on the scattering angle $\mathbf{\Omega} \cdot \mathbf{\Omega}'$. In this case, Eq. (2.11) can be written as:

$$Q_{scat}(\mathbf{r}, E, \mathbf{\Omega}) = \int_{4\pi} d^2\Omega' \int_0^{+\infty} dE' \, \Sigma_s(\mathbf{r}, E' \longrightarrow E, \mathbf{\Omega} \cdot \mathbf{\Omega}') \, \phi(\mathbf{r}, E', \mathbf{\Omega}') \qquad (2.12)$$

For the fission source term, the fission neutrons are emitted isotropically and therefore the corresponding source terms are independent of $\mathbf{\Omega}$.

$$Q_{fiss}(\boldsymbol{r}, E) = \frac{1}{4\pi k_{eff}} \sum_{j=1}^{J} \chi_j(E) \int_0^{+\infty} dE' \nu \Sigma_{f,j}(\boldsymbol{r}, E') \, \phi(\boldsymbol{r}, E') \qquad (2.13)$$

where

$\chi_j(E)$ represents the fission spectrum. This is the probability density that the fission of the j-th isotope produces a neutron of energy E within interval dE.

$\Sigma_{f,j}(\boldsymbol{r}, E')$ is the fission cross section.

ν the average number of neutrons emitted per fission.

J is the number of fissile isotopes.

k_{eff} is the effective multiplication factor used to divide the fission source in order to maintain steady-state conditions.

Note that we have the following relation:

$$Q(\boldsymbol{r}, E, \boldsymbol{\Omega}) = Q_{scat}(\boldsymbol{r}, E, \boldsymbol{\Omega}) + Q_{fiss}(\boldsymbol{r}, E) \qquad (2.14)$$

In certain situations, such as when using perturbation theory to determine the effect of small changes in the macroscopic cross-section values on reactivity, the adjoint flux is needed. The adjoint flux is obtained by solving the adjoint Boltzmann equation given by:

$$-\boldsymbol{\Omega} \cdot \nabla \phi^*(\boldsymbol{r}, E, \boldsymbol{\Omega}) + \Sigma(\boldsymbol{r}, E, \boldsymbol{\Omega}) \phi^*(\boldsymbol{r}, E, \boldsymbol{\Omega})$$

$$= Q_{scat}^*(\boldsymbol{r}, E, \boldsymbol{\Omega}) + Q_{fiss}^*(\boldsymbol{r}, E) \qquad (2.15)$$

The adjoint scattering source term, $Q_{scat}^*(\boldsymbol{r}, E, \boldsymbol{\Omega})$, is defined as:

$$Q_{scat}^*(\boldsymbol{r}, E, \boldsymbol{\Omega}) = \int_{4\pi} d^2\Omega' \int_0^{+\infty} dE' \, \Sigma_s(\boldsymbol{r}, E \to E', \boldsymbol{\Omega} \to \boldsymbol{\Omega}')\phi^*(\boldsymbol{r}, E', \boldsymbol{\Omega}') \qquad (2.16)$$

The main difference between the direct and adjoint scattering source is the swapping of the incoming and outgoing neutron energies, E and E', as well as, the incoming and outgoing directions $\boldsymbol{\Omega}$ and $\boldsymbol{\Omega}'$.

The adjoint fission term, $Q_{fiss}^*(\boldsymbol{r}, E)$, is defined as:

$$Q_{fiss}^*(\boldsymbol{r}, E) = \frac{1}{k_{eff}} \nu\Sigma_f(\boldsymbol{r}, E) \int_{4\pi} d^2\Omega \int_0^{+\infty} dE' \, \chi(E')\phi^*(\boldsymbol{r}, E') \qquad (2.17)$$

The adjoint fission source has the same energy dependence as the fission-neutron spectrum, $\chi(E')$, and its spectrum follows the energy dependence of the fission cross section, $\Sigma_f(\boldsymbol{r}, E)$.

2.1.5 Multigroup Energy Discretization and Boundary Conditions

The resolution of the transport equation is defined by its multigroup discretization of the energy spectrum. The multigroup approach consists of dividing the energy spectrum to produce a set of G groups. That means that neutrons are assumed to behave as one-speed particles within the group. The energy dependent quantities are calculated by condensing over the energy groups. The lethargy variable $\mu = \ln(\frac{E_0}{E})$ can also be used, where E_0 is the highest possible energy of neutrons in the system.

We can write the transport equation in the multigroup form:

$$\mathbf{\Omega} \cdot \nabla \phi_g(\mathbf{r}, \mathbf{\Omega}) + \Sigma_g(\mathbf{r}) \, \phi_g(\mathbf{r}, \mathbf{\Omega}) = Q_g(\mathbf{r}, \mathbf{\Omega}) \tag{2.18}$$

where $g \in \{1, \dots, G\}$.

In the multigroup approach, the group-average values of the flux, the current and the source are respectively defined as:

$$\phi_g(\mathbf{r}, \mathbf{\Omega}) = \int_{\mu_{g-1}}^{\mu_g} \phi(\mathbf{r}, \mu, \mathbf{\Omega}) d\mu \tag{2.19}$$

$$\mathbf{J}_g(\mathbf{r}, \mathbf{\Omega}) = \int_{\mu_{g-1}}^{\mu_g} \mathbf{J}(\mathbf{r}, \mu, \mathbf{\Omega}) d\mu \tag{2.20}$$

$$Q_g(\mathbf{r}, \mathbf{\Omega}) = \int_{\mu_{g-1}}^{\mu_g} Q(\mathbf{r}, \mu, \mathbf{\Omega}) d\mu \tag{2.21}$$

The average cross sections for each group are defined in such a way as to preserve the reaction rates.

$$\Sigma_{x,g}(\mathbf{r}, \mathbf{\Omega}) = \frac{1}{\phi_g(\mathbf{r}, \mathbf{\Omega})} \int_{\mu_{g-1}}^{\mu_g} \Sigma_x(\mathbf{r}, \mu, \mathbf{\Omega}) \phi(\mathbf{r}, \mu, \mathbf{\Omega}) d\mu \tag{2.22}$$

$$\Sigma_{s,h \to g}(\mathbf{r}, \mathbf{\Omega} \cdot \mathbf{\Omega}')$$

$$= \frac{1}{\phi_h(\mathbf{r}, \mathbf{\Omega})} \int_{\mu_{g-1}}^{\mu_g} d\mu \int_{\mu_{h-1}}^{\mu_h} d\mu' \Sigma_s(\mathbf{r}, \mu' \to \mu, \mathbf{\Omega} \cdot \mathbf{\Omega}') \, \phi(\mathbf{r}, \mu, \mathbf{\Omega}) d\mu$$

$$\tag{2.23}$$

where μ_{g-1} and μ_g are the limits of the energy group g, and μ_{h-1} and μ_h are the limits of the energy group h.

Before we can attempt to solve the transport equation, we need to define the boundary conditions to close the system of equations. Depending on the nature of the problem, different types of boundary conditions can be imposed. Considering a

domain V that is surrounded by a boundary ∂V where boundary conditions are to be applied, solution of the transport equation requires the knowledge of the incoming flux.

An albedo boundary condition provides a relation between the incoming flux at the boundary and the outgoing flux. An explicit form of this relation is given by:

$$\phi(\boldsymbol{r_s}, \mathrm{v}_n, \boldsymbol{\Omega}) = \alpha \; \phi(\boldsymbol{r_s}, \mathrm{v}_n, \boldsymbol{\Omega'}), \forall r_s \in \partial V \tag{2.24}$$

where

r_s is a point on the boundary ∂V.

$\boldsymbol{\Omega'}$ is the direction of the outgoing particle.

$\boldsymbol{\Omega}$ is the direction of the incoming particle, and satisfies $\boldsymbol{\Omega} = \boldsymbol{\Omega'} - \boldsymbol{2}[\boldsymbol{\Omega'} \cdot \boldsymbol{n}(r_s)]\boldsymbol{n}(r_s)$, where $\boldsymbol{n}(r_s)$ is the normal vector.

A boundary condition with α = 1 is a reflective boundary condition. A reflective boundary condition can be used to evaluate the behaviour of a cell surrounded by infinite lattice of the same cell. α = 0 is called a vacuum boundary condition.

2.1.6 Reactivity Device Increments

The CANDU reactivity devices are orthogonally oriented to its fuel channels. These reactivity devices therefore require a 3D supercell model which generally consists of two adjacent horizontal lattice cells and a vertically oriented reactivity device between them. Reactivity devices are accounted for in the full-core model by 'incremental cross sections' to the basic-lattice properties from lattice calculations.

The increment of a given lattice property for a particular reactivity device is defined as the difference between the homogenized supercell cross section in the presence of the reactivity device and the same cross section in the absence of the device. The homogenized and energy-condensed cross sections are calculated based on the higher resolution cross sections using Eq. (2.25):

$$\bar{\Sigma}_{x,G} = \frac{\sum_{r \in V} \sum_{g \in G} V_r \, \Sigma_x(V_r, E_g) \phi(V_r, E_g)}{\sum_{r \in V} \sum_{g \in G} V_r \, \phi(V_r, E_g)} \tag{2.25}$$

where

$\bar{\Sigma}_{x,G}$ is the homogenized and condensed cross section for reaction x for condensed energy group G.

V_r is the volume of subregion r.

$\Sigma_x(V_r, E_g)$ is the macroscopic cross section of reaction x in subregion V_r for energy group g.

$\phi(V_r, E_g)$ is the flux in subregion V_r for energy group g.

Two sets of homogenized cross sections are calculated for each reaction x (absorption, fission, etc.): one in the absence of the reactivity device $\bar{\Sigma}_{x,G}$, and one in its presence $\bar{\Sigma}^d_{x,G}$, where d denotes the reactivity device. The macroscopic cross-section increments are then calculated as:

$$\overline{\Delta\Sigma}^d_{x,G} = \bar{\Sigma}^d_{x,G} - \bar{\Sigma}_{x,G} \tag{2.26}$$

The supercell reactivity increments can be calculated as the difference between the supercell reactivity in the presence, ρ^d, and in the absence, ρ, of the reactivity device:

$$\Delta\rho = \rho^d - \rho \tag{2.27}$$

2.1.7   Static Core Calculations

When cell average cross sections and incremental cross sections for reactivity devices are known, core calculations can be performed as outlined in Figure 2-3. This calculation is an assembly of homogenized cells with energy-condensed lattice homogenized properties with the reactivity device properties superimposed at volumetric representations containing reactivity devices. The full-core calculations can provide the global flux distribution, reaction rates and bundle and channel powers in the core.

The full-core calculation consists of solving the diffusion equation, which is only an approximation of the transport equation. This solution can be performed either in transient or static conditions using a small number of energy groups (generally, $G = 2$ is sufficient).

To obtain the diffusion equation from the multigroup transport equation given in Eq. (2.18), we introduce Fick's law into the transport equation. Fick's law is an empirical application based on the consideration that neutrons migrate globally from a region where their concentration is higher to a region where it is weaker. It gives a

directional relationship between the total neutron current and the flux gradient. The proportionality coefficient D_g is called the diffusion coefficient.

$$J_g(\boldsymbol{r}) = -D_g(\boldsymbol{r})\nabla\phi_g(\boldsymbol{r}) \tag{2.28}$$

The diffusion equation is then written as:

$$-\nabla \cdot D_g(\boldsymbol{r})\nabla\phi_g(\boldsymbol{r}) + \Sigma_g(\boldsymbol{r})\phi_g(\boldsymbol{r}) = Q_g(\boldsymbol{r}) \tag{2.29}$$

The diffusion equation can be solved using the standard finite-different method numerical technique. The static core calculations are a solution of the static diffusion equation based on an instantaneous snapshot of the fuel burnup distribution and corresponding lattice cell properties.

2.1.8   Time-Average Calculations

The time average model calculates the lattice properties that are averages of their values over the burnup cycle and provide a target power distribution for operational considerations. The time-average model, when completed, provides the targets for 3D flux, power, burnup and fuelling frequency for standard operations. The time-average power distribution, channel fuelling frequencies and the fuel discharge burnup values also provide a guide for core follow simulations.

Time-average nuclear cross sections can be defined at each bundle position in core by averaging the lattice cross sections over the irradiation range $[\omega_{in}, \omega_{out}]$ corresponding to the residence time of the fuel at a specific position in the core, where ω_{in} is the value of the fuel irradiation when the fuel enters that position in core and ω_{out} is the fuel irradiation when the fuel leaves that position. The cross sections are

defined such that they preserve the average reaction rate over the irradiation range ω_{in} to ω_{out}. In this case, the time-average cross section for reaction x at some bundle position r is:

$$\Sigma_{x,r,tav} = \frac{\int_{\omega_{in,r}}^{\omega_{out,r}} \Sigma_{x,r}(\omega)d\omega}{\int_{\omega_{in,r}}^{\omega_{out,r}} d\omega} = \frac{1}{(\omega_{out,r} - \omega_{in,r})} \int_{\omega_{in,r}}^{\omega_{out,r}} \Sigma_{x,r}(\omega)d\omega \qquad (2.30)$$

Since consistency must be achieved between the time-average flux, the channel dwell times, the individual-bundle irradiation ranges $[\omega_{in}, \omega_{out}]$, and the lattice properties, an iterative scheme between the solution of the diffusion equation and of the other supplementary equations is employed until all quantities converge. Typically, the user iterates on the values of exit irradiation $\omega_{out}(r)$ in the various regions to obtain a critical reactor and the desired flux shape.

Most reactors in the world use batch refuelling. To maintain steady core reactivity over the refuelling cycle, light water reactors (LWRs) utilize a burnable poison in the moderator and/or in the fuel to compensate for initial excess reactivity of the fresh fuel. In contrast, a CANDU reactor is refuelled online and maintains core reactivity by fuelling a few channels each day. From a refuelling point of view, the CANDU reactor core is typically subdivided into multiple (usually two) refuelling regions. For each of the refuelling regions, a specific exit irradiation is set, which determines the channel fuelling frequency for that region. Starting from a fresh fuel core, if the reactor is refuelled regularly to maintain necessary core reactivity, after a period of time, the reactor can be considered to reach equilibrium conditions, which are typically assessed for compliance with its time-averaged results.

2.1.9 Core-Follow Calculations

Core-follow calculations are performed to track the actual operating history of a reactor and composed of a sequence of 'instantaneous' or 'snapshot' calculations in the life of the reactor. The duration of the burn step between simulations is a user input. Typical burn steps are of the order of 1-3 full power days. At each step, individual channel refuellings are simulated and the core irradiation is advanced from the previous step using the previous flux and irradiation distribution and the length of the burn step. A full-core model in a diffusion code is most suitable to carry out core-follow simulations.

At the reactor design stage, core-follow simulations can be used to simulate the initial transient from start-up to equilibrium to investigate the effect of various refuelling schemes, to obtain estimates of likely maximum channel and bundle powers and discharge burnups, etc.

2.1.10 Kinetics Calculations

In modern reactor transient analyses, the space-time dependency of neutron in Eq. (2.8) is solved using kinetic methods. The most commonly used kinetic method in full-core simulations is the flux factorization method which can be further subdivided, in inverse order of accuracy, into improved quasi-static, quasi-static, adiabatic and point kinetics.

In flux factorization, the first step is to factorize the time-, energy- and space-dependent solution into a function dependent only on time and a vector

dependent on energy, space and time. The function that is dependent only on time is called an amplitude function $P(t)$, and the vector that is dependent on space, energy and time is called a shape function $\psi(\boldsymbol{r}, \mathrm{v}_n, t)$.

$$\phi(\boldsymbol{r}, \mathrm{v}_n, t) = P(t)\psi(\boldsymbol{r}, \mathrm{v}_n, t) \tag{2.31}$$

The amplitude function can be defined as follows:

$$P(t) = \langle w(\boldsymbol{r}, \mathrm{v}_n), \mathrm{v}_n^{-1}\phi(\boldsymbol{r}, \mathrm{v}_n, t)\rangle \tag{2.32}$$

Where $w(\boldsymbol{r}, \mathrm{v}_n)$ is an arbitrary weight vector dependent only on position and energy. $P(t)$ can therefore be interpreted as a generalized neutron population. In the case where the weight function is chosen to be unity, $P(t)$ would be exactly equal to the neutron population.

For full-core kinetics simulations using the flux factorization method, the calculation of the flux shape function is computationally expensive, whereas calculation of the amplitude function is relatively inexpensive. In many problems, the shape function is only weakly time-dependent. Therefore, calculation of the shape function at every time step may not be needed. If it is assumed that the shape function does not change during a transient and holds its initial unperturbed shape then integrating over volume and summing over energy groups results in the point kinetics formulation for the amplitude function. Other factorization methods such as adiabatic and quasistatic method are improvements over standard point kinetics since they allow for shape change to certain extents.

In the adiabatic method, the shape functions are recalculated at some macro-intervals during the transient. The updated flux shapes are the solution of the

static equation corresponding to the instantaneous condition of the perturbed reactor, which is artificially made critical by adjusting the fission source.

The quasi-static method is a generalization of the adiabatic method where instead of using a static calculation for the shape function, a full space-time kinetic calculation is performed to determine the shape function. Since the fast-varying amplitude part is factored out, the shape function varies much more slowly. This makes it possible to use large time steps for calculating shape function. This is to say that the time progression scheme is a two-tier scheme, since the amplitude function is calculated in every micro-interval using point kinetics, and the flux shape is calculated at much longer macro-intervals.

The improved quasi-static method, like all methods based on flux factorization, relies on calculating effective point-kinetic parameters, which dominate the time behaviour of the flux, using adjoint-weighted integrals.

2.1.11 Lattice-Level Reactivity Coefficients

In a reactor, macroscopic cross sections can change as a consequence of various parameters, and in turn, these changes can perturb the overall reactivity. The key parameters that influence reactivity are fuel, coolant and moderator temperature, coolant and moderator density and moderator poison.

Changes in reactivity induced by any one of the aforementioned parameters p are referred to as the reactivity effect of that parameter and denoted as $\partial \rho(p)$ The

derivation of the reactivity with respect to the change in the parameter $\frac{\partial \rho(p)}{\partial p}$ is called

the parameter's reactivity coefficient.

CANDU reactivity coefficients depend on the specific characteristic of the CANDU lattice. The reactivity coefficients can be calculated using a single lattice model where the subject parameter is varied within it limits while all other parameters are kept constant. This method is further discussed in Chapter 4.

2.2 The Molybdenum Producing Bundle

Researchers at Ontario Tech University have proposed a 37-element fuel bundle where each fuel pin is radially separated into two regions, one consisting of high-assay low-enriched uranium (HALEU) fuel and another consisting of depleted uranium fuel [3]. This modified 37-element fuel bundle is referred to in this dissertation as the '*Molybdenum Producing Bundle*' or 'MPB' and the standard CANDU fuel bundle is referred to as 'SCB'. A schematic of the MPB considered for this dissertation is shown in Figure 2-4.

All 37 fuel pins of the MPB are identical and are divided radially into two regions. The inner region consists of 0.2 wt% depleted UO_2 while the outer region consists of 19.5 wt% HALEU UO_2. The thickness of the outer, enriched-uranium, region of the pin is 79.36 μm.

19.5 wt% Enriched UO$_2$
Thickness: 79.36 μm

0.2 wt% Depleted UO$_2$
Radius: 0.60 cm
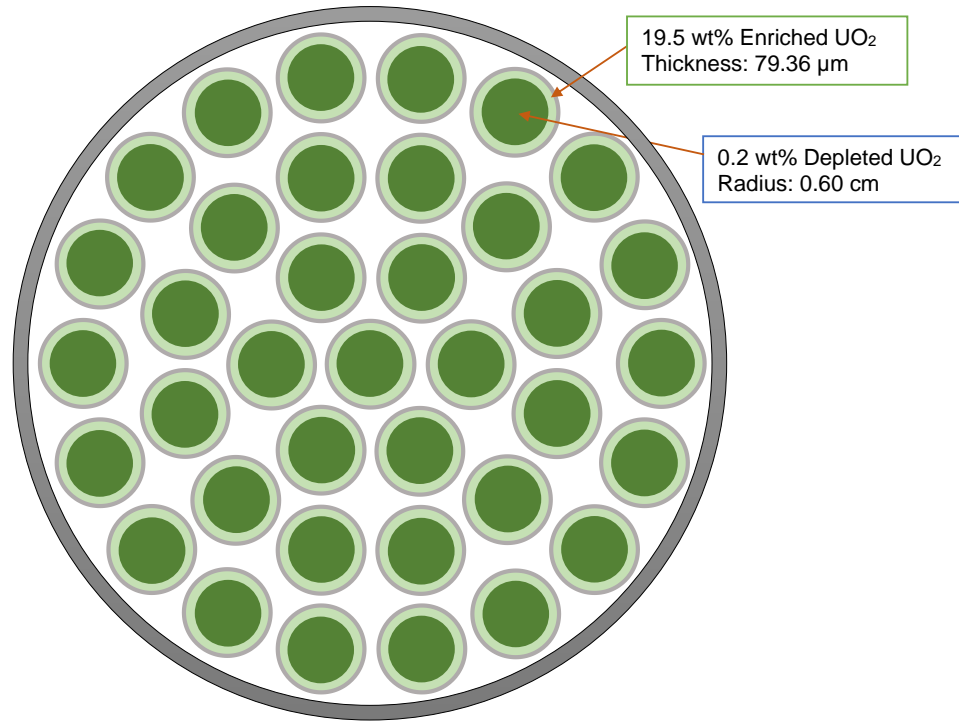
Figure 2-4: Schematic of the new MPB design

Outside of the heterogeneous fuel pins, the overall bundle geometry of the new MPB is dimensionally identical to that of the SCB. The MPB has the same fuel pin and sheath diameters as the SCB. This allows the MPB to have the same hydrodynamic properties as the SCB and ensures compatibility with the fuel handling devices, most notably, the fuelling machine. Hence, the MPB presented in Figure 2-4 has the same fuel pellet and sheath diameters as the SCB.

For an MPB, neutronic equivalence with the standard bundle was achieved by strategically designing the volumetric sizes of the enriched and depleted fuel regions inside each fuel pin. The addition of enriched uranium in the fuel pins causes an

increase in the fission rate resulting in higher reactivity in the region. To compensate for this increased reactivity, the remainder of the fuel pin is composed of depleted uranium (DU).

The preliminary study in Reference [3] compared the lattice cell reactivity, two-group homogenized macroscopic cross sections, linear heat rating and radial temperature profiles using transport calculations for static lattice cell models of MPB and SCB. The two-group homogenized cross sections were observed to match within ~1% and reaction rates at the fuel pin surface level were found to be similar among the two bundles. In addition, a stylized 3x3 diffusion model was produced to equate effective reactivities and normalized bundle powers at varying burnups with the SCB results. The differences in nodal power induced by the use of an MPB were smaller than 0.6% and the corresponding maximum change in the model reactivity was ~0.16 mk. It was therefore concluded that the newly designed MPB is equivalent to the SCB for all practical purpose during normal, steady-state, conditions.

The 19.5 wt% enrichment has been chosen to be just below the upper limit for low-enriched uranium (LEU), to avoid proliferation concerns. Moreover, the 19.5 wt% enrichment of the outer region is sufficiently high to allow ^{99}Mo extraction by existing irradiated fuel treatment processes. Aside from the slight modifications needed to accommodate the larger masses of LEU target material as compared to the HEU target for the equivalent output of ^{99}Mo, the rest of the chemical processing involved for the production of ^{99}Mo using LEU targets is similar to the acid dissolution technique presently used for obtaining ^{99}Mo using HEU [5]. The use of LEU for ^{99}Mo

production has been successfully demonstrated at many research reactors currently

producing ^{99}Mo using LEU targets.

The worldwide demand for ^{99}Mo is approximately 12,000 six-day Curies per

week [6], [7]. When accounting for the processing time and efficiency, 12,000 six-day

Curies is equivalent to approximately 77,000 end-of-bombardment Curies, which is

160 mg of ^{99}Mo at the end of the irradiation stage [8].

Curie is the unit of radioactivity (1 Curie = 3.7x1010 disintegrations per second

or Becquerels, Bq). A six-day Curie is a unit of measure most commonly used in the

industry which equates to the amount of ^{99}Mo remaining in a ^{99m}Tc generator six days

after shipment from the producer's facility. In other words, the producers usually

calibrate a shipment value to the activity of the ^{99}Mo isotopes 6 days after it leaves

the production facility [9].

The new MPB was evaluated to produce approximately 4,000 six-day Curies of

^{99}Mo activity per bundle when irradiated in the peak-power channel of a CANDU core

[3]. Accounting for the lower channel flux away from the core center, a production

rate of ~4 bundles per week is estimated to meet the global demand of ^{99}Mo.

Chapter 3:   Review of Literature

3.1 An Overview of Molybdenum-99 Production

Historically, ^{99}Mo has been produced at various research reactor facilities, where specially designed highly-enriched-uranium (HEU) targets are irradiated at dedicated high flux regions in these reactors. In some cases, the HEU targets were enriched to 90-wt% of ^{235}U or higher. Although some ^{99}Mo is produced in natural uranium (NU), the NU fuel composition is not suitable for producing significant quantities of ^{99}Mo since the ratio of ^{99}Mo yield to fuel volume processed is generally low. Therefore, the use of enriched fuel is desirable from the perspective of ^{99}Mo production [9].

3.1.1 Past and Current Molybdenum Producing Reactors

Until the end of 2015, five nuclear research reactors were producing approximately 95% of the world's supply of ^{99}Mo [10]. The five were the NRU reactor in Canada, the High Flux Reactor (HFR) in the Netherlands, BR2 in Belgium, OSIRIS in France, and the SAFARI-1 in South Africa. Prior to its shutdown, the NRU reactor was producing approximately 35% of the global demand for ^{99}Mo. In 2016, the NRU reactor ceased production of ^{99}Mo and in March of 2018, the reactor was permanently closed down after operating for 61 years [11]. The OSIRIS reactor in France was shutdown at the end of 2015 [12].

Currently, the world's supply of ^{99}Mo comes from six reactors, five of which are over 50 years old [10].

The typical production capacity of these six major isotope-producing reactors is shown in Table 3-1. In addition to the production of medical isotopes, these multi-purpose reactor facilities provide other services such as nuclear fuel testing and material research. The four European reactors have the capacity to produce approximately 70% of the global demand for ^{99}Mo. Five of these six reactors are using low-enriched uranium (LEU) targets for ^{99}Mo production. The OPAL reactor in Australia and the SAFARI-1 in South Africa, both of which use LEU targets, have the capacity to produce approximately 25% of the ^{99}Mo supply. The smaller reactors around the world support approximately 5% of the global demand. Table 3-1 also provides information on estimated reactor stop dates for these six reactors.

The majority of the smaller ^{99}Mo producing reactors accommodate the local or regional medical isotope markets. Some regional producers of ^{99}Mo are Argentina, Germany, Indonesia, Poland and Russia. The research reactors in the aforementioned countries do not produce the commercial quantities necessary to compensate for the closure of one or more of the big six-reactors. However, they can act as a short-term buffer when one of the big-six reactors experiences an outage. The regional reactors are listed in Table 3-2.

Consequently, alternative production methods and radioisotope production facilities need to be developed for a more stable supply of ^{99}Mo.

Table 3-1: Worldwide Production Capacity of Molybdenum-99 [10], [7], [13], [14]

Reactor	Typical Capacity (Six-day Curies)	Thermal Power (MW)	Thermal Neutron Flux (cm^{-2}s^{-1})	Target Type	Estimated Stop Date
BR2 (Belgium)	6500	100	1×10^{15}	LEU	2026
HFR (Netherlands)	6200	45	2.7×10^{14}	LEU	2022
OPAL (Australia)	3500	20	3×10^{14}	LEU	2030+
LVR-15 (Czech Republic)	3000	10	1.5×10^{14}	HEU	2028
SAFARI-1 (South Africa)	3000	20	2.4×10^{14}	LEU	2025
MARIA (Poland)	2200	10	1.5×10^{14}	LEU	2030

Table 3-2: Small-scale Producers of Molybdenum-99 in 2011 [10] , [9], [14]

Reactor	Typical Capacity (Six-day Curies)	Thermal Power (MW)	Thermal Neutron Flux (cm^{-2}s^{-1})	Target Type
MURR (USA)	750	10	6.0×10^{14}	HEU
ETTR-2 (Egypt)	250	22	2.8×10^{14}	LEU
RECH-1 (Chile)	250	5	7×10^{13}	LEU
RA-3 (Argentina)	200	5	4.8×10^{13}	LEU
RSG-GAS (Indonesia)	150	30	2.5×10^{14}	HEU
PARR-1 (Pakistan)	20	10	1.7×10^{14}	HEU
WWR-TS (Russia)		15	1.0×10^{14}	HEU
RBT-6 (Russia)		6	2.2×10^{14}	HEU
RBT-10/2 (Russia)		7	2.2×10^{13}	HEU
FRM-II (Germany)		20	8×10^{14}	HEU

3.1.2 Alternative Methods for Producing Molybdenum-99

Fission of ^{235}U-based targets inside a nuclear reactor is not the only method for producing ^{99}Mo. An accelerator can also be utilized to generate ^{99}Mo by photo-fission of the ^{238}U atoms present in NU. Alternative options for the production of ^{99}Mo include eliminating uranium from the process by using other isotopes of molybdenum and converting them to ^{99}Mo. This consists of four possible reactions: ^{98}Mo(n,γ)^{99}Mo (neutron activation) occurring inside a reactor, ^{100}Mo(γ,n)^{99}Mo, ^{100}Mo(p,pn)^{99}Mo and ^{100}Mo(p,2n)^{99m}Tc (neutron emission) using accelerators.

3.1.2.1 Photo-fission Process ^{238}U(γ,f)^{99}Mo

In this method, a high intensity beam of photons is generated and directed at ^{238}U. This reaction results in nearly the same 6.1% fission yield for ^{99}Mo as the fission yield of ^{235}U in nuclear reactors. The cross section for this reaction is 0.16 barn which is about 3700 times smaller than the fission cross section of ^{235}U [15]. As a result, a relatively large number of accelerators would be required to produce significant amounts of ^{99}Mo. The authors in Reference [9] estimated that half a dozen accelerators are needed to supply 30% to 50% of North American demand. In this method, after the irradiation process is complete, ^{99}Mo is chemically separated from the uranium targets in the same way as irradiated HEU or LEU targets in nuclear reactors.

3.1.2.2 Neutron Activation of Molybdenum-98

The reaction, ^{98}Mo(n,γ)^{99}Mo (neutron activation), requires thermal (~0.025 eV) or epithermal (0.025 – 1.0 eV) neutrons. However, only a small portion of this target

is converted to ^{99}Mo because the cross section of this reaction is small ($\sigma_{thermal}$ ~0.14 barns). In addition, although neutron activation of molybdenum generates the desired radionuclide with little to no waste stream, ^{99}Mo produced through this method is not 'carrier-free' as it contains ^{98}Mo (natural molybdenum contains approximately 24% of ^{98}Mo) which is chemically identical to ^{99}Mo and behaves as a contaminant [16]. Therefore, the potential exists for increased elution of undesirable ^{98}Mo when formulating patient dosages.

The ^{99}Mo produced through neutron activation has low specific activity and requires a large number of targets to produce significant quantities of ^{99}Mo. A nuclear reactor would still be required to provide the necessary neutron flux for this method.

3.1.2.3 Neutron Emission from Molybdenum-100

The three neutron emission-based methods (^{100}Mo(p,pn)^{99}Mo, ^{100}Mo(γ,n)^{99}Mo and ^{100}Mo(p,2n)^{99m}Tc) require accelerators that can generate very high intensity beams of protons (500 μA) or electrons, in order to create photons powerful enough to overcome the significantly smaller cross sections for these reactions.

When the ^{100}Mo(γ,n)^{99}Mo reaction is employed, high energy photons known as Bremsstrahlung radiation are produced by the electron beam as it interacts and loses energy in the 'converter' target. The photons are subsequently used to irradiate another target material (^{100}Mo) placed just behind the converter to produce ^{99}Mo via neutron emission.

The ^{100}Mo(p,2n)^{99m}Tc neutron emission method results in the direct production of ^{99m}Tc which has a significant disadvantage due to its short half-life. It is not an ideal

method to produce ^{99m}Tc because any need to ship the ^{99m}Tc generators over long distances would reduce the usefulness to the end-user and by extension, to the patient [9].

3.1.3 Power Reactors and Production of Molybdenum-99

Production of ^{99}Mo using commercial power reactors is a novel idea considering nuclear reactors that are purposed for power production are not normally used to produce radioisotopes. In the past, a few other radioisotopes have been produced in power reactors, particularly in CANDUs. For example, tritium is recovered from the heavy water coolant in some CANDU stations [17]. The cobalt-based adjuster rods used in some CANDU stations are also processed to produce cobalt-60 sources for industrial radiation processing and radiosurgery. However, most commercial power reactors generally restrict their use solely to the generation of electricity.

It is possible to irradiate targets in the irradiation channels that exist in some pressure tube type reactors to produce molybdenum and other radioisotopes. For instance, unused instrumentation channels can be used to irradiate targets in CANDU reactors. However, this may be a challenging task requiring reconfiguration of the reactor instrument calibration and possibly the core neutronics. Production of lutetium-177 (^{177}Lu) has been recently achieved through irradiation of specially designed targets inside a CANDU irradiation channel [18]. Another CANDU station has retrofitted an isotope irradiation system for the purpose of producing ^{99}Mo via irradiation of natural molybdenum targets inside the core [19].

Production of ^{99}Mo through irradiation of uranium fuel in CANDU has been explored by other researchers in the past [20], [8], [21]. Researchers at McMaster University have analyzed a new 37-element fuel bundle containing a combination of slightly enriched/depleted uranium pins that, when irradiated inside a CANDU reactor, could yield 100% to 120% of the world's demand of ^{99}Mo [8], [21]. These researchers proposed modifications to the standard 37-element fuel bundle that would contain 1.5% to 3% enriched uranium dioxide fuel either in the second and third ring, or in the fourth ring of the fuel bundle, with the rest of fuel pins containing depleted uranium. Neutronic calculations using the WIMS-AECL lattice code showed a reactivity difference of +10 mk to +15 mk from the reference SCB. Although these proposed modified bundles were shown to produce significant amounts of ^{99}Mo when irradiated in the central and/or periphery channels, the significant reactivity increase of 10 mk to 15 mk per bundle have the potential to adversely affect important reactor safety parameters and potentially the existing operational envelope of the plant.

Whenever a bundle design deviates from the standard bundle design either neutronically or thermal-hydraulically, some of the neutronics and thermal-hydraulic safety analyses need to be repeated using the new bundle specifications in order to prove the safety case for the new bundle design. In particular, the power distribution in the core and inside the bundle, the coolant temperature, density and pressure at all locations in the core and fuel temperatures need to be re-calculated.

A better alternative to producing ^{99}Mo in the CANDU reactor fuel is to use modified 37-element fuel bundles that do not affect important reactor safety

parameters and existing operational envelope and safety margins. The challenge lies in developing a fuel design that has similar neutronics and thermal-hydraulic characteristics to the SCB and is able to produce significant quantities of ^{99}Mo. One such fuel bundle is the MPB, which has been developed by authors of Reference [3] and presented in Figure 2-4. This dissertation further evaluates the neutronic characteristics of the MPB particularly from the view point of its transient behaviour in the core and refuelling strategy.

3.2 Standard Methodology for Characterization of CANDU Bundles

In reactor physics, the process for characterizing fuel is a multi-phased one as briefly described in Chapter 2. The physics of CANDU design is based on a large number of accurate measurements of detailed physical parameters in lattices of a wide range of bundle design and channel separations, etc. To assist in these design exercises, several lattice codes have been written over the years to treat the intricate geometrical layout of fuel bundles in a pressure tube, which in turn is surrounded by a gap and a calandria tube separating the moderator from the hot coolant in the pressure tube.

There are several variations of fuel bundles that have been analyzed for use in CANDU reactors. These bundles vary in the number and size of fuel elements. The SCB contains 37 elements comprised of NU and is arranged in four concentric rings of 1, 6, 12 and 18 elements. The pin cladding, the pressure tube and the calandria tube are

made of zirconium alloys. A pictorial representation of the 37-element fuel lattice is

shown in Figure 3-1.
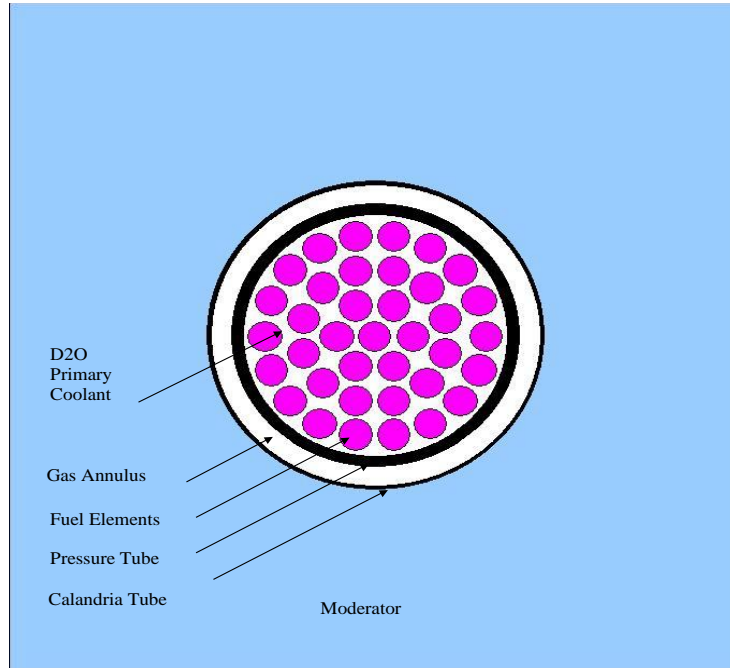
Figure 3-1: 37-Element standard CANDU bundle lattice cell

Each lattice is a basic unit in building a reactor core model, with its neutronics

characteristics represented by a set of homogenized nuclear reaction cross sections

determined by lattice-cell calculations. Due to the highly heterogenous nature of the

CANDU lattice cell, an extremely detailed spectral information must be accurately

modelled [22].

Since the early days of CANDU fuel prototypes, there has been a need for a fast

and reasonably accurate lattice code for assessment and design purposes. Lattice

codes allow for heterogeneity of lattice geometry to be explicitly represented. In

regular lattice calculations, the fuel elements are discretized to capture the evolution of the fuel composition during burnup and to capture the 'rim effect'. Applicable self-shielding models are also employed. The outermost moderator region is discretized in order to ensure spatial convergence of the flux for transport calculations using the most applicable solution technique, e.g., the collision probabilities (CP) method.

Several organisations have developed numerous lattice codes over time. A commonly used lattice code in the CANDU industry is WIMS-AECL [23], [24]. The WIMS code was initially developed at Winfrith for its general purpose and later developed at Chalk River Nuclear Laboratories with the focus on code applicability to CANDU lattice requirements. WIMS-AECL comprises of complete functionality of a lattice code which includes treatment of the complete energy domain, a resonance self-shielding model and diffusion coefficient calculation.

Another noteworthy mention is the lattice code DRAGON, which has been developed at the Ecole Polytechnique and is considered as one of the recommended codes by the Canadian nuclear industry to be used for lattice calculations. The DRAGON code solves the integral neutron transport equations using 2D or 3D integral neutron transport equations using either the CP method or the Method of Characteristics (MOC). The code is capable of handling nuclear data in various formats.

The DRAGON code is an assembly of calculation models which can simulate the neutron behaviour in a pincell or fuel assembly. The calculation models are

41

implemented in the form of various modules that include modules to read the geometry, read the microscopic cross section libraires from various sources, perform self shielding calculations, track geometry, obtain collision probabilities and solve for a flux. Other modules are capable of performing burnup calculations of various fuel types, merging of fluxes in multiple regions and generating new homogenized cross section libraries. The sequence of modules most commonly used in DRAGON as well as information transfer are shown in Figure 3-2. It should be noted that one or multiple module calls can be made throughout the calculations. Furthermore, the list of the module shown in Figure 3-2 are only a subset of modules available to DRAGON users. A detailed description of key modules can be obtained from the DRAGON User Manual [25].
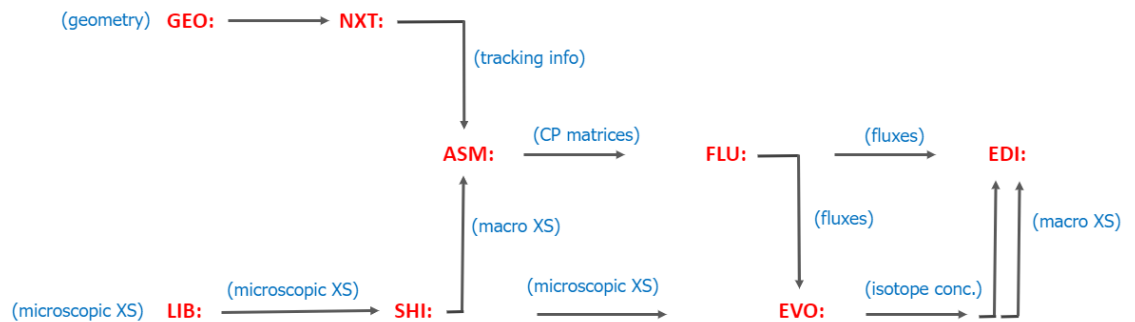
Figure 3-2: Sequence of modules in DRAGON

The standard methodology for neutronic characterization of advanced fuel bundles is based on the following steps:

1. Use of a lattice code (WIMS-AECL, DRAGON, e.g.) for all neutron transport calculations in space and energy in 2D.

2. Use of homogenization techniques to process multi-region flux distributions and cross sections calculated by the transport calculations in space and energy into homogenized properties and a smaller number of condensed energy groups, typically two energy groups.

3. Use of a 3D lattice code to simulate the 3D representation of fuel lattice and the orthogonally oriented reactivity device, and the use of similar homogenization techniques to represent reactivity devices using incremental macroscopic cross sections.

4. Use full-core 3D models based on state-of-the-art diffusion theory-based codes incorporating homogenized cross sections from Step 2 and 3 to characterize a reactor core including solution of reactor core flux and reactivity.

The above methodology has been documented in detail in References [23], [26].

The standard methodology employed by the CANDU industry typically relies on a 2D fuel lattice calculation to generate the few group fuel properties either using WIMS-AECL or DRAGON and on a 3D supercell calculation using DRAGON for the analysis of the reactivity devices present in the core [27]. DRAGON provides a higher degree of flexibility in terms of modelling options and state-of-the art resonance self-shielding calculations that goes beyond WIMS-AECL based models. Although the WIMS-AECL is still being utilized in the CANDU industry as the 'Industry Standard Toolset' for generation of latticed homogenized and energy condensed cross sections,

these functionalities are also available in DRAGON. Due to this, WIMS-AECL is not utilized in this study.

The CANDU core consists of 380 horizontal fuel channels, each containing 12 37-element fuel bundles. Each of the fuel bundles used in the core has identical geometry and is typically marked by a serial number. The lattice conditions at which the design calculations are performed are typically representative of a core at the nominal operating conditions (100% full-power hot operation). The moderator and coolant temperatures are usually assumed core-average values. The fuel temperature is a weighted core average temperature [28]. With the advent of high-speed and high-memory computers, it is now feasible to analyze rector lattices with a high degree of spatial and spectral subdivisions.

3.3 Methods and Models for Calculating Reactivity Coefficients

The reactivity coefficient is a measure of feedback reactivity. It is defined as the change in system reactivity due to a change in a key lattice or core parameter, $\frac{\partial \rho(p)}{\partial p}$. Introducing the definition of ρ namely,

$$\rho = \frac{k-1}{k} = 1 - \frac{1}{k} \tag{3.1}$$

And differentiating gives

$$\frac{\partial \rho}{\partial p} = \frac{1}{k^2} \frac{\partial k}{\partial p} \tag{3.2}$$

In all cases of interest, the multiplication factor, k, is close to unity and so Eq. (3.2) can be written approximately as

$$\frac{\partial \rho}{\partial p} = \frac{1}{k} \frac{\partial k}{\partial p} \tag{3.3}$$

A precise knowledge of the reactivity coefficients due to change in the physical properties of the core such as material temperature or density, and their variation with fuel irradiation is desirable as they are important parameters in the development of a new fuel bundle design. The dynamics of nuclear reactors are strongly dependent on the nuclear properties of the materials from which they are built. These properties are strongly coupled to the thermodynamic and physical status of the materials involved. Because of the complex nature of the phenomena involved in parameter-induced reactivity changes, these calculations are typically performed in a transport code [29]. In certain situations where spatial effects are strong, the reactivity changes are often calculated in static core diffusion calculations where the findings can be compared against experimental values to test the accuracy of the methods used.

The reactivity coefficients are calculated as small changes about the nominal operating conditions, i.e., as differences between given initial and final operating states. Reactivity effects are used to model the reactor-power feedback in reactor kinetics calculations. The most important reactivity coefficients are those associated with changes in temperature, density and poison concentration in key reactor parameters, namely coolant density, moderator density, coolant temperature, moderator temperature, fuel temperature and moderator poison concentration.

At the dawn of advanced deterministic codes for use in lattice calculations, a researcher at Chalk River Nuclear Laboratories used a legacy version of WIMS and 47 energy group ENDF/B-V nuclear library data to benchmark the coolant density (void) reactivity coefficient among other lattice phenomena [30]. Six different 2D models of 37-element cluster of UO_2 fuel with a heavy water coolant and a square lattice pitch of 28.6 cm were created where each model represented a specific static lattice state with parameters set to values of particular interest. The reactivity effects due to voiding of coolant in the lattice from WIMS were compared with a Monte Carlo calculation and they were found to be in good agreement.

In the study documented in Reference [31], the fuel temperature coefficient of the SCB was calculated by WIMS-AECL with ENDF/B-V cross section library and compared with a variant of the SCB. Details of the lattice model used for calculation of the fuel temperature coefficient of the two bundles were not given as the focus of the study was to analyze the effect of fuel temperature coefficient on core performance.

Coolant void reactivity is a very important safety parameter for CANDU reactors. This is because, unlike LWR designs, the pressure-tube design of a CANDU physically separates the D_2O coolant from the D_2O moderator, allowing substantial moderation to occur even when the entire or partial coolant supply is lost. In Reference [32], coolant void reactivity calculations were performed for SCB and a variant of the SCB using WIMS-AECL with cross sections derived from ENDF/B-VI. Only a one-quarter segment of the lattice cell of half the full lattice height was

modelled explicitly with reflective-boundary conditions applied to all cell-boundary surfaces except for the cases with leakage, which had a vacuum-boundary condition at one axial end. The coolant and moderator were modelled with the same isotopic purity of 99.65 wt% D_2O. The models used a 33-energy group library and employed the collision probability method. The calculated coolant void reactivity affects were calculated to be in good agreement between WIMS-AECL and the results obtained using Monte Carlo based calculations.

At the onset of the 21st century, the designers of CANDU reactors were looking at the "Next Generation" CANDU reactors based on CANFLEX fuel bundles. These reactors were aimed at producing electrical power at a reduced capital cost by eliminating the use of D_2O as coolant and incorporation of slightly enriched uranium (SEU) in a tight D_2O moderated lattice. The Next Generation CANDU design centered on adapting the fuel channel lattice which achieves a modestly positive value of coolant void reactivity. The key parameter that makes possible this low value is the moderator-to-fuel ratio in the lattice. By reducing the lattice pitch in the core, the designers effectively reduced the moderator-to-fuel ratio and thereby reduced the coolant void reactivity. Of course, spatial and spectral changes of the neutron flux in the lattice cell due to voiding of the coolant, as well as the nuclide composition in the fuel, also affect the coolant-void reactivity to a lesser extent. The work documented in Reference [33] provided a survey study of the relationship between coolant-void reactivity and fuel enrichment as a function of lattice pitch using the lattice code WIMS-AECL with ENDF/B-VI based nuclear cross section library. Details of the lattice model used for calculation of the coolant void reactivity were not given. It was

concluded that full-core coolant-void reactivity in Next Generation CANDU is less than one Beta (total delayed-neutron fraction).

The coolant void reactivity for CANDU reactors has been calculated using a single lattice cell with several nuclear codes documented in References [34], [35], [36], [37], [38], [39]. The coolant void reactivity has also been evaluated in CANDU lattice cells using DRAGON [40]. It is recognized that for higher accuracy, in particular for checkerboard voiding, simulation of coolant void reactivity should be performed using transport assembly models.

In the 2002 proceedings of the Canadian Nuclear Society conference, a summary paper documented the WIMS-AECL validation against 11 different reactor physics phenomena of interest which included, among other parameters that influence reactivity, fuel temperature, coolant and moderator temperature, coolant and moderator density and moderator poison induced reactivity changes [41].

Traditionally for 2D lattice calculations of reactivity coefficients, the evaluation of temperature profile within a fuel pin is carried out with the assumption that the temperature does not vary with the azimuthal angle. The fuel temperature is assumed a weighted core average of temperature even for temperature reactivity coefficient calculations. Notwithstanding a noticeable variation of the azimuthal power actually exists even for NU based fuel pins particularly in the outermost ring since the outer surface is in close proximity to the moderator and hence a higher intensity of thermal flux.

The asymmetric heat production due to neutron flux gradients across a fuel pin is a known phenomenon for SCBs. This asymmetric heat production is even more pronounced for the MPB due to the heterogeneity of the fuel pin [3]. The authors in Reference [28] investigated the effect of distributed temperatures in a pin under steady-state conditions using WIMS-AECL and an undisclosed external nuclear data library. A finite element analysis code was utilized to obtain two-dimensional distribution of fission power and fuel temperature within the fuel pins. It was concluded that WIMS-AECL simulations using the uniform temperature yielded lattice reactivity-to-burnup curve that was very close to that generated with distributed fuel temperatures. It was therefore concluded that for homogeneously composed fuel pins in the SCB, using uniform fuel temperature in lattice simulations yields very close results to those obtained with a more accurate fuel temperature distribution across the radial length of the pin. The authors further noted that for enriched uranium or mixed oxide fuel pins, the pin power distribution is more skewed in the fuel pins and the effects of fuel temperature distribution within the fuel pins would have a more noticeable impact on lattice calculations.

Reference [42] reports on an interesting study where the authors benchmarked the DRAGON calculations of the reactivity coefficients for a SCB lattice with a Monte Carlo based code. The DRAGON calculations employed the JEFF 3.1 based microscopic cross section library; condensed into 69 energy groups that has been made compatible under the WIMS-D4 format by way of the WIMS-D Library Update Project (WLUP). For the Monte Carlo simulations, continuous energy JEFF 3.1 evaluated microscopic cross section data library was employed. The reactivity effects were

determined for changes to the coolant, moderator, and fuel temperatures and to the coolant and moderator densities for zero-burnup, mid-burnup and discharge burnup fuel. It was found that the overall trend in the reactivity coefficients calculated using DRAGON matched those calculated using the Monte Carlo based code for the burnup cases considered. However, differences that exceeded the amount attributable to statistical error were found for some reactivity effects, particularly for perturbations to coolant and moderator density and fuel temperature.

The overall theme of the literature review indicates that lattice level calculations for analyzing reactivity coefficients are routinely performed for various CANDU compatible fuel bundles. Lattice level calculations involve intricate geometry details especially that of the fuel pins. Reflective and translational boundary conditions are applied to the lattice in order to estimate integral parameters like the infinite multiplication factor, flux distribution at various locations, spectral indices, conversion ratio, etc.

In the past, the transport models had used stylized models of the fuel to reduce computational demand, but with time, the lattice models have used more explicit geometry and spectral representations. The fuel, coolant and the moderator region are typically subdivided into separate regions. The geometries are often simplified and subdivision of regions removed to perform the self-shielding calculations. Uniform fuel temperature is used ignoring the radial shape and variation of fuel temperature between fuel pins of a bundle.

3.4 Methods for Interpreting Reactivity Coefficients

CANDU reactivity coefficients depend on the specific characteristics of the CANDU lattice. Of particular importance is the coolant density or void reactivity coefficient in CANDU reactors as mentioned in Section 3.3. One way to interpret what the coolant void reactivity is by considering the four factors that constitute the infinite multiplication factor (k_{inf}). The four factors are fast fission factor (ε), resonance escape probability (þ), thermal utilization factor (f) and thermal reproduction factor (η).

$$k_{inf} = \varepsilon \; \text{þ} f \, \eta \tag{3.4}$$

This formalism leads to physical interpretation and can provide quantitative estimates of reactivity coefficients for thermal reactors [43].

The four-factor based evaluation of reactivity coefficient has been widely used in the industry. The author in Reference [44] performed a detailed investigation of factors influencing the coolant void reactivity in CANDU reactors. The author performed several lattice calculations using WIMS-AECL with both geometric and critical bucklings and 69-energy neutron group based on ENDF/B-IV. The author concluded that the most overwhelming effects in coolant void reactivity are the increase in the epithermal group escape probability in ^{238}U, and the increase in the thermal yield efficiency and utilization in ^{235}U. In the negative direction, the most important countering effects is the decrease in thermal yield efficiency and utilization in ^{239}Pu, which builds as burnup progress. The loss of down-scattering in the coolant

creates a hardened spectrum that leads to increased fast absorption and fission as well as decreased resonance absorption. In the thermal range this is countered by the loss of thermal up-scattering, reducing absorption and fission in ^{239}Pu. At the same time a shift of the thermal and epithermal spatial flux distribution takes place, increasing the former and decreasing the latter in inner fuel regions. The effects of increased thermal absorption and decreased epithermal absorption are therefore greatest. in relative terms, near the centre of the fuel cluster.

Thus far in this section, the factors induced by coolant density reactivity in CANDU reactors have been discussed. Whenever neutron population increases due to any positive reactivity feedback, the fission heating increases. Since this heating is deposited in the fuel element, the fuel temperature will increase immediately. Several lattice parameters are affected by variations in fuel temperature due to changes in the neutron cross sections and in the neutron energy spectrum. Furthermore, as the fuel temperature increases, Doppler broadening of the resonances in the absorption cross sections of ^{238}U occurs which leads to increased neutron absorption. As a result, increases in fuel temperature leads to negative reactivity feedback. The change in reactivity due to change in fuel temperature is a function of the fuel composition and burnup.

During operation at constant power, the fuel temperature distribution is linked to the core power distribution where the temperature in the fuel pin is itself a distributed temperature profile along the length of the fuel pin. However, as stated in Section 3.3, in production models, the effect of the fuel temperature distribution on

the overall neutron balance is reproduced by using a spatially constant weighted average value of fuel temperature.

Some of the increased fission heat is transported out of the fuel pin into the surrounding coolant, causing a delayed increase in coolant temperature. An increase in coolant temperature will produce a decrease in coolant density, which causes a change in the local fuel-coolant properties and subsequently affects the lattice reactivity. Similarly, reactor operations can also lead to an increase in moderator temperature and consequently decrease moderator density. Local fuel-moderator properties will be impacted including changes in both the moderator absorption and the fuel to moderator flux ratio. The reduction in moderator density increases the diffusion of neutrons and increases leakage, producing a further change in reactivity.

Reference [45] provides insight into various physical phenomena that contribute to reactivity coefficients through the lens of a modified version of the four factors which also includes non-leakage probability. The author also provides a discussion of a linear perturbation theory-based approach that can be used for quantitative evaluation of reactivity coefficients. The prescribed perturbation approach is to multiply the perturbed and unperturbed equations by its adjoint, ϕ_g^*, subtract the two, integrate over the volume of the reactor, and sum over all energy groups to obtain the perturbation theory estimate for the change in reactivity associated with the perturbation in material properties. The author then provides application of the perturbation-based approach to fast reactor reactivity coefficients

while acknowledging that this approach is also applicable for thermal reactor reactivity coefficient evaluation.

It is noteworthy that this dissertation includes a first-of-its-kind application of the linear perturbation formulism to gain insight into the correlation between the parametric changes in a specific cell region and the corresponding reactivity effect. The approach used herewith captures, in synthetic form, the relationship between changes in the energy-dependent macroscopic cross sections in a specific cell region and the corresponding integrated reactivity effect. Chapter 4 provides a detailed explanation of this strategy.

3.5 Methods and Models for Calculating Reactivity Device Increments

The orthogonal orientation of the CANDU reactivity-control devices with respect to the fuel channel requires a full 3D model to capture the variations in neutron flux along the length of the fuel channel and locally, near reactivity device components. The usual calculation scheme as covered in Section 3.2 follows that after the 2D lattice calculations and after application of an adequate homogenization technique, the incremental cross sections of reactivity devices are then computed using a 3D model of fuel bundle and a neighbouring reactivity device.

Although the use of high resolution in 3D neutron transport models has always been preferred, the impact of performing such analyses has always been thought to be very significant in terms of limitation of the transport codes and required

computational effort. The earlier methods for calculation of the 3D neutron flux distribution in and around the fuel channels and reactivity devices consisted on one- and two-dimensional transport calculations using the WIMS-AECL code, a superhomogenization step, and 3D flux calculations with finite-difference diffusion theory application. Details of this legacy method is documented in Reference [23]. The results of this method were benchmarked against station measurements and found to be in reasonable agreement but indicated that there was significant variability depending on the reactor and differences were attributed to uncertainty in the measurement data.

In a paper published in 1994, the authors provided a review of the supercell calculations process that was implemented in an older version of the DRAGON code [46]. At the time, only cylindrical geometries were available in DRAGON for 3D modelling, no clusters could be processed in these cylinders. Therefore, different regions of fuel channel and reactivity devices were represented as combinations of cylindrical and rectangular regions, preserving the overall cylindrical geometry for both fuel channel and reactivity devices. The fuel cluster was homogenized by merging all regions inside the pressure tube into a fuel paste, and the cluster geometry of the zone controller unit was annularized into multiple regions. To perform the supercell calculations meant to only represent one bundle surrounded by its moderator and part of a reactivity device.

The work documented in References [47] and [48] compared the efficacy of the WIMS-AECL/MULTICELL and WIMS-AECL/DRAGON-2 modelling methods by

comparing the incremental cross section properties with Wolsong-1 and Point Lepreau nuclear reactor stations' measurements. It was discovered that both methods produced good agreement for cross-section increments for stainless steel adjusters but the agreement was not quite good for zone controller units. For shutoff rods/mechanical control absorbers, there was appreciable discrepancy between the two modelling approaches. The worsening trend between the two modelling approaches was attributed to superhomogenization treatment and the use of diffusion theory in MULTICELL with strong absorptions and 3D flux gradients associated with reactivity devices with higher worth.

From thereon, the diffusion-based approach used in the past for supercell calculations was replaced by the transport-based DRAGON code and the DRAGON code became the industry standard tool for the generation of device incremental homogenized cross sections [49]. It bears mentioning that the Canadian nuclear industry has adopted WIMS-AECL, DRAGON and RFSP (a diffusion code) for use in safety analysis, licensing and routine operations for CANDU reactors. Each of three reactor physics codes have gone through systematic assessment of code applicability addressing the unique features of the CANDU design including novel aspects of the code models, structure and constitutive correlations. These three computer codes are actively managed, configured and validated under the Industry Standard Toolset (IST) program at CANDU Owners Group.

Because of complexity and computational needs, the supercell calculations are continued to be performed using simplified or stylized fuel and reactivity device

geometries in DRAGON where applicable [23]. The overall calculation strategy for the generation of reactivity device incremental cross sections can be summarized as follows:

i.   2D lattice calculations with fully explicit cluster representation of fuel using complete neutron energy group structure;

ii. Full energy group macroscopic cross-section computations using the 2D results; in some cases, the number of neutron energy groups are reduced to less than 100 energy groups;

iii. Homogenization of fuel-cladding-coolant region with or without energy condensation;

iv. Cylindrization of the reactivity device, if necessary;

v.   Two-bundle-model 3D supercell calculation with and without the reactivity device; and

vi. Incremental cross-section calculations using the difference between the two 3D results.

Reference [50] validated the application of 3D neutron transport calculation of CANDU reactivity devices in DRAGON using the steps outlined above against measurements made in the Pickering-A Unit 4 and Darlington Unit 4 nuclear reactor stations for zone controller units, adjuster rods, and shutoff rods/mechanical control absorbers. It was discovered that all device-calibration cases, the calculated device reactivity worth underestimated the calculated worths of measured zone level changes. The calculation accuracy obtained for each of the measured devices was

found to be between 5% and 7% of the measured changes. Reference [27] validated the WIMS-AECL/DRAGON based method by comparing with the device-calibration measurements obtained from Bruce-A Unit 4 nuclear reactor station restart commissioning data. The validation exercise showed excellent results, with the DRAGON code overestimating the measured liquid zone controllers worth by ~5%. Reference [51] used the same modelling process to calculate the incremental reactivity cross sections for Wolsong Unit 1 station reactivity devices and various structural materials.

The development of new geometry features in DRAGON and the availability of faster computers have made it possible to improve the 2D cell and 3D supercell models by using explicit 3D assemblies of clusters to simulate the reactivity devices in CANDU reactors. The most commonly employed model of a 3D supercell configuration consists of two 3D lattice cells extending to the full length of the bundle and a perpendicular reactivity device located at the center, between the two lattice cells.

In 2006, it was announced that the developers of the DRAGON code have now made it possible to explicitly analyze and process 3D assemblies of the fuel reactivity device clusters in a 3D calculation by introducing a new tracking procedure incorporated in the NXT module of DRAGON [52]. Although previously both stainless steel adjuster rods and shutoff rods/machinal control absorbers could be explicitly modelled due to their cylinderized geometries, it had not been possible to explicitly model liquid zone controllers or cobalt adjusters in supercell calculations, which

effectively necessitate the most complex geometry. The introduction of the NXT tracking module expanded the geometrical handling capabilities of DRAGON and made it possible to treat the liquid zone controllers in their exact 3D supercell geometry. Reference [52] presented a set of calculations using cluster geometries of fuel and liquid zone controllers. The self-shielding procedure was based on the improved Stamm'ler method without Livolant-Jeanpierre normalization and used microscopic cross section data from the WLUP IAEA 69-group library [53]. The self-shielding calculations were performed on a 2D two-bundle geometry since a comparison with self-shielding directly on the 3D geometry is considerably expensive in terms of computer time and also did not result in noticeable differences. The authors also compared the performances of the CP method and method of characteristics within the framework of incremental cross-section calculations. It was concluded that both methods may be used for supercell calculations as they produced coherent results. The work of Reference [54] used the new geometry features of DRAGON to explicitly model 3D assemblies of clusters to simulate reactivity devices adjacent to 43-element CANFLEX fuel. Since the use of explicit 3D geometries implies a very fine spatial mesh discretization that can generate a large number of regions leading to problems, the author sided for the use of method of characteristics instead of the CP method. The work also provided a comparison of results using these two solution methods for 3D models with a coarse mesh discretization. The results of the use of 3D cluster model were found to be very close to those obtained by the annularized model (the standard model) with fine mesh discretization. This was not surprising because the Advanced CANDU Reactor 1000 (ACR-1000) reactivity devices

considered in this work are simply rectangular plates. It was inferred that some improvements are expected with 3D cluster model where the reactivity devices are more complex, for example, the cluster geometries of CANDU liquid zone controllers.

The literature review confirms that the use of 3D supercell models using advanced transport codes is a common practice. The DRAGON code is well-suited to process 3D assemblies of the fuel and reactivity device clusters in a 3D calculation. However, in order to reduce the computational burden, the standard calculation scheme used in the industry for generation of reactivity device incremental cross sections consists of a multistep process. This multistep process involves first completing 2D lattice calculations with fully explicit cluster representation of fuel and complete neutron energy group structure, followed by annularization of the fuel bundle and reactivity device and the use of equivalent material mixtures in two-bundle-model 3D supercell calculations.

It is noteworthy that this dissertation calculates incremental cross sections using both a detailed cluster model and an annularized model of the 37-element fuel to investigate differences between the two sets of calculated cross-section increments.

3.6 Assessment Methods for Advanced Fuel Designs

In addition to the standard 37-element fuel bundle, many other fuel designs have been assessed for suitability in CANDU reactors. These fuels can be broadly

categorized as enriched uranium fuel, recovered uranium fuel, mixed oxide fuel (MOX) fuel, thorium fuel and actinide burning fuel [55].

3.6.1.1 Enriched Uranium Fuel

This type of fuel uses ^{235}U as the initial fissile material that has been enriched, typically to less than 5%. During the late 1900s and early 2000s, CANDU reactor designers seriously considered using enriched fuels in designs such as the ACR-1000 [56] and in low void reactivity fuels (LVRF) [57].

In Reference [58], the authors studied the CANFLEX bundle with 2 wt% enriched uranium and 4.6 wt% dysprosium in the central pin using WIMS-AECL. The main intent of the study was to develop an advanced fuel design with more desirable reactivity feedback, specifically the coolant void reactivity.

A very interesting study was performed in Reference [59], where the authors compared the results from the standard WIMS-AECL, DRAGON and RFSP calculations with the experimental results obtained from the Zero Energy Deuterium (ZED-2) critical facility at AECL Chalk River Laboratories. Two types of reactivity control devices were tested using the LVRF type fuel bundles (similar to the ACR CANFLEX fuel) inside the ZED-2 critical facility. Two-group homogenized cross sections to be used in the diffusion code were determined based on the WIMS-AECL calculation using both single-cell and multi cell models. DRAGON was used to calculate the macroscopic, incremental two-group cross sections for reactivity devices. In the DRAGON model, the fuel channel was represented by a stylized geometry consisting of a homogenized cylindrical region of fuel and coolant and a surrounding annulus,

consisting of the pressure tube, gas annulus gap and calandria tube. The use of WIMS-AECL/DRAGON/RFSP based standard method gave biases in device worths that were within 0.3 mk of measured values.

3.6.1.2 Recovered-Uranium Fuel

Recovered-Uranium (RU) fuel consist of reprocessed LWR fuel to recover unused uranium. The RU is reused to make new uranium-based fuel. Fresh uranium can also be added where necessary. The ^{235}U content of RU depends mainly on initial enrichment and discharge burnup of LWR fuel. Conventional fuel reprocessing technologies can yield very pure RU with very few contaminants from fission products. Residual fissile material is also available in used CANDU fuel, however the fissile content of used fuel from CANDU is much lower than that of the used enriched fuel from LWRs. Therefore, the recovery of residual fissile material from used CANDU fuel would be significantly more expensive.

The authors of References [60] and [61] have described the salient attributes of RU fuel from CANDU's perspective. Reference [60] provides an assessment of the impact from extra isotopes in RU by performing lattice and core simulation using 0.9% SEU, as being representative of RU. WIMS-AECL was used to create a representative model for generating lattice cross sections as a function of bundle-average burnup for 0.9 % SEU.

Various types of RU based fuel have been looked at for use in CANDU reactor. These fuels differ in the level of reprocessing performed to the LWR-discharged fuel as well as the nature of additional fuel material added for reactivity control. In the

direct use of spent PWR fuel in CANDU (DUPIC), the spent fuel is directly reused in a

CANDU reactor after a short reprocessing using dry mechanical methods to remove

gaseous fission products. The DUPIC fuel provides excellent uranium utilization,

high-level waste reduction per electricity generation and the proliferation resistant

feature since the plutonium residing in the used fuel is not separated [62], [63].

In another fuel design known in the industry as natural uranium equivalent

(NUE), a mixture of pure RU from spent fuel reprocessing technologies and depleted

uranium (DU) from enrichment tails is combined in a 37-element fuel bundle design

such that the resulting fuel will behave similar to the SCB. The composition of NUE is

~70% of 0.85 wt% to 0.99 wt% of RU and ~30% of ~0.2 wt% to 0.3 wt% of DU [64].

The composition of RU and DU in the fuel are selected such that the initial bundle

reactivity between the NU and SCB is equivalent. In Reference [65], the authors used

the two lattice codes WIMS-AECL and DRAGON to calculate the fuel bundle power

distribution for each ring based on two-group cross section properties for NEU fuel.

3.6.1.3 Mixed Oxide Fuel

In MOX fuel, plutonium recovered through reprocessing spent LWR fuel is

mixed with either fresh or DU to make mixed uranium- and plutonium-oxide (MOX)

fuel [66]. The main benefit of this fuel type is that it has the potential to allow for

utilization of significant amounts of high-grade plutonium from dismantled nuclear

warheads.

The authors of Reference [67] evaluated both solid and annular fuel pins

comprised of plutonium/uranium-based MOX fuel arranged in various forms of

square array using the lattice code DRAGON. The code was used to study nuclear

fission rate density, multiplication factor, fuel and moderator reactivity feedback

parameters, and production/depletion of isotopes for different burnup periods.

3.6.1.4 Thorium Fuel

Thorium is a fertile element that is more abundant than uranium in the earth's

crust. Therefore, the use of thorium as a primary energy source in nuclear reactors

has been a tantalizing prospect for many years [68]. Thorium fuel needs a fissile

material, such as ^{235}U or ^{239}Pu as a 'driver' so that chain reaction can be maintained.

Thorium fuel can be either first irradiated in a reactor to provide the necessary

neutron dosing followed by the separation of fissile ^{233}U for use in new fuel, or the

^{233}U may be usable 'in-situ' in the same fuel form. In the CANDU reactor, a

once-through thorium cycle is economically viable, which enables energy to be

derived from ^{233}U without reprocessing and recycling. A wide variety of

thorium-based fuel designs have been proposed for used in CANDU reactors which

incorporates the use of LEU oxide with thorium oxide fuel elements in a 43-element

or 37-element fuel bundle layout. These fuel designs vary on the source and quantity

of the fissile component (^{233}U, ^{235}U or plutonium) and how the fissile component is

arranged with the fertile thorium.

The authors of Reference [69] proposed the use of the standard method for

analysis of the 43-element based thorium-fuelled CANDU reactor. It was concluded

that the codes developed for assessment of NU fuel can also be used for reactor

physics analysis of the thorium-based CANDU, namely the use of WIMS-AECL with

ENDF/B-VII derived nuclear data library for calculation of macroscopic, cell-averaged 2-energy-group cross sections, and DRAGON for derivation of reactivity device incremental cross sections. The use of RFSP for three-dimensional calculations of neutron flux and power density distributions in a reactor core, and a Monte Carlo based code for the purpose of benchmarking the aforementioned toolset was also put forward.

The authors of References [70], [71] studied the impact of introducing small amounts of thorium into the traditional 37-element fuel bundle as well as a modified 37-element fuel bundle comprising of slightly enriched uranium fuel and a thorium central element. In Reference [70], a series of 2D WIMS-AECL simulations using approximate models was carried out as part of conceptual scoping studies to evaluate the potential performance and safety characteristics of thorium-based fuel including possible reduction in coolant void reactivity. A 89-group nuclear data library based on the ENDF/B-VII.0 evaluation was used in conjunction with WIMS-AECL. In Reference [71], both WIMS-AECL based depletion simulations and RFSP-based full-core time-average diffusion simulations were carried out to evaluate various characteristics of introducing thorium in the core. It was concluded that introducing thorium in the 37-element bundle can provide increased margin to maximum bundle power limit and significant increase in fissile utilization.

3.6.1.5 Actinide Burning Fuel

The reprocessing of spend fuel and extraction of actinide materials for use in fuel for reactors is a key component in reducing the end waste from plant operations.

Many transuranic actinides in nuclear spent fuel produce heat for long durations, resulting in significant nuclear waste management challenges. Fissioning some of the long-lived actinides from used LWR fuel and blending with a fuel matrix such as uranium, thorium or a neutronically inert material such as zirconia and use as fuel in CANDU reactors has been examined by authors in Reference [72]. It was reported that resulting waste would significantly lower decay heat and radiotoxicity, and simplify the waste management. In Reference [72], lattice cell calculations using WIMS-AECL with a library with nuclear data for nuclides up to atomic number 96 and full-core models using RFSP were performed to study the utilization of a CANDU reactor for actinide destruction and to assess the impact on normal operations due to deviation from normal fuelling scheme.

The authors of References [73] and [74] use the lattice transport code DRAGON to perform neutronic assessment on transuranic mixed oxide fuel (TRUMOX) with 95.25% natural uranium and 4.75% of actinide mixture in a 43-element bundle design that features a larger diameter center pin containing a burnable dysprosium-zirconium poison. In Reference [73], 2D burnup and 3D incremental simulations for reactivity worth of an adjuster rod were performed. Additionally in Reference [74], 2D DRAGON simulations for study of the coolant void reactivity for TRUMOX fuel were performed. The 2D simulations used a detailed lattice geometry with resonance self-shielding for the 43-element TRUMOX fuel. The 3D simulations used a simplified fuel model depicting the 43-element bundle as two regions consisting of homogenized fuel + coolant paste in the centre and the surrounding pressure tube + gap + calandria tube paste.

The literature review of reactor physics methods confirms overall that the use of advanced transport codes for 2D lattice, 3D supercell and diffusion codes for full-core calculations is deemed acceptable for advanced CANDU fuel designs.

Chapter 4: Reactivity Feedback Effects of Molybdenum Producing Bundle

The time dependence of core power during a transient induced by perturbing core parameters from their reference, steady-state, values is determined, primarily, by the core reactivity which is the difference between the reactivity of the perturbed core and the reactivity of the steady-state core. Consequently, when a single parameter is perturbed, the transient behavior is determined by the difference between the reactivity of the perturbed core and the reactivity of the reference core, also known as the reactivity effect of that parameter. To compare the behaviour of the MPB to that of the SCB under transient conditions, a first step is to compare their respective reactivity effects due to changes in local core parameters such as coolant density, moderator density, coolant temperature, moderator temperature, fuel temperature and moderator poison concentration. This chapter calculates and compares the reactivity effects of the two bundles under investigation over a wide range of perturbations in coolant density, moderator density, coolant temperature, moderator temperature, fuel temperature and moderator poison concentration (boron and gadolinium), for burnups ranging from fresh to discharge burnup. A detailed investigation into the observed dissimilarities between the MPB and SCB reactivity feedback coefficients based on linear perturbation theory is provided.

4.1 Reactivity Feedback Effects Methodology

The reactivity feedback effects are calculated for both bundle types by perturbing the following parameters around reference values that are representative of core conditions, and taking the difference between the reactivity of the perturbed lattice cell and that of the reference, unperturbed, one:

i.   Coolant temperature

ii.   Moderator temperature

iii.   Coolant density

iv.   Moderator density

v.   Fuel temperature

vi.   Moderator poison concentration

The reference values, perturbation ranges and perturbation steps of the parameters for which reactivity effects are calculated are presented in Table 4-1. When calculating the reactivity effect for each parameter, only the parameter under consideration is varied while the remaining parameters are held constant at their reference values; even if the resulting combination of parameters is unphysical, e.g., varying fuel temperature without simultaneously changing fuel density. The described, strictly parametric approach, has the advantage that it can be utilized to predict the reactivity effect of any physical combination of (small) parameter changes by simply adding the individual effects for all perturbed parameters.

Table 4-1: Reference and Perturbed Values for MPB and SCB Lattice Parameters

Parameter	Unit	Reference Value	Perturbation Range	Increment
Coolant Temperature	K	583.15	[300, 650]	50
Moderator Temperature	K	346	[300, 500]	25
Coolant Density	g/cm³	0.830	[0.0, 1.0]	0.1
Moderator Density	g/cm³	1.083	[0.4, 1.2]	0.1
Fuel Temperature Outer Surface	K	681	[750, 1050]	100
Moderator Poison Boron Gadolinium	ppm ppm	0 0	[0,10] [0,4]	1.0 0.5

The reactivity effects are calculated for each parameter at burnups of 0 MWd/t(U), 906.62 MWd/t(U), 3750 MWd/t(U), and 7500 MWd/t(U), which are selected to represent zero burnup, 20-day burnup, mid-burnup, and discharge burnup conditions, respectively. A burnup of 906.62 MWd/t(U) corresponds to 20 days of irradiation at the specific power of 45.33 kW/kg (based on a bundle power of 900 kW). This burn up is sufficient to reach the maximum activity of ^{99}Mo in the fuel pins. Beyond 20 days, the rate of production of ^{99}Mo in the fuel pins balances the rate at which ^{99}Mo is lost due to radioactive decay [9]. Irradiation for longer than 20 days does not increase the amount of produced ^{99}Mo and is uneconomical due to the accumulation of other undesirable fission products and the increase in the radioactive waste streams that ultimately require disposal. The higher MPB burnups are only included in the study to account for the possibility of the MPB inadvertently spending more time in the core than planned.

4.2 Transport Code and Model

The neutron transport code DRAGON ver. 3.06 [25] is used for this study. For the current analysis, the technique of collision probabilities was applied to a two-dimensional model with material cross sections derived from the 69-group IAEA WLUP library [53]. The flux was normalized to a total production rate of one neutron per second and the adjoint was also normalized to an adjoint-weighted production rate of unity.

The DRAGON model used in this study is a single lattice cell corresponding to either the SCB or the MPB with reflective boundaries on all sides. The pressure tube is modelled as an alloy of natural zirconium with 2.5% niobium, while the calandria tube is modelled as pure natural zirconium. Within a single-lattice pitch (28.575 cm) square region, unpressurized heavy water moderator at a significantly lower temperature (345 K) surrounds the calandria tube. Each fuel pin consists of a string of UO_2 pellets that is encapsulated by a layer of cladding. The SCB fuel pins have a density of 10.6 g/cm^3 and 0.711 wt% enrichment of ^{235}U, corresponding to natural uranium. The MPB fuel pins have a density of 10.6 g/cm^3. The inner-region UO_2 fuel contains depleted uranium, with 0.2 wt% of ^{235}U. The outer-region UO_2 fuel contains 19.5 wt% of ^{235}U. The thickness of the outer, enriched-uranium, region of the pin is 79.36 μm, which is adapted from the work of Reference [3].

Resonance treatment is performed using the modified Stamm'ler method [75] and 11 distinct radial resonance domains in the fuel. The inner, depleted-fuel, region of the MPB is split into 10 radial material regions and 10 distinct resonance domains,

and the outer, enriched-fuel, region consists of 1 material region and a single resonance domain. The high number of spatial regions and the 11 resonance domains in the fuel pin are used to capture the self-shielding effects and the so-called 'rim effect', which represents the higher neutron absorption at the periphery of the fuel pin with better accuracy. The use of multiple material regions with additional regional splitting (for a total of 23 radial computational regions) ensures that the evolution of the fuel composition during burnup is captured in detail in the transport calculation and that sufficiently-fine radial power profile data is available. The SCB model is geometrically identical to the MPB one, but all fuel regions contain natural uranium. The DRAGON geometrical model used in this study is shown in Figure 4-1.

One important difference between the SCB and MPB is the radial fuel temperature profile. The fuel temperatures in each discrete region of the pin are set, for each bundle type, according to the radial temperature profiles shown in Figure 4-2, which are calculated using the methodology employed in Reference [3]. The modelling of the radial variation in the fuel temperature ensures more accurate predictions of the reactivity feedback compared to the use of a uniform fuel temperature as typically done in lattice calculations.
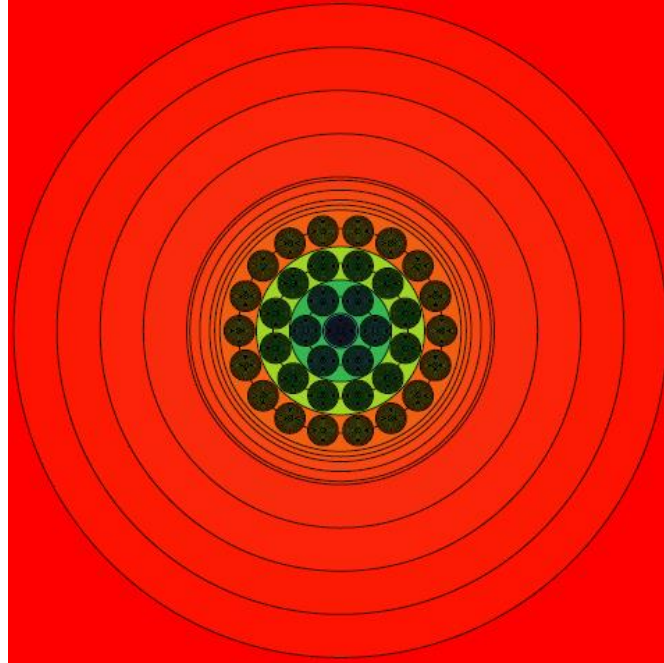
Figure 4-1: A DRAGON representation of the CANDU lattice discretized into material regions

Figure 4-2 shows that the fuel centreline temperature of the MPB is significantly lower than that of the SCB for all burnups. The difference in the centreline temperatures for the two bundles is due to the fact that the temperature difference between the center of the pin and the outer surface of the pin is, by and large, proportional to the radial integral of the heat flux between the outer surface of the pin and the centerline. While the two bundle types have the same outer fuel temperature, set by the coolant temperature, the increase in temperature towards the center of the pin is much more pronounced for the SCB than for the MPB. At zero burnup, this is due to the fact that, for the SCB, heat is generated fairly uniformly throughout the fuel while, for the MPB, the vast majority of the heat is generated in the outer, enriched, fuel region, and therefore the integration distance in the heat flux

component is much shorter for the MPB pin compared to the SCB pin with uniform

heat generation. Figure 4-3 shows a step increase in the power density in the

enriched-uranium region of the MPB for fresh fuel conditions. As the MPB is

irradiated, heat generation in the enriched peripheral region decreases due to ^{235}U

depletion, and increases in the central region as ^{238}U is converted to fissile ^{239}Pu. This

gradual shift in heat generation from the peripheral region to the inner region of the

pin causes the MPB centreline temperature, and radial temperature profile in general,

to rise with burnup. However, the MPB fuel temperature at any radial position still

remains lower than that of the SCB.
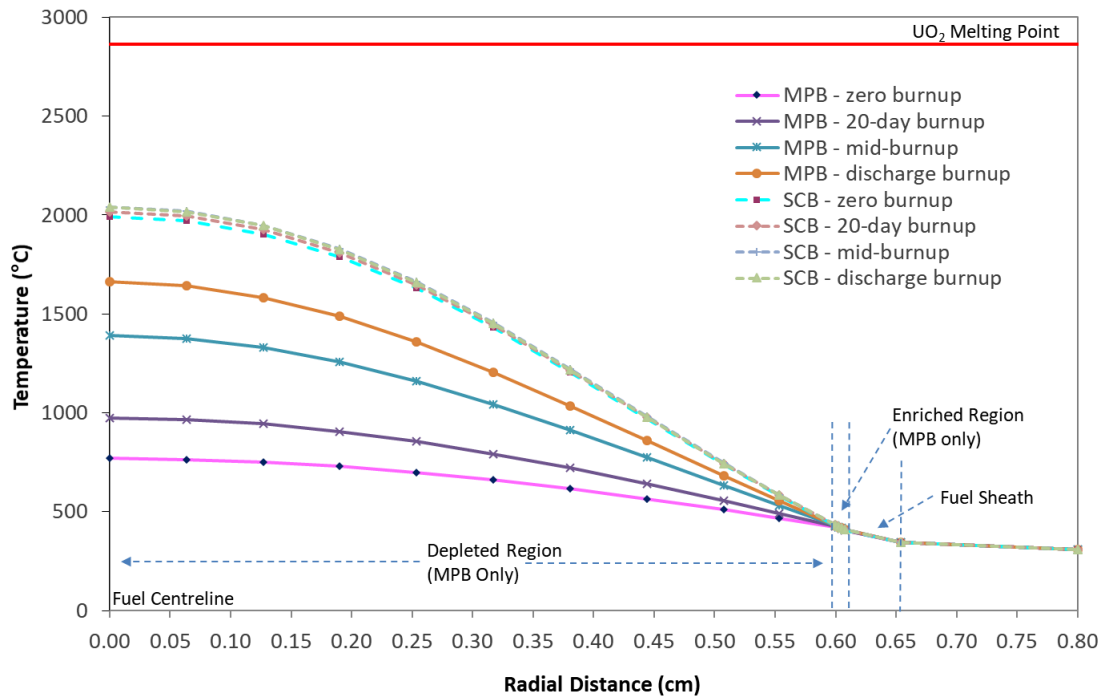
Figure 4-2: Radial temperature profiles of MPB and SCB for various burnups [3]
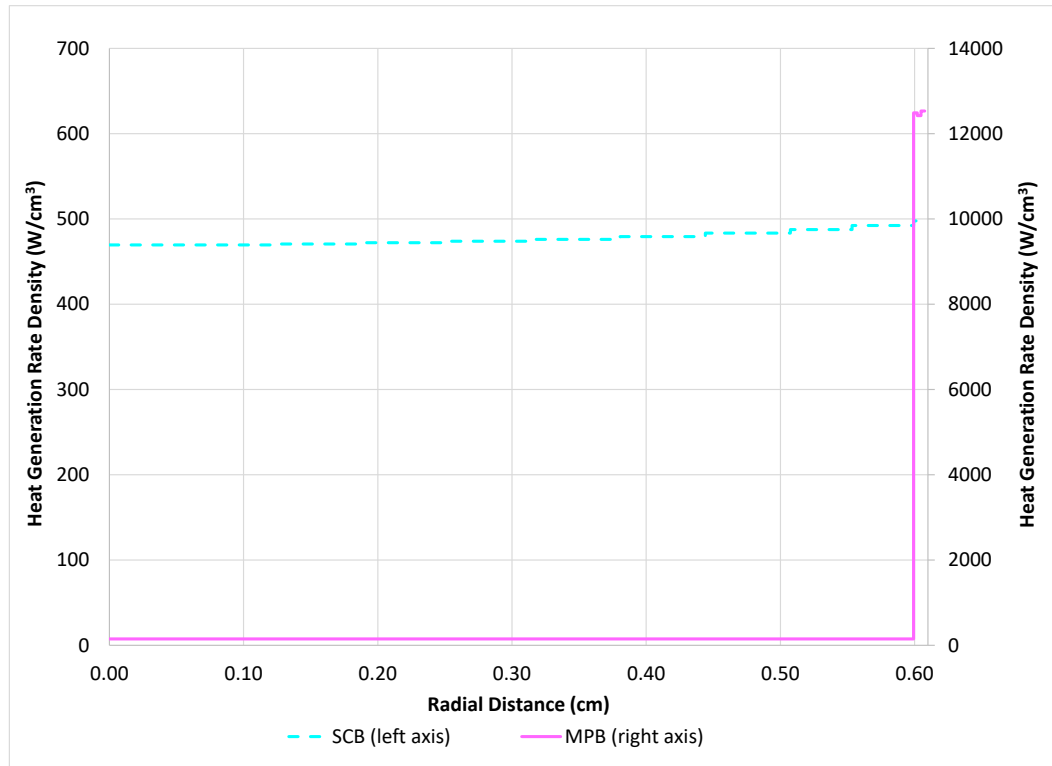
Figure 4-3: Normalized heat generation rate density for SCB and MPB fuel pins

Starting from the fresh fuel conditions, the fuel burnup is advanced using burnup steps of less than 250 MWd/t(U) until a burnup of 1250 MWd/t(U) was reached. The burnup steps are kept small in order to capture the initial, sharp decline of the reactivity due to the accumulation of saturating fission products, followed by its subsequent rise resulting from plutonium buildup. Beyond the irradiation stage of 1250 MWd/t(U), larger burnup steps (375 MWd/t(U) and 625 MWd/t(U)) are used to reach the mid-burnup and discharge burnup stages. All parameters are kept at their reference conditions during the burnup evolution.

The lattice model assumes reflective boundary conditions for all transport calculations. For each parameter listed in Table 4-1, the infinite-medium multiplication constants for the reference state and for each perturbed state are used to calculate the reactivity feedback effect using Eq. (4.1).

$$\Delta\rho_i = 1000 \times \left(\frac{1}{k_{\text{inf},0}} - \frac{1}{k_{\text{inf},i}} \right)(mk) \qquad\qquad (4.1)$$

4.3 Calculations and Results

The following sections describe the impact of perturbing the key parameters about their reference values listed in Table 4-1.

4.3.1 Coolant-Temperature Reactivity Effect

The coolant temperatures simulated in DRAGON range from 300 K to 650 K in increments of 50 K for all four burnup cases: zero burnup, 20-day burnup, mid-burnup and discharge burnup. The reference coolant temperature used to calculate the reactivity change in Eq. (4.1) is 583.15 K.

The calculated effect of coolant temperature on reactivity for SCB and MPB lattice models is presented in Figure 4-4. The coolant temperature perturbations yield reactivity differences that display smooth variations, which are very similar for both MBP and SCB for all four burnups. The slight differences in reactivity between the two fuel types remain below 1 mk over the entire coolant-temperature perturbation range.

For the perturbation range analyzed, the maximum difference in reactivity occurs at 300 K coolant temperature for 20-day burnup, followed by mid-burnup, zero burnup and then discharge burnup. The differences at higher-than-reference coolant temperatures are much less pronounced for the given perturbation range. The shifting of the curves from downwards trending for zero burnup and 20-day burnup to upwards trending for mid-burnup and discharge burnup as the coolant temperature is increased is a recognized effect and it occurs for both the MPB and the SCB.
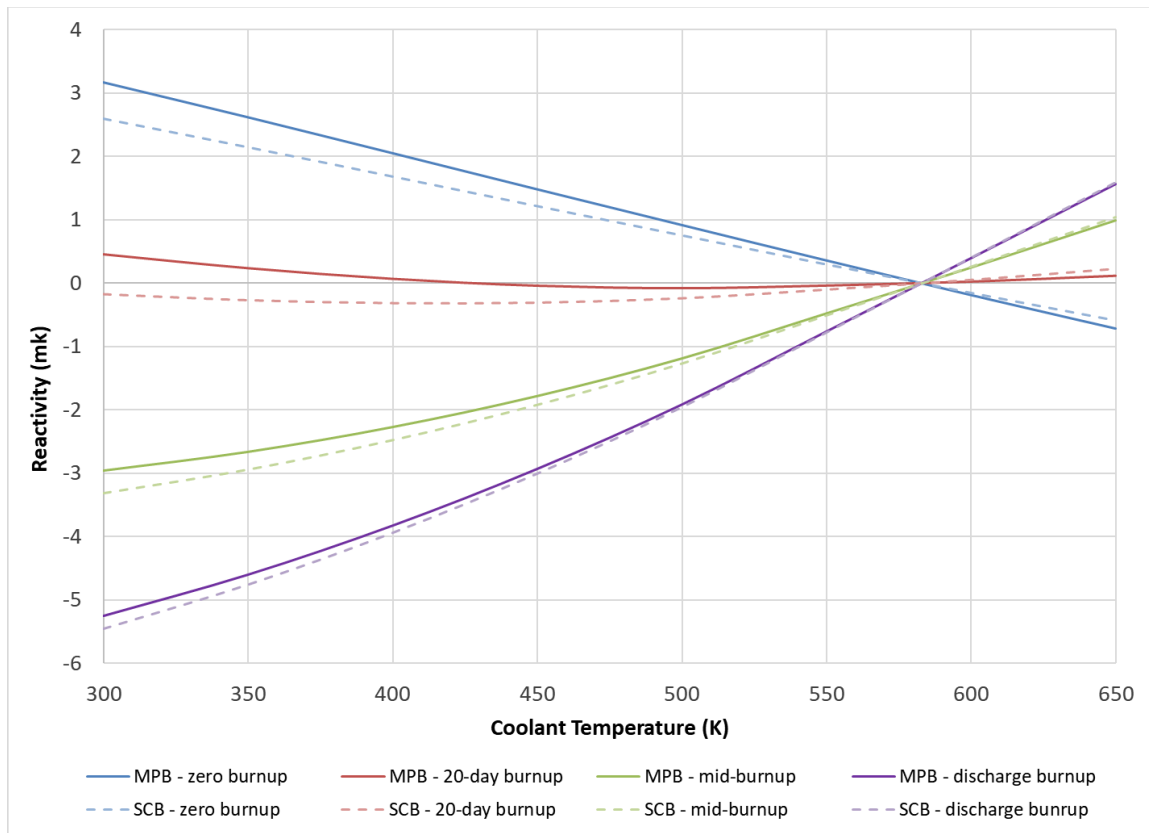
Figure 4-4: Coolant-temperature reactivity effect for MPB and SCB

4.3.2 Moderator-Temperature Reactivity Effect

The moderator temperature simulated in DRAGON range from 300 K to 500 K in increments of 25 K for all four burnups. The reference temperature used to calculate the reactivity change in Eq. (4.1) is 346 K.

The calculated effect of the moderator temperature on reactivity for SCB and MPB lattice models is presented in Figure 4-5. The moderator temperature perturbations yield reactivity differences that display almost linear trends, and are very similar for both MBP and SCB for all four burnups. The reactivity effects are nearly-identical for zero burnup. The slight differences in the reactivity values for 20-day burnup, mid-burnup and discharge burnup are below 1 mk for the entire moderator-temperature perturbation range.

For the perturbation range analyzed, the maximum reactivity difference occurs at 500 K moderator temperature for 20-day burnup, followed by mid-burnup, discharge burnup and then zero burnup. The differences at the lower-than-reference temperature range are much less pronounced for the given perturbation range. The shifting of the curves from downwards trending for zero burnup to upwards trending for 20-day burnup, mid-burnup and discharge burnup as the moderator temperature is increased is a recognized effect and it occurs for both the MPB and the SCB.
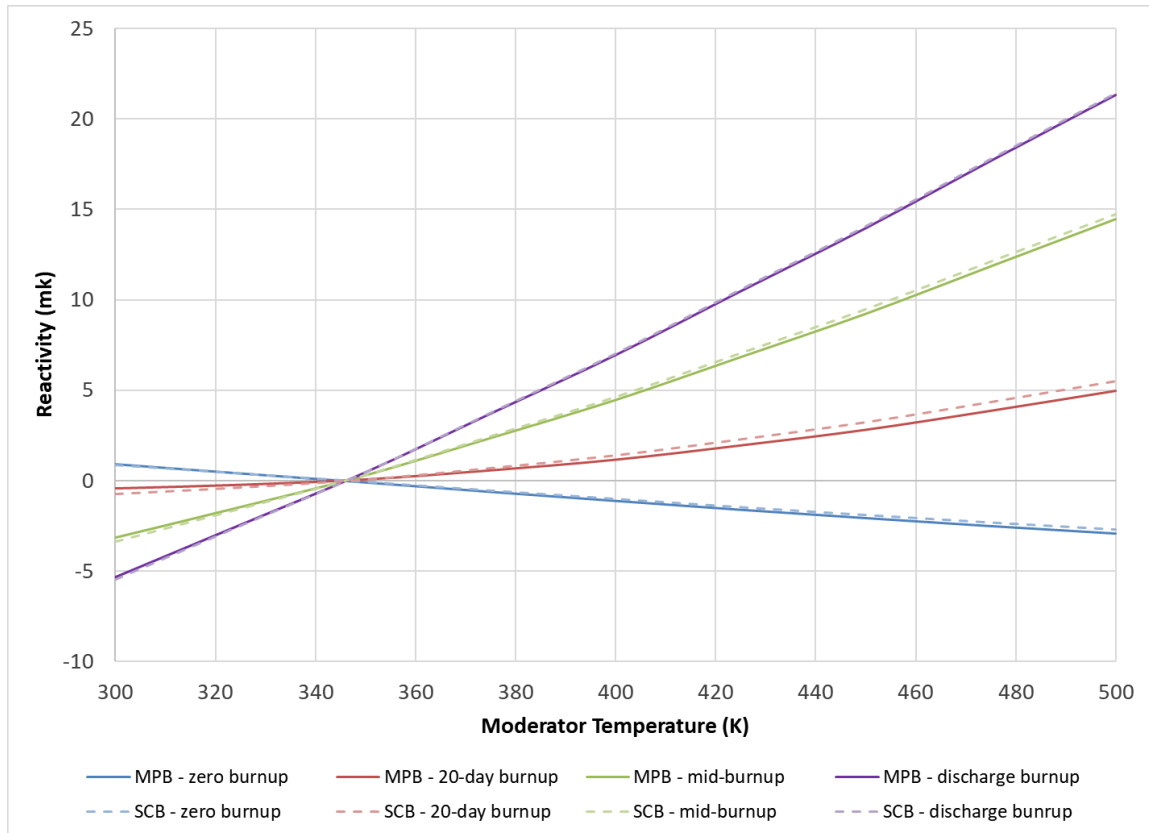
Figure 4-5: Moderator-temperature reactivity effect for MPB and SCB

4.3.3   Coolant-Density Reactivity Effect

The coolant densities simulated in DRAGON range from 0.0 g/cm^3 to 1.0 g/cm^3 in increments of 0.1 g/cm^3 for all four burnups. The reference density used to calculate the reactivity change in Eq. (4.1) is 0.830 g/cm^3.

The calculated effect of the coolant density on reactivity for SCB and MPB lattice models is presented in Figure 4-6. It is evident that coolant density perturbations yield reactivity differences that display linear trends, and are nearly-identical for the

two fuel types for all four burnups. The slight differences in reactivity between the

two fuel types remain below 1 mk over the entire coolant-density perturbation range.
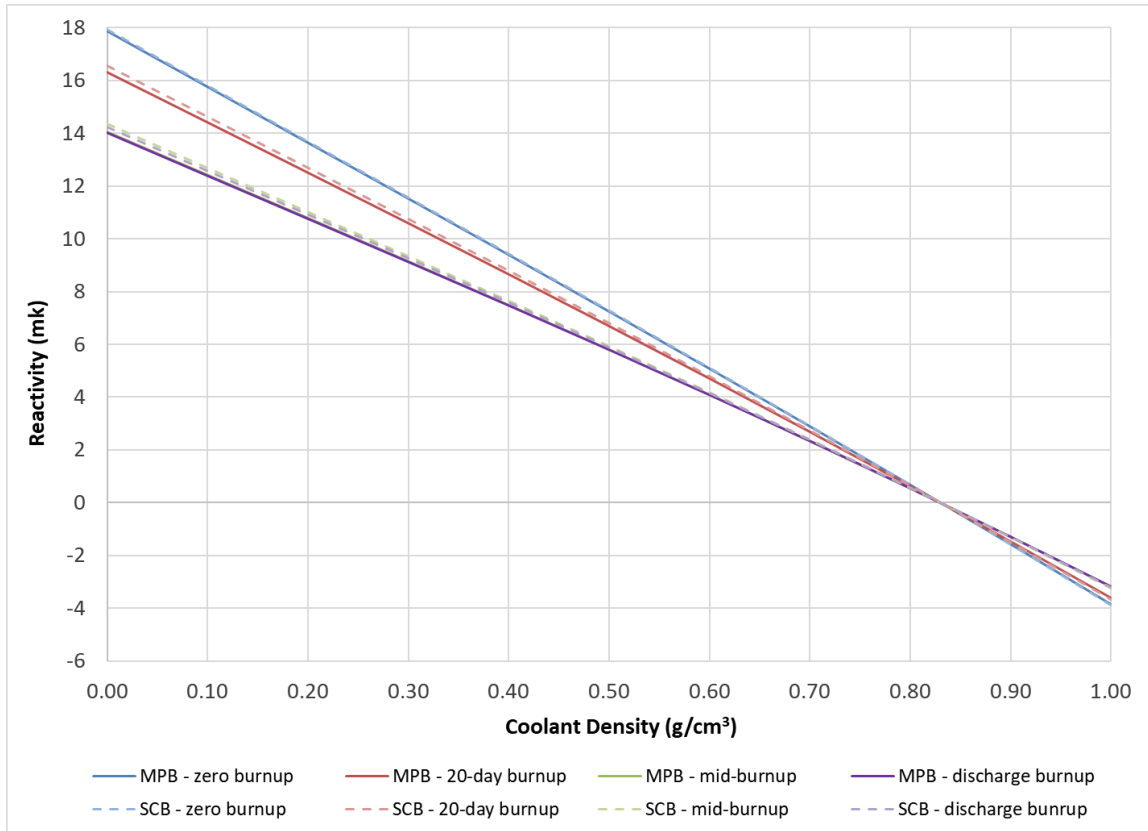
Figure 4-6: Coolant-density reactivity effect for MPB and SCB

For the perturbation range analyzed, the maximum reactivity difference

between the two fuel types occurs when coolant density is 0 g/cm³ (fully voided

conditions) for discharge burnup, followed by mid-burnup, 20-day burnup and then

zero burnup. The differences at the higher-than-reference density range are much

less pronounced for the given perturbation range. For voided conditions, the highest

positive reactivity effect for both fuel types occurs for zero burnup, followed by 20-day burnup, mid-burnup, and then discharge burnup.

4.3.4 Moderator-Density Reactivity Effect

The moderator densities simulated in DRAGON range from 0.4 g/cm^3 to 1.2 g/cm^3 in increments of 0.1 g/cm^3 for all four burnups. The reference density used to calculate the reactivity change in Eq. (4.1) is 1.083 g/cm^3.

The calculated effect of the moderator density on reactivity for SCB and MPB is presented in Figure 4-7. The moderator density perturbations yield reactivity differences that display smooth variations, which are very similar for MBP and SCB for all four burnups considering that for 0.4 g/cm^3 moderator density, the calculated reactivity value lies between -280 mk and -345 mk.

For the perturbation range analyzed, the maximum difference in reactivity between the two fuel types occurs at 0.4 g/cm^3 moderator density for discharge burnup, followed by mid-burn, 20-day burnup and then zero burnup. The reactivity effect of loss of moderation is quite significant, as displayed in Figure 4-7 at low moderator density range, since moderator is the main source of thermalized neutrons in the core.
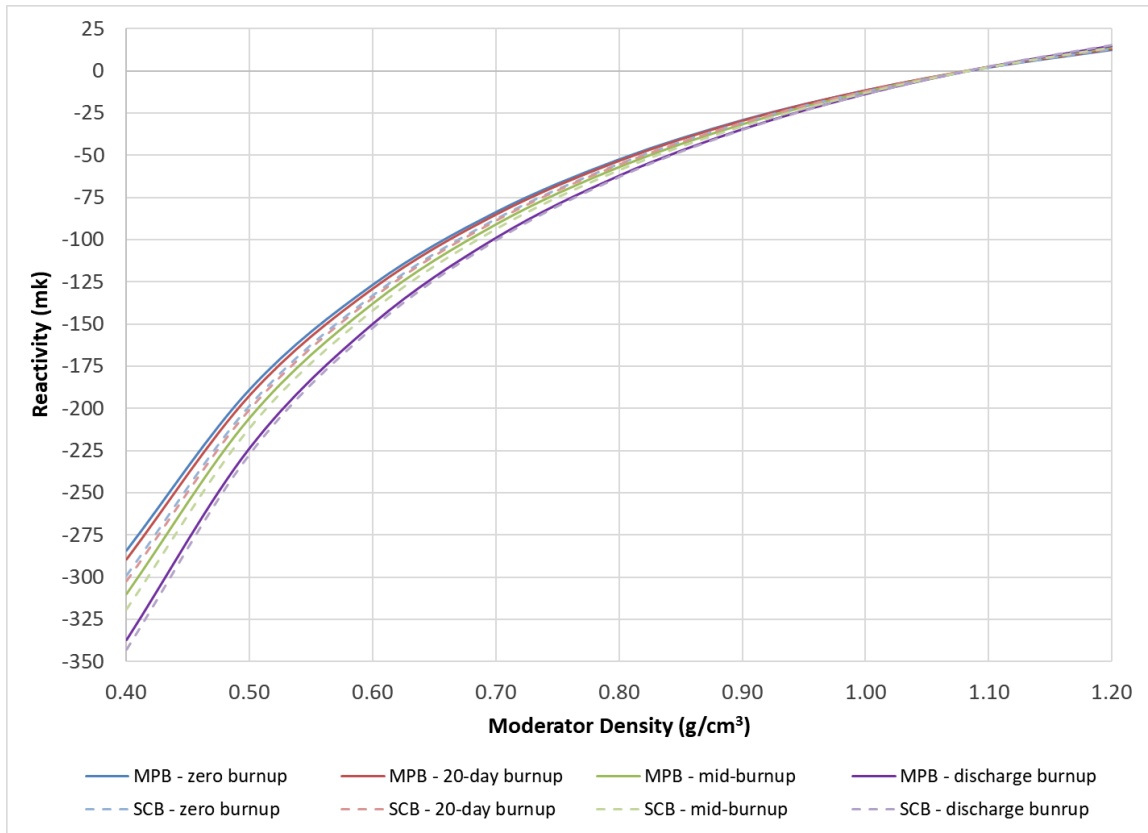
Figure 4-7: Moderator-density reactivity effect for MPB and SCB

4.3.5   Fuel-Temperature Reactivity Effect

When calculating the fuel-temperature reactivity effect, because the radial fuel-temperature profiles of the SCB and MPB are vastly different, using the average fuel temperature as the perturbed parameter is inadequate. Instead, in this study, the perturbed parameter is the fuel pin outer temperature, which is the same for both bundle types (because it is dictated, primarily, by the coolant temperature) and thus allows for a fair comparison. Perturbing the outer fuel temperature from its reference value perturbs the temperature throughout the fuel pin, but by different amounts

depending on the radial position. The radially-dependent fuel-temperature perturbation increases towards the centerline where it can be as high as 2.2 times the perturbation in the outer fuel temperature. For that reason, a different radial temperature profile is calculated for each fuel-temperature perturbation case and for each burnup, accounting for the temperature dependence of the thermal conductivity at each radial position.

The reference fuel temperature profiles corresponding to each of the four burnups, as depicted in Figure 4-2, are simulated in DRAGON. The outer fuel temperature is perturbed from 681 K to 750 K and subsequently to 1050 K in steps of 100 K. As an illustration, Figure 4-8 shows the reference and perturbed fuel temperature profiles for MPB and SCB for fresh fuel. The calculated effect of the fuel temperature on reactivity for SCB and MPB is presented in Figure 4-9.

The horizontal axis in Figure 4-9 denotes the fuel pin outer temperature. The overall fuel-temperature reactivity follows the same general downward trend as the fuel temperature is increased for both fuel types and for all four burnups. The slight differences in reactivity between the two fuel types remain below 1 mk over the entire fuel-temperature perturbation range. For the perturbation range analyzed, the maximum difference in the reactivity among the two fuel types occurs for 1050 K outer fuel pin temperature for zero burnup, followed by mid-burnup, discharge burnup and then 20-day burnup.
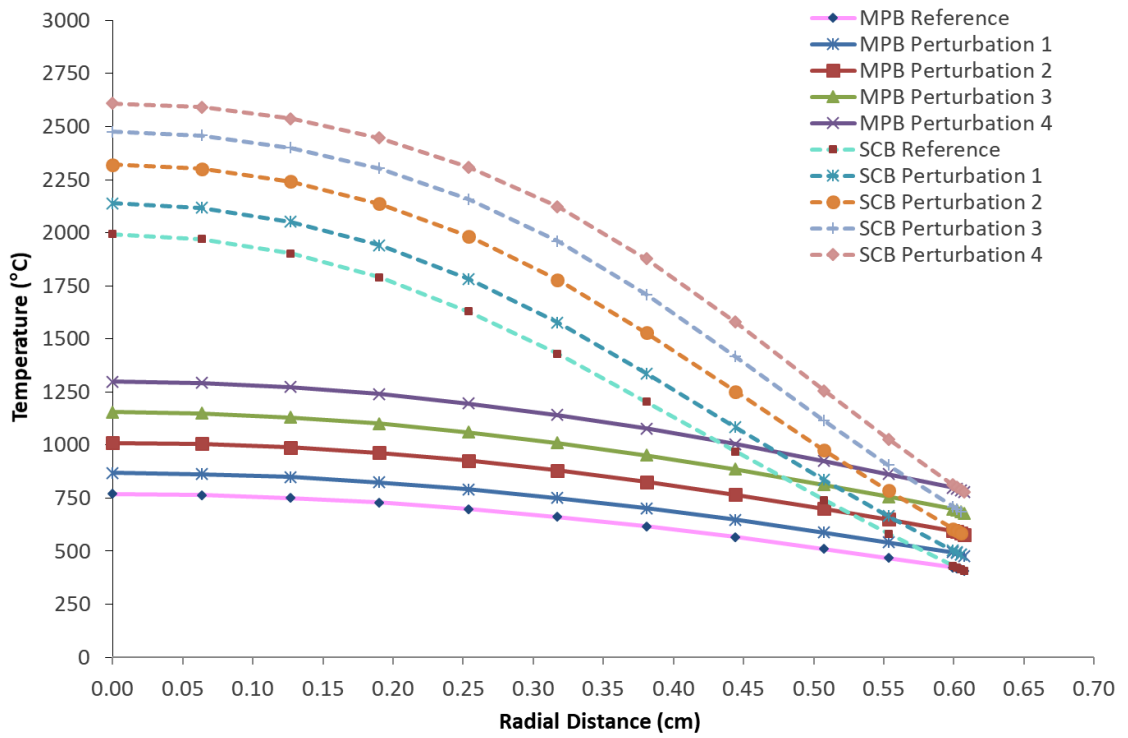
Figure 4-8: Perturbed fuel temperature radial profiles for the fresh fuel case

It can be seen from Figure 4-9 that, for zero burnup, the reactivity effect is slightly more negative for the SCB than the MPB but as the bundles are irradiated, the fuel-temperature reactivity effect becomes to a lesser extent less negative for the SCB than the MPB.
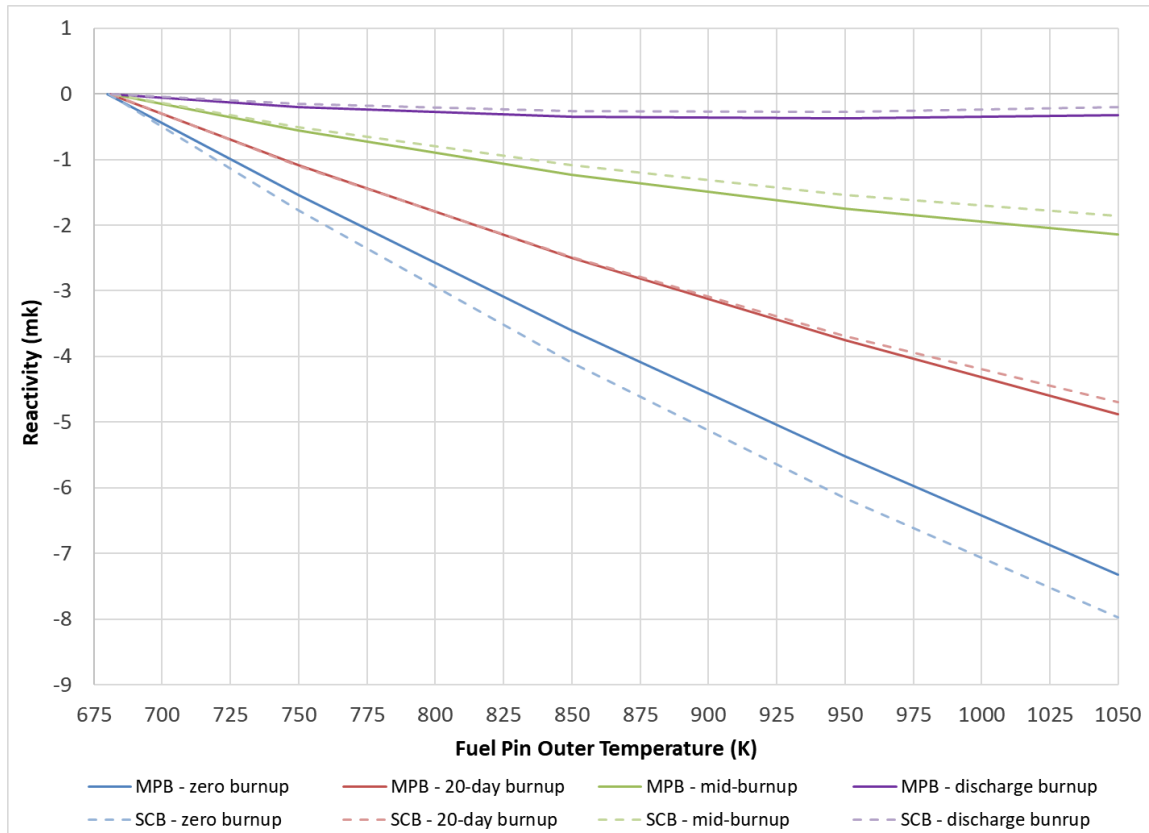
Figure 4-9: Fuel-temperature reactivity effect for MPB and SCB

4.3.6   Moderator-Poison Reactivity Effect

The two poisons that are typically added to the CANDU moderator to control reactivity are natural boron and natural gadolinium. The calculated effects of both boron and gadolinium moderator poisons on reactivity for SCB and MPB are presented in Figure 4-10 and Figure 4-11. Figure 4-10 shows the moderator boron results for boron concentrations between 0 and 10 ppm in increments of 1.0 ppm for all four burnups. Figure 4-11 shows the moderator gadolinium results for gadolinium concentrations between 0 and 4 ppm in increments of 0.5 ppm for all four burnups.

The perturbations induced by both poisons yield reactivity differences that display

linear trends, and are nearly-identical for the two fuel types for all four burnups. For

the perturbation range analyzed, the maximum reactivity difference occurs at the

highest simulated poison concentrations (10 ppm for boron and 4 ppm for

gadolinium), but the difference remains less than 1.5 mk for both boron and

gadolinium poisons at all four burnups. At the highest simulated poison

concentrations, the maximum reactivity difference occurs for zero burnup, followed

by 20-day burnup, mid-burnup and discharge burnup.
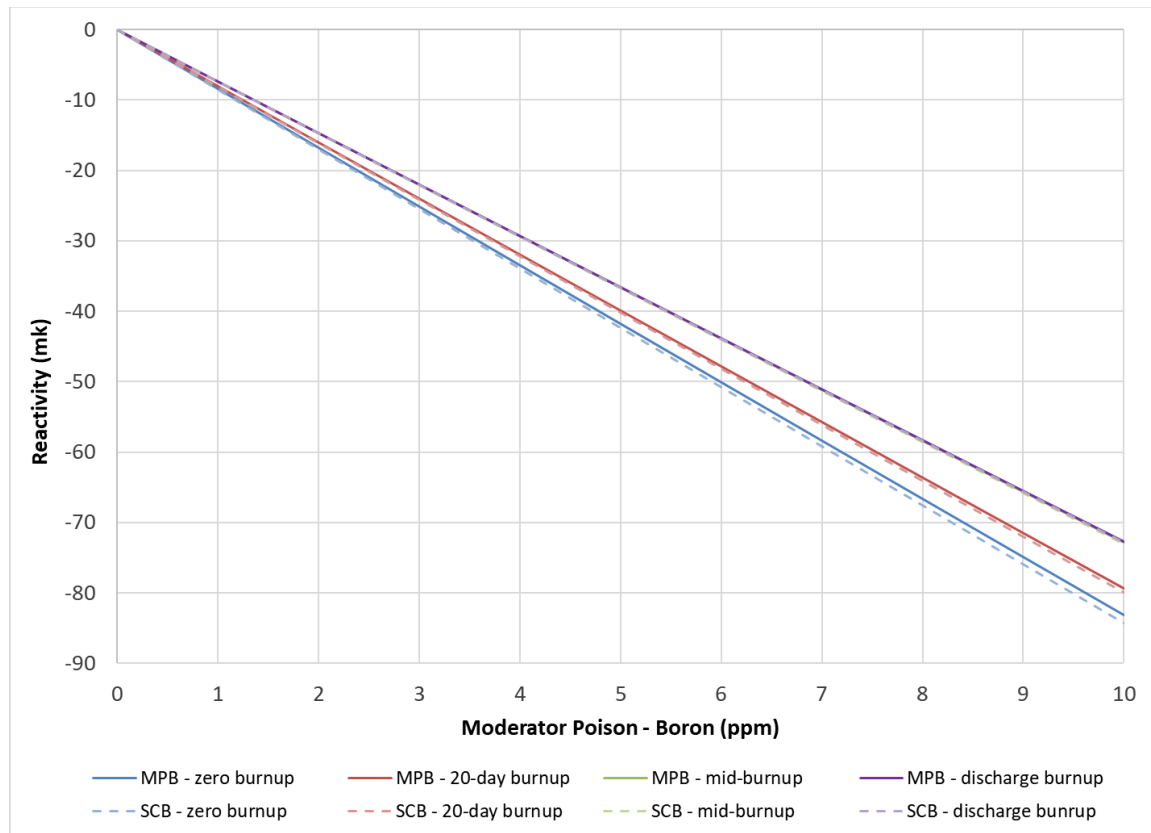
Figure 4-10: Moderator-poison (boron) reactivity effect for MPB and SCB
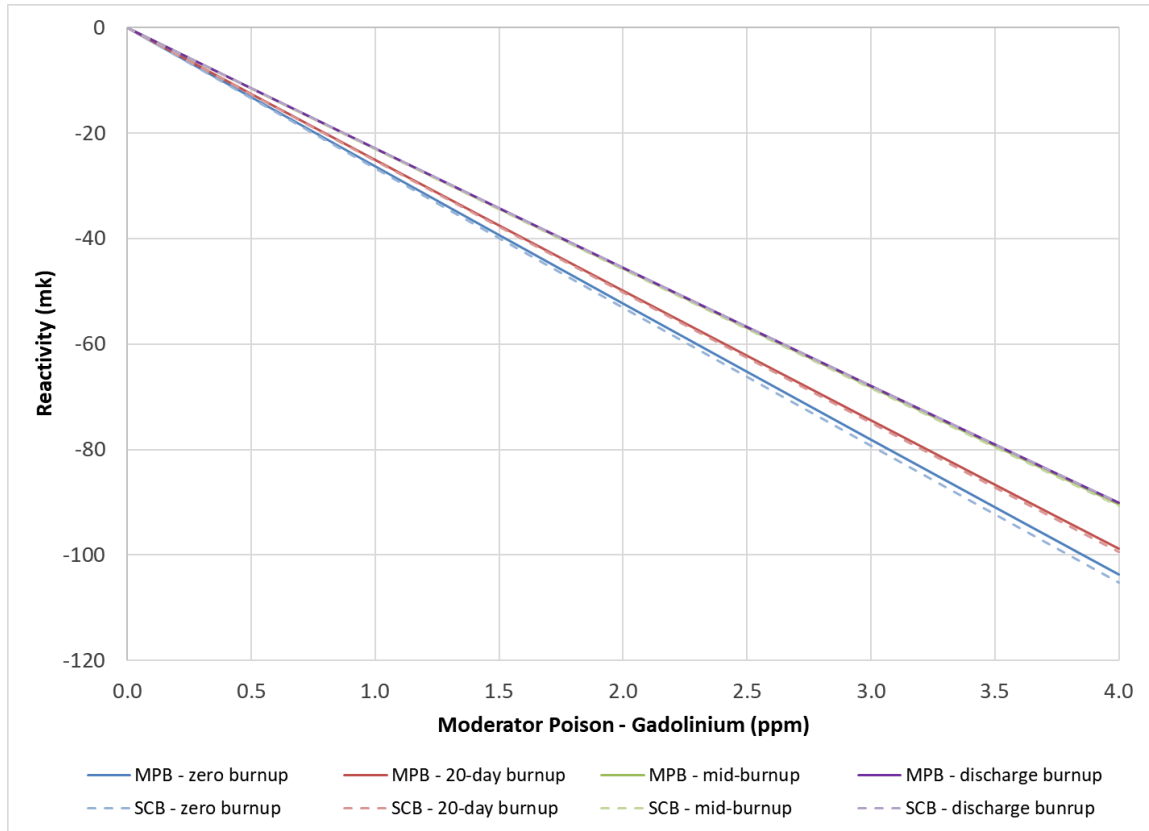
Figure 4-11: Moderator-poison (gadolinium) reactivity effect for MPB and SCB

4.4 Interpretation of Results

The perturbation of any cell parameter, p, results in a change in the cell reactivity. The immediate effect of perturbing a parameter in a specific cell region is a change in the energy-dependent macroscopic cross sections in that region. At the same time, perturbing the macroscopic cross sections in any given region induces changes in the amplitude and energy dependence of the neutron flux in all regions.

Consequently, the overall effect on reactivity is a combination of changes in the production and absorption reaction rates in all regions, not just in the region affected by the initial parameter perturbation.

To gain insight into the correlation between the parametric changes in a specific cell region and the corresponding reactivity effect, one can use the linear perturbation formula of reactivity which is valid for small perturbations, δp, and captures, in synthetic form, the relationship between changes in the energy-dependent macroscopic cross sections in a specific cell region and the corresponding full-cell reactivity effect. In the multigroup collision-probability formalism, the (approximate) reactivity perturbation formula is written as [76]:

$$\delta\rho = \frac{1}{k_{eff}^0} - \frac{1}{k_{eff}} \cong \frac{\sum_{g=1}^{G}\sum_{g'=1}^{G}\sum_{r\in V_{pert}} \Phi_{g,r}^{0*}\Phi_{g',r}^0 V_r \left[\frac{1}{k_{eff}^0}\delta\left(\chi_g \nu\Sigma_{fg',r}\right) + \delta\left(\Sigma_{s,g'\to g,r} - \delta_{g'g}\Sigma_{tg,r}\right)\right]}{\sum_{g=1}^{G}\sum_{g'=1}^{G}\sum_{r\in V_{tot}} \Phi_{g,r}^{0*}\Phi_{g',r}^0 V_r \chi_g^0\Sigma_{fg',r}^0}$$

$$\cong \frac{\sum_{g=1}^{G}\sum_{g'=1}^{G}\sum_{r\in V_{pert}} \Phi_{g,r}^{0*}\Phi_{g',r}^0 V_r \left[\frac{1}{k_{eff}^0}\frac{\delta\left(\chi_g \nu\Sigma_{fg',r}\right)}{\delta p} + \left(\frac{\delta\Sigma_{s,g'\to g,r}}{\delta p} - \frac{\delta_{g'g}\times\delta\Sigma_{tg,r}}{\delta p}\right)\right]}{\sum_{g=1}^{G}\sum_{g'=1}^{G}\sum_{r\in V_{tot}} \Phi_{g,r}^{0*}\Phi_{g',r}^0 V_r \chi_g^0\Sigma_{fg',r}^0}\delta p$$

$$(4.2)$$

In Eq. (4.2), $\Phi_{g',r}^0$ denotes the neutron flux in region r for energy group g', and $\Phi_{g,r}^{0*}$ denotes the adjoint in region r for energy-group g. The "0" superscript denotes the unperturbed (reference) state. Terms preceded by a plain "δ" symbol denote the changes in the respective multigroup macroscopic cross sections induced by the

specific perturbation δp in parameter p, and $\delta_{g,g'}$ represents the Kronecker delta

symbol. The adjoint flux is obtained by solving the adjoint formulation of the neutron

transport equation as presented in Eq. (2.15).

The fraction multiplying the perturbation δp represents the partial derivative

of the reactivity effect with respect to parameter p and is referred to as the reactivity

coefficient of parameter p:

$$\frac{\partial \rho}{\partial p} \cong \frac{\displaystyle\sum_{g=1}^{G}\sum_{g'=1}^{G}\sum_{r\in V_{pert}} \Phi_{g,r}^{0*}\Phi_{g',r}^{0}V_{r}\left[\frac{1}{k_{eff}^{0}}\frac{\delta\left(\chi_{g}\nu\Sigma_{fg',r}\right)}{\delta p}+\left(\frac{\delta\Sigma_{s,g'\to g,r}}{\delta p}-\frac{\delta_{g'g}\times\delta\Sigma_{tg,r}}{\delta p}\right)\right]}{\displaystyle\sum_{g=1}^{G}\sum_{g'=1}^{G}\sum_{r\in V_{tot}} \Phi_{g,r}^{0*}\Phi_{g',r}^{0}V_{r}\chi_{g}^{0}\nu\Sigma_{fg',r}^{0}}$$

(4.3)

For example, if p=T_m is the moderator temperature, then the partial derivative

$\frac{\partial \rho}{\partial T_m}$ is referred to as the reactivity coefficient of the moderator temperature. When the

reactivity effect (change) is plotted as a function of the parameter p, the reactivity

coefficient of parameter p represents the slope of that curve.

As shown by Eq. (4.3), the reactivity coefficient depends on the reference direct

flux, the reference adjoint, and the derivatives of individual macroscopic cross

sections with respect to parameter p:

$$\frac{\partial\left(\chi_g \nu\Sigma_{f,g'}\right)}{\partial p} \cong \frac{\delta\left(\chi_g \nu\Sigma_{f,g'}\right)}{\delta p}$$

$$\frac{\partial\Sigma_{tg}}{\partial p} \cong \frac{\delta\Sigma_{tg}}{\delta p} \qquad\qquad\qquad (4.4)$$

$$\frac{\partial\Sigma_{s,g'\to g}}{\partial p} \cong \frac{\delta\Sigma_{s,g'\to g}}{\delta p}$$

According to Eq. (4.3), the reactivity coefficient is just a weighed sum over all energy groups and regions of cross section derivative terms. The weight consists of the product between the reference flux, the reference adjoint, and the region volume, namely $\Phi_{g,r}^{0*}\Phi_{g',r}^{0}V_r$. Accordingly, knowledge of the flux and adjoint flux for the reference case is sufficient to evaluate the first-order change in the reactivity for the perturbed problem provided that terms on the right-hand-side in Eq. (4.4) can evaluated explicitly. The main regions of interest when applying the perturbation formula are the inner fuel region, the outer fuel region, coolant and moderator. Representative plots of the reference flux and adjoint in the four regions of interest are shown in Figure 4-12 to Figure 4-19.

The first thing to notice from the flux plots is that the flux in the fuel regions has two maxima, one in the high-energy range and another in the thermal-energy range. The high-energy maximum corresponds to fast neutrons being emitted in fission reactions, while the thermal maximum corresponds to thermal neutrons produced by slowing down (moderation) in moderator and coolant. The second thing to notice is that the high-energy maximum is absent in the moderator. Because the moderator is farther away from the fuel, and sufficient neutron slowing-down occurs, Figure 4-18

shows no prominent fast flux. In the coolant, both the low-energy and high-energy maxima are visible, but the high-energy maximum is less prominent than in the fuel. The presence of the high-energy maximum in the coolant is explained by the spatial proximity of the coolant to the fuel. Because of the proximity, only a fraction of the fast neutrons produced from fission have the chance to be moderated.

Figure 4-12 and Figure 4-14 show that, for a given bundle type (either SCB or MPB) and a given burnup, the fluxes in the inner and outer fuel regions are similar, with only small differences. This is due to the fact that fuel pins are relatively thin (~1.2 cm) and thus neutrons travelling from one fuel region to the other do not have a high probability of interaction and hence do not undergo much absorption or slowing down. Figure 4-12 and Figure 4-14 also show that, for a given burnup, the differences between the MPB fuel flux and the SCB fuel flux are minor. At zero burnup, the small differences (both in the inner and outer fuel region) are best described as a slight softening (shift towards thermal energies) of the MPB flux compared to the SCB one. This is likely a consequence of the fact that, at zero burnup, most of the fissions in the MPB occur in the (enriched) outer fuel region, closer to the coolant, and hence neutrons produced there have a better chance of being moderated, which leads to a slightly softer spectrum. At discharge burnup, there is almost no difference between the MPB and SCB fuel fluxes. This is likely due to the fact that, as the fuel burns and fissile material (^{239}Pu) is produced in the inner fuel region of the MPB, a significant fraction of fissions in the discharge-burnup of the MPB occur in the inner fuel region, just like for the SCB, and hence there is no enhanced neutron moderation for the MPB compared to the SCB at discharge burnup.

Substantial flux differences exist between discharge burnup and zero burnup and they are visible for both bundle types and for all regions (inner fuel, outer fuel, coolant and moderator). The substantial flux differences between discharge and zero burnup are due to the accumulation of fission products, depletion of ^{235}U and accumulation of ^{239}Pu in the fuel.

An examination of the adjoint plots reveals that there are only minor differences between the MPB adjoint and the SCB adjoint. This is true for all regions (inner fuel, outer fuel, coolant and moderator) and for both zero burnup and discharge burnup. However, just like for the flux, substantial differences exist between the discharge-burnup adjoint and the zero-burnup adjoint for both bundle types and for all regions. These differences are due primarily to the accumulation of ^{239}Pu in the fuel.

In what follows, the perturbation formula in Eq. (4.3) and the observations made about the reference flux and adjoint are used to analyze the reactivity coefficients of specific parameters for the MPB and the SCB.
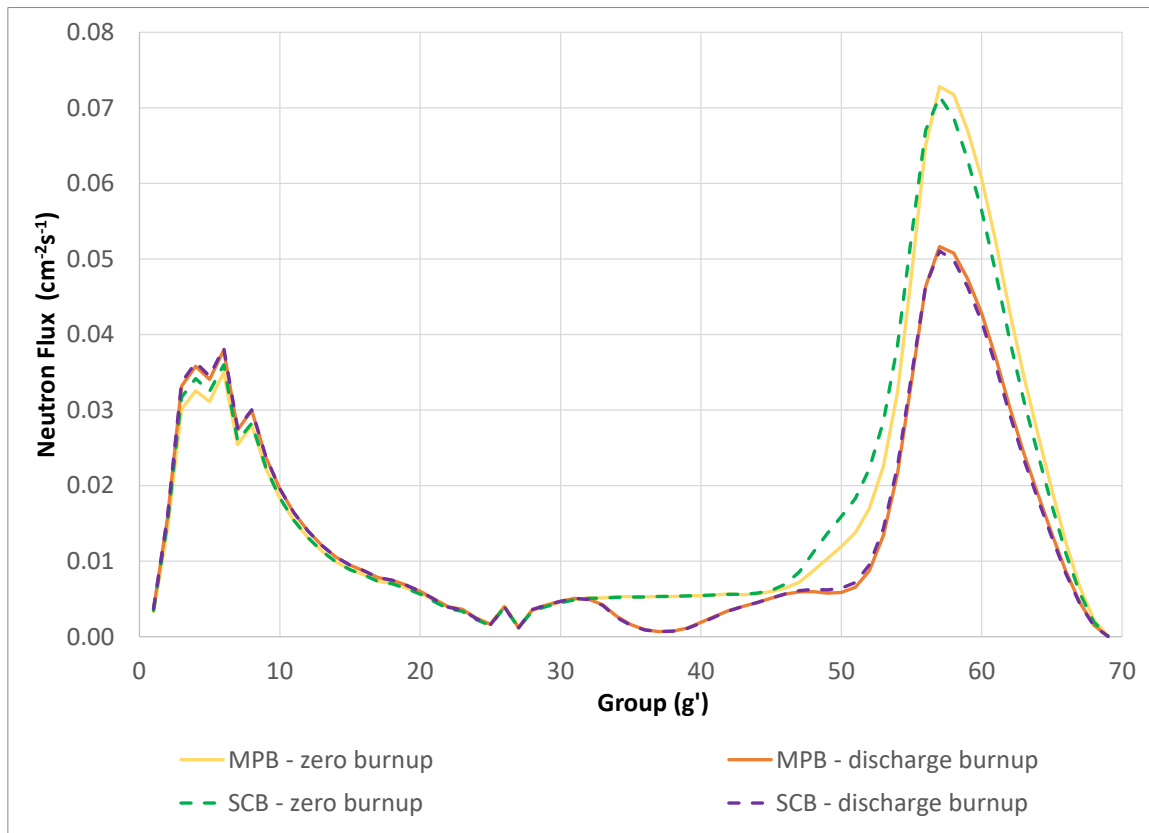
Figure 4-12: Reference SCB and MPB direct flux in the inner fuel region for zero burnup and discharge burnup
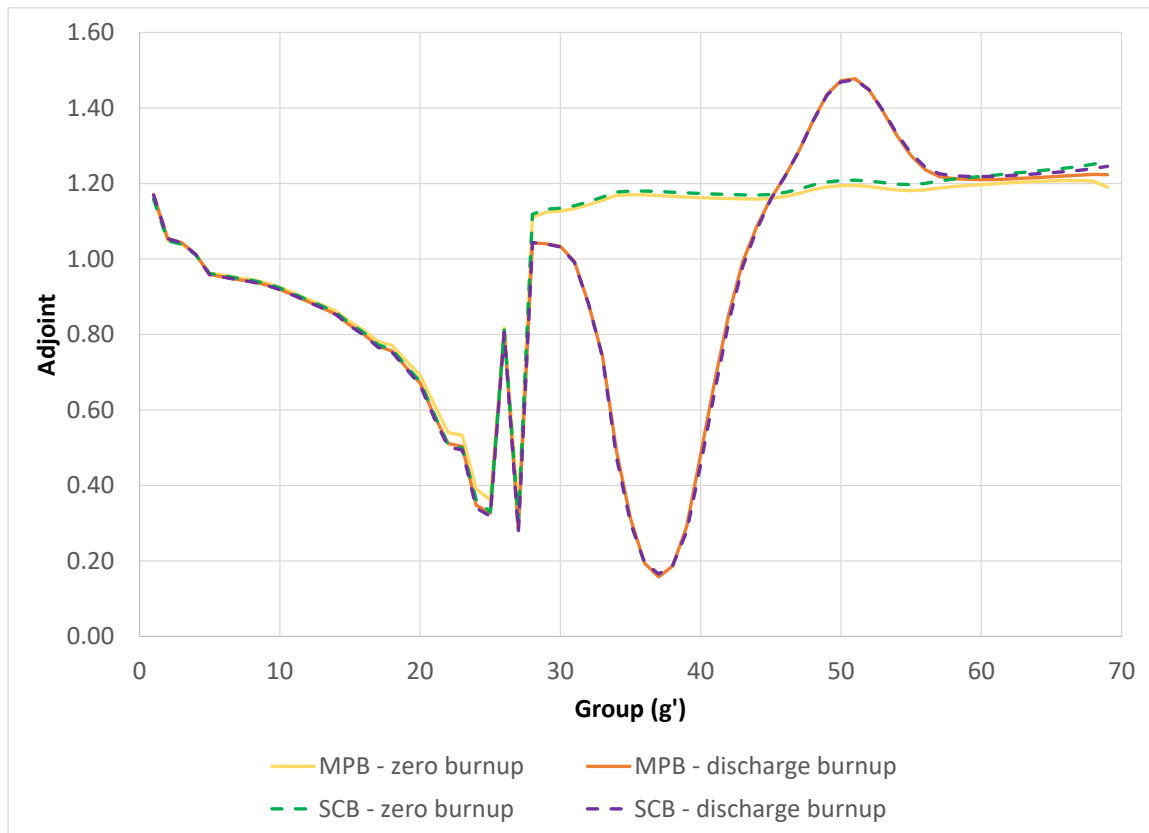
Figure 4-13: Reference SCB and MPB adjoint in the inner fuel region for zero burnup and discharge burnup
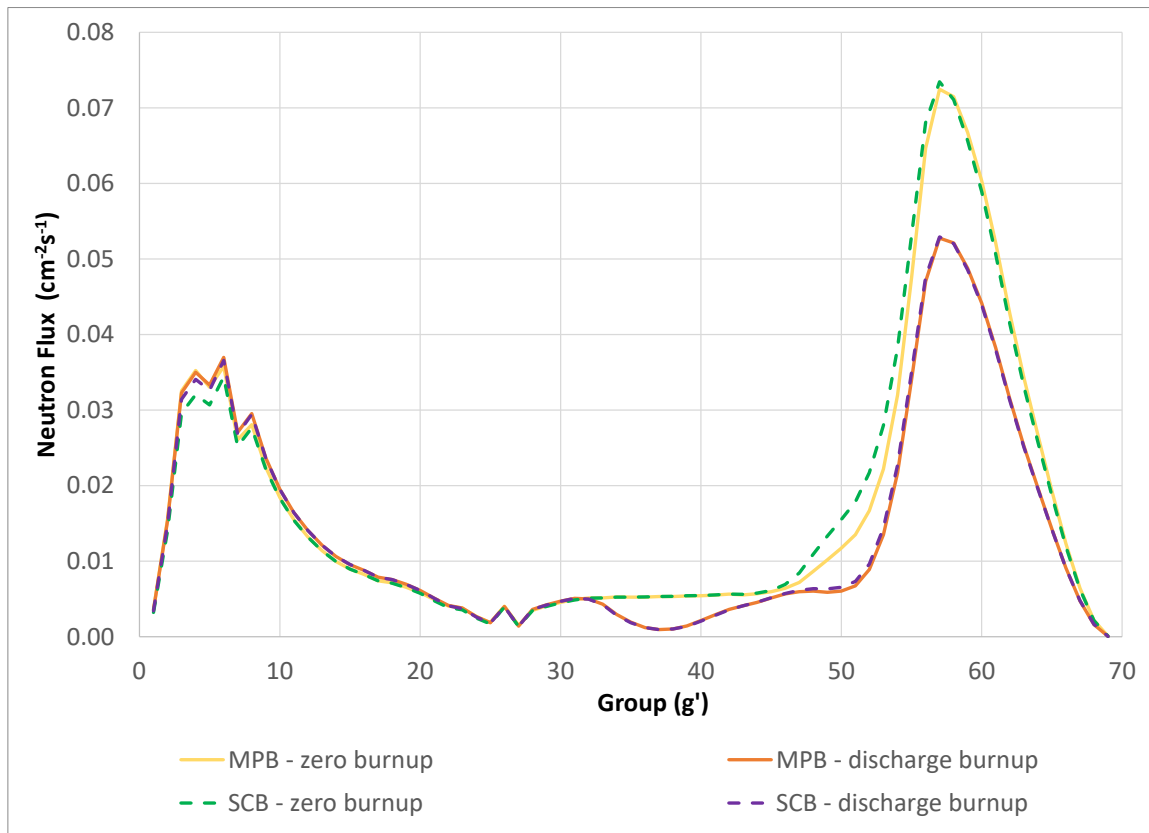
Figure 4-14: Reference SCB and MPB direct flux in the outer fuel region for zero burnup and discharge burnup
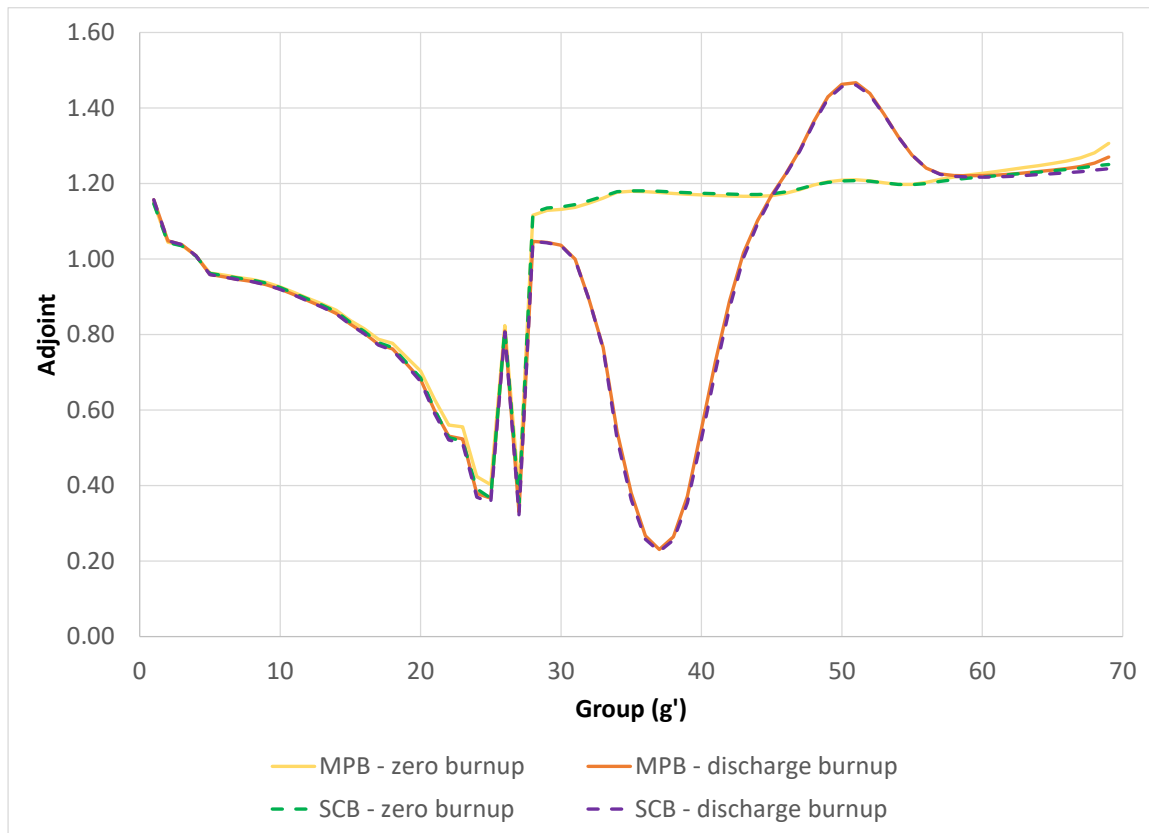
Figure 4-15: Reference SCB and MPB adjoint in the outer fuel region for zero burnup and discharge burnup
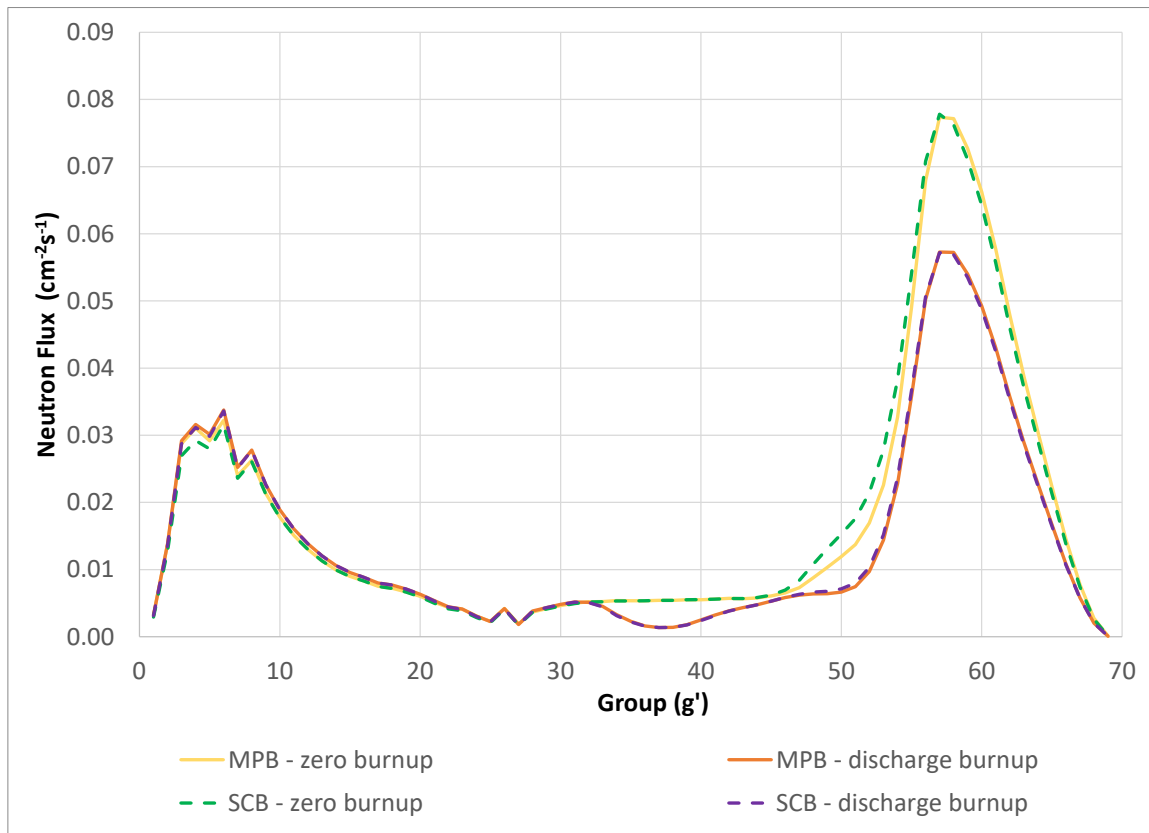
Figure 4-16: Reference SCB and MPB direct flux in the coolant for zero burnup and discharge burnup
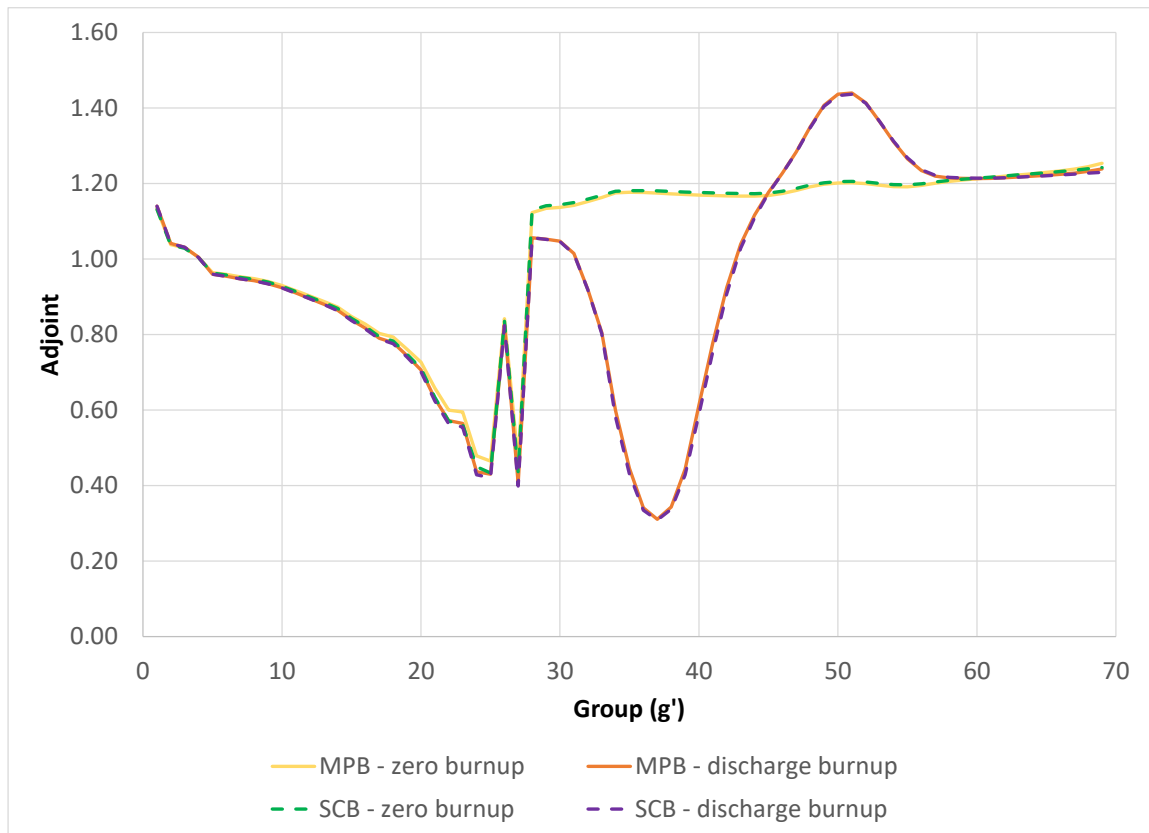
Figure 4-17: Reference SCB and MPB adjoint in the coolant for zero burnup and discharge burnup
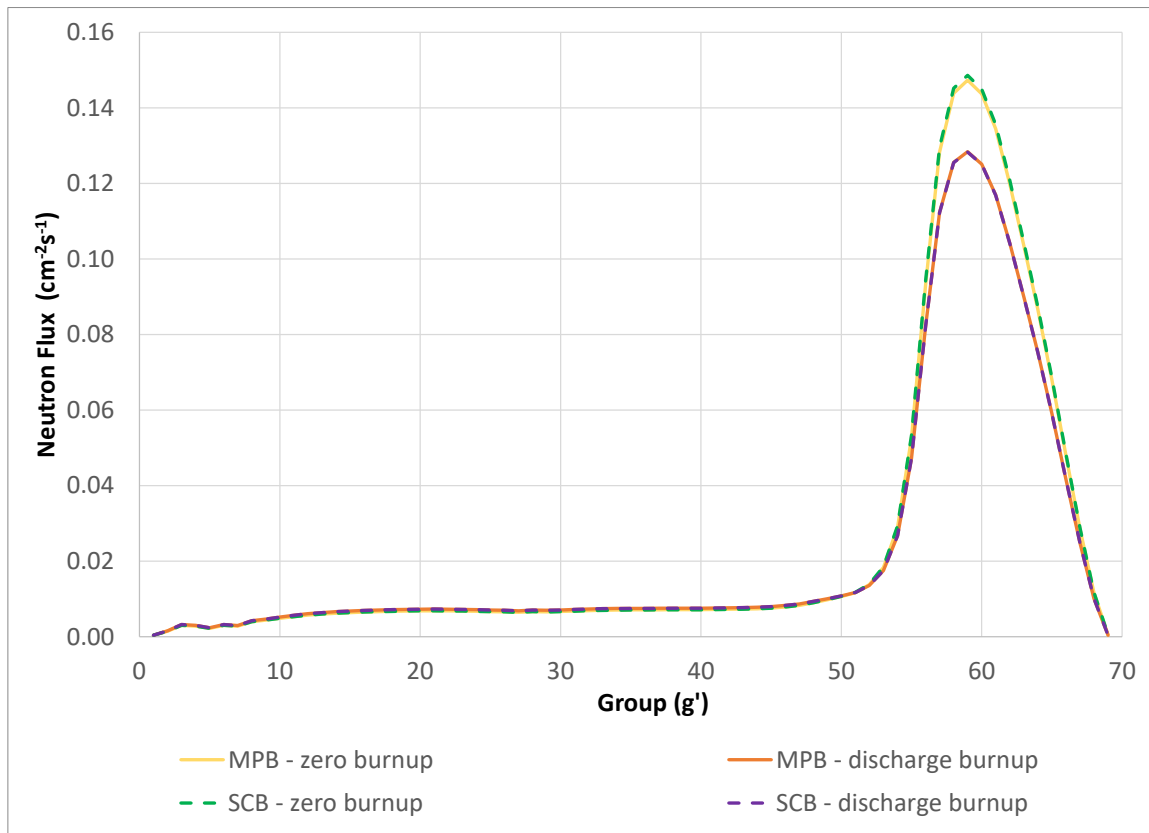
Figure 4-18: Reference SCB and MPB direct flux in the moderator for zero burnup and discharge burnup
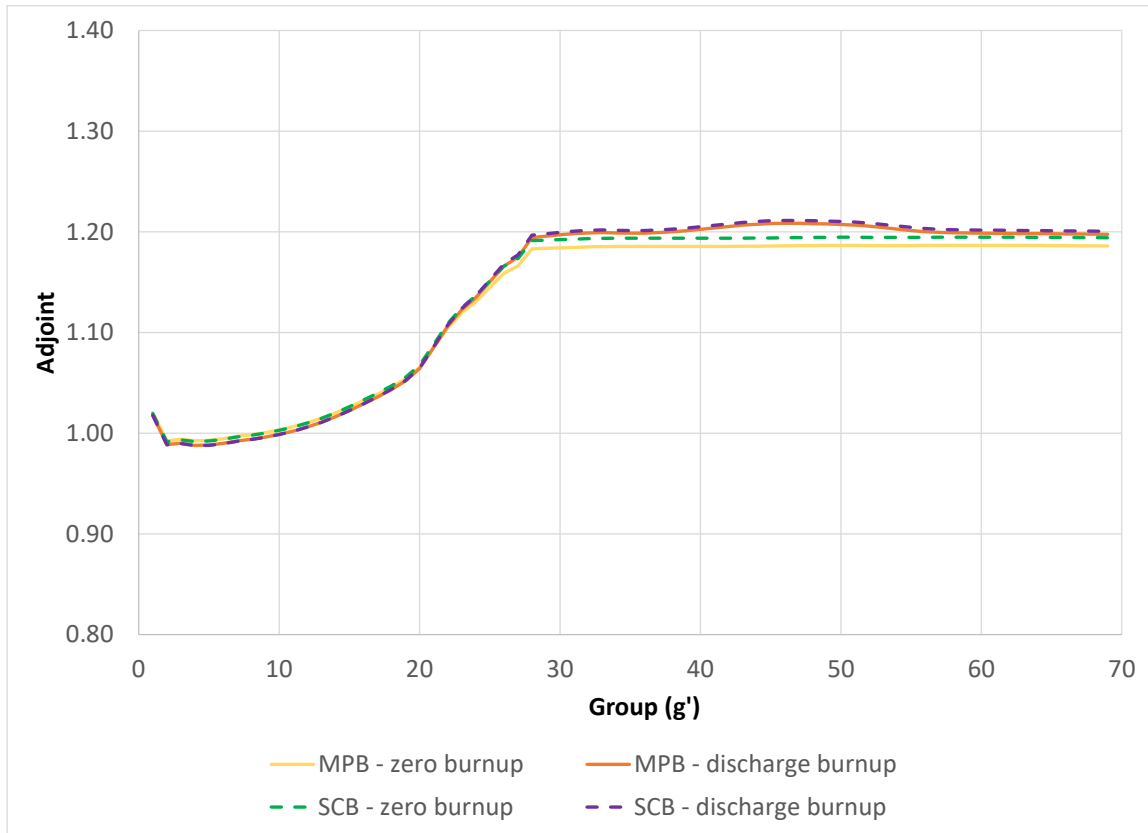
Figure 4-19: Reference SCB and MPB adjoint in the moderator for zero burnup and discharge burnup

4.4.1 Coolant-Temperature Reactivity Effect

An analysis of the coolant-temperature reactivity effect can be performed by estimating the reactivity coefficients in the vicinity of the reference point using Eq. (4.3). Considering a 50 K increase in the coolant temperature from the reference value of 583 K to 633 K, Eq. (4.3) can be used to evaluate the corresponding coolant-temperature reactivity coefficients for the zero-burnup SCB, the zero-burnup MPB, the discharge-burnup SCB, and discharge-burnup MPB. Results are shown in Table 4-2.

To understand what causes the differences in the coolant-temperature reactivity coefficient between the MPB and the SCB, as well as between discharge burnup and zero burnup, specific terms in Eq. (4.3) can be examined. First, it is observed that, because the perturbation only affects the coolant, the derivative of the production term, $\dfrac{\partial\left(\chi_g \nu\Sigma_{f,g'}\right)}{\partial T_{cool}}$, vanishes. Second, because the flux and adjoint are normalized such that the total production rate as well as the adjoint-weighted production rate (denominator in Eq. (4.3)) equal unity, Eq. (4.3) simplifies to:

$$\frac{\partial\rho}{\partial T_{cool}} \cong \sum_{g=1}^{G}\sum_{g'=1}^{G}\frac{\delta\left(\Sigma_{s,g'\to g,cool}-\delta_{g'g}\Sigma_{tg,cool}\right)}{\delta T_{cool}}\sum_{r\in cool}\Phi_{g,r}^{0*}\Phi_{g',r}^{0}V_r \qquad (4.5)$$

According to Eq. (4.5), the reactivity coefficient is just a weighed sum over all energy groups and coolant regions of cross section derivative terms $\dfrac{\delta\left(\Sigma_{s,g'\to g,cool}-\delta_{g'g}\Sigma_{tg,cool}\right)}{\delta T_{cool}}$. The weight is given by the product between the direct flux, the adjoint, and the region volume, namely $\Phi_{g,r}^{0*}\Phi_{g',r}^{0}V_r$. The cross section derivative terms $\dfrac{\delta\left(\Sigma_{s,g'\to g,cool}-\delta_{g'g}\Sigma_{tg,cool}\right)}{\delta T_{cool}}$ are the same for the SCB and the MPB and independent of burnup, while the product of the adjoint with the direct flux depends on both bundle type and burnup. It follows from Eq. (4.5) that the differences between the coolant-temperature reactivity coefficients of the MPB and those of the SCB (bottom row of Table 4-2) are due solely to the differences between the reference coolant flux and adjoint of the MPB and those of the SCB. Similarly, the differences

between the coolant-temperature reactivity coefficients at discharge burnup and those at zero burnup (right column of Table 4-2) are due solely to the differences between the reference coolant flux and adjoint at discharge burnup and those at zero burnup.

The coolant direct flux and adjoint for reference conditions are shown in Figure 4-16 and Figure 4-17, respectively, and a map of the $\dfrac{\delta\left(\Sigma_{s,g'\to g,cool}-\delta_{g'g}\Sigma_{tg,cool}\right)}{\delta T_{cool}}$ terms is shown in Figure 4-20. In Figure 4-20, diagonal terms correspond to the removal (from group g) macroscopic cross section, taken with a minus sign because of its negative contribution to reactivity. Terms above the diagonal (g'<g) represent down-scattering and terms below the diagonal (g'>g) represent up-scattering. Down- and up-scattering terms are taken with a positive sign because of their positive contribution to the reactivity.

The negative diagonal terms represent a positive derivative of (increase in) the removal macroscopic cross section, while the positive off-diagonal terms represent a positive derivative of (increase in) the group-to-group scattering macroscopic cross section. Importantly, the positive derivative of (increase in) the up-scattering cross sections in the thermal range (visible in the lower-right quadrant of Figure 4-20) is due to the higher coolant temperature which increases up-scattering due to increased thermal agitation of the coolant molecules.

As can be seen from Figure 4-20, the macroscopic cross section derivatives have different values, and even different signs, at different (g, g') combinations. Therefore,

differences (even subtle ones) in the direct flux and adjoint can induce differences in the reactivity coefficient calculated according to Eq. (4.5) and even a change in its sign.

Table 4-2 shows that, at zero burnup, the magnitude of the coolant-temperature reactivity coefficient of the MPB is 24% larger than that of the SCB, while at discharge burnup, the magnitude of the MPB coolant-temperature reactivity coefficient is almost equal, but slightly smaller (-1.7%) than that of the SCB. Such modest differences stem from the relatively minor differences between the reference coolant flux and adjoint of the MPB and those of the SCB, as illustrated in Figure 4-16 and Figure 4-17

Table 4-2 also shows that while the coolant-temperature reactivity coefficients for the zero-burnup SCB and MPB are negative, those coefficients become positive at discharge burnup for both bundle types and their absolute values are two to three times larger at discharge burnup than at zero burnup. Such large swings in the coolant-temperature reactivity coefficients between zero burnup and discharge-burnup are explained by the substantial differences between the reference coolant flux and adjoint at zero burnup and those at discharge burnup, as can be seen in Figure 4-16 and Figure 4-17.

The coolant-temperature reactivity coefficients predicted by perturbation theory and summarized in Table 4-2 are consistent with the slopes of the coolant-temperature reactivity effect plots shown in Figure 4-4. Figure 4-4 also shows that, for large perturbations, the coolant-temperature reactivity effect becomes slightly non-linear.

Table 4-2: Coolant-temperature Reactivity Coefficients (mk/K)

	Zero burnup	Discharge burnup	% Difference
SCB	-8.18E-06	+2.42E-05	-396%
MPB	-1.01E-05	+2.38E-05	-335%
% Difference	23.9%	-1.7%	
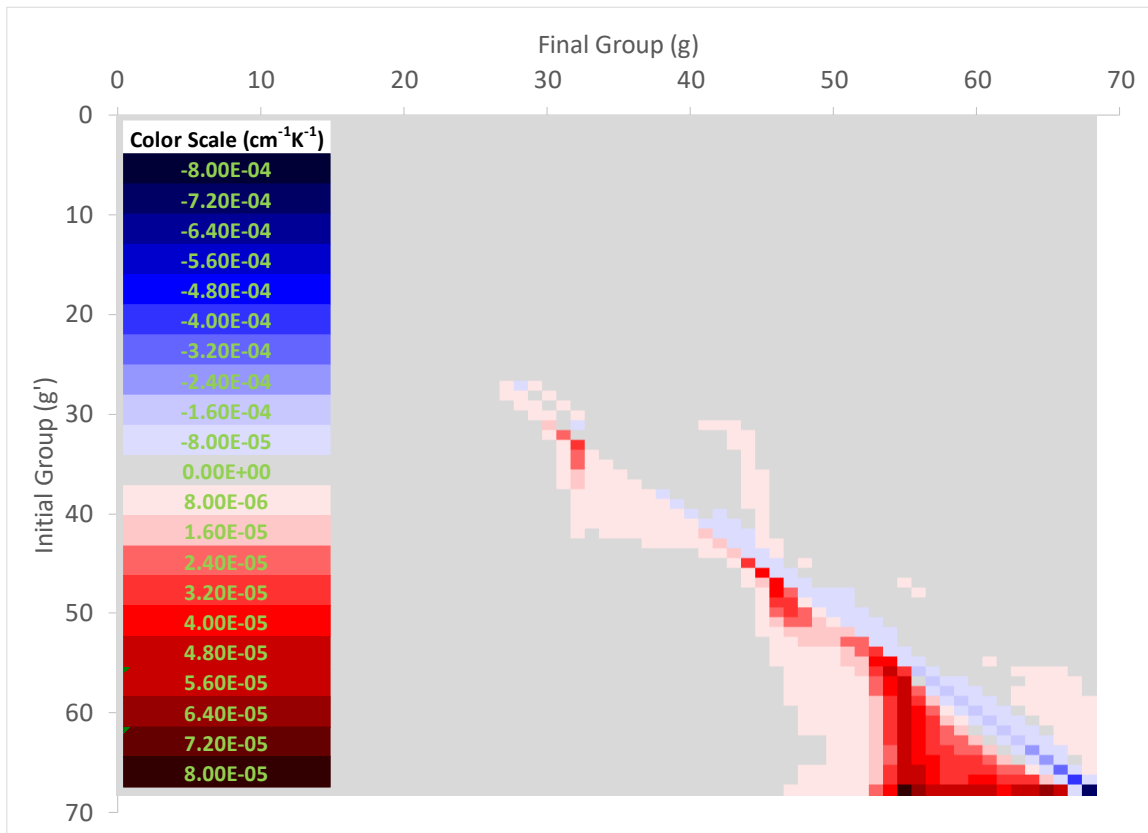
Figure 4-20: Map of the $\dfrac{\delta\left(\Sigma_{s,g'\to g,cool} - \delta_{g'g}\Sigma_{tg,cool}\right)}{\delta T_{cool}}$ *terms*

4.4.2 Moderator-Temperature Reactivity Effect

An analysis of the moderator-temperature reactivity effect can be performed by estimating the reactivity coefficients in the vicinity of the reference point using Eq. (4.3). Considering a 50 K increase in the moderator temperature from the reference value of 346 K to 396 K, Eq. (4.3) can be used to evaluate the corresponding moderator-temperature reactivity coefficients for the zero-burnup SCB, the zero-burnup MPB, the discharge-burnup SCB, and discharge-burnup MPB. Results are shown in Table 4-3.

To understand what causes the differences in the coolant-temperature reactivity coefficient between the MPB and the SCB, as well as between zero burnup and discharge burnup, specific terms in Eq. (4.3) can be examined. Because the perturbation only affects the moderator, the same arguments that applied to the coolant apply here, and a formula similar to Eq. (4.5) can be used:

$$\frac{\partial \rho}{\partial T_{\text{mod}}} \cong \sum_{g=1}^{G} \sum_{g'=1}^{G} \frac{\delta\left(\Sigma_{s,g'\to g,\text{mod}} - \delta_{g'g}\Sigma_{tg,\text{mod}}\right)}{\delta T_{\text{mod}}} \sum_{r\in mod} \Phi_{g,r}^{0*}\Phi_{g',r}^{0}V_r \tag{4.6}$$

Similar to the case of the coolant, the reactivity coefficient is just a weighed sum over all energy groups and moderator regions of cross section derivative terms $\frac{\delta\left(\Sigma_{s,g'\to g,\text{mod}} - \delta_{g'g}\Sigma_{tg,\text{mod}}\right)}{\delta T_{\text{mod}}}$ with the weight given by the product between the direct flux, the adjoint, and the region volume, namely $\Phi_{g,r}^{0*}\Phi_{g',r}^{0}V_r$. Just as for the coolant,

the cross section derivative terms $\dfrac{\delta\left(\Sigma_{s,g'\to g,\mathrm{mod}}-\delta_{g'g}\Sigma_{tg,\mathrm{mod}}\right)}{\delta T_{\mathrm{mod}}}$ are the same for the SCB

and the MPB and independent of burnup, while the product of the adjoint with the

direct flux depends on both bundle type and burnup. It follows from Eq. (4.6) that the

differences between the moderator-temperature reactivity coefficients of the MPB

and those of the SCB (bottom row of Table 4-3) are due solely to the differences

between the reference coolant flux and adjoint of the MPB and those of the SCB.

Similarly, the differences between the moderator-temperature reactivity coefficients

at discharge-burnup and those at zero-burnup (right column of Table 4-3) are due

solely to the differences between the reference moderator flux and adjoint at

discharge burnup and those at zero burnup.

The moderator direct flux and adjoint for reference conditions are shown in

Figure 4-18 and Figure 4-19, respectively, and a map of the $\dfrac{\delta\left(\Sigma_{s,g'\to g,\mathrm{mod}}-\delta_{g'g}\Sigma_{tg,\mathrm{mod}}\right)}{\delta T_{\mathrm{mod}}}$

terms is shown in Figure 4-21. Similar to the case of the coolant, the positive

derivative of (increase in) the up-scattering cross sections in the thermal range

(visible in the lower-right quadrant of Figure 4-21) is due to a higher moderator

temperature which increases up-scattering due to increased thermal agitation of the

heavy-water molecules.

Just like for the coolant, and as can be seen from Figure 4-21, the macroscopic

cross section derivatives have different values, and even different signs, at different

(g, g') combinations. Because of that, differences (even subtle ones) in the direct flux

and adjoint can induce differences in the reactivity coefficient calculated according to Eq. (4.6) and even a change in its sign.

Table 4-3 shows that, at zero burnup, the magnitude of the moderator-temperature reactivity coefficient of the MPB is 8.9% larger than that of the SCB, while at discharge burnup, the magnitude of the MPB moderator-temperature reactivity coefficient is almost equal, but slightly smaller (-1.7%) than that of the SCB. Such modest differences stem from the relatively minor differences between the reference moderator flux and adjoint of the MPB and those of the SCB, as illustrated in Figure 4-18 and Figure 4-19.

Table 4-3 also shows that while the moderator-temperature reactivity coefficients for the zero-burnup SCB and MPB are negative, those coefficients become positive at discharge burnup for both bundle types and their absolute values are six to seven times larger at discharge burnup than at zero burnup. Such large swings in the moderator-temperature reactivity coefficients between zero burnup and discharge-burnup are explained by the substantial differences between the reference moderator flux and adjoint at zero burnup and those at discharge burnup, as can be seen in Figure 4-18 and Figure 4-19.

Table 4-3: Moderator-temperature Reactivity Coefficients (mk/K)

	Zero burnup	Discharge burnup	% Difference
SCB	-1.92E-05	1.31E-04	-780%
MPB	-2.10E-05	1.29E-04	-714%
% Difference	8.9%	-1.7%	
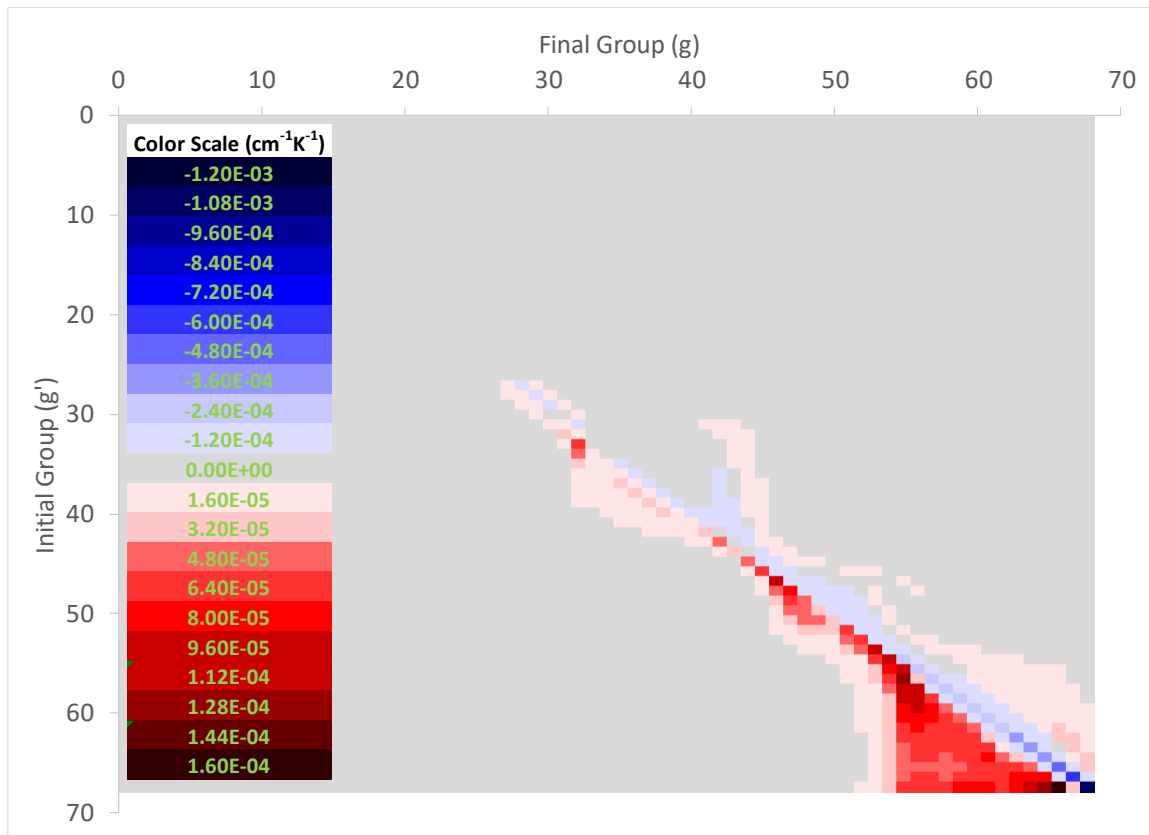
Figure 4-21: Map of the $\dfrac{\delta\left(\Sigma_{s,g'\to g,\text{mod}} - \delta_{g'g}\Sigma_{tg,\text{mod}}\right)}{\delta T_{\text{mod}}}$ *terms*

The moderator-temperature reactivity coefficients predicted by perturbation theory and summarized in Table 4-3 are consistent with the slopes of the moderator-temperature reactivity effect plots shown in Figure 4-5.

4.4.3 Coolant-Density Reactivity Effect

An analysis of the coolant-density reactivity effect can be performed by estimating the reactivity coefficients in the vicinity of the reference point using Eq. (4.3). Considering a decrease in the coolant density, D_{cool}, from the initial value of 0.76 g/cm³ to 0.61 g/cm³, Eq. (4.3) can be used to evaluate the corresponding

coolant-density reactivity coefficient for the zero-burnup SCB, the zero-burnup MPB, the discharge-burnup SCB, and discharge-burnup MPB. Results are shown in Table 4-4.

To understand what causes the differences in the coolant-density reactivity coefficient between the MPB and the SCB, as well as between zero burnup and discharge burnup, specific terms in Eq. (4.3) can be examined, just as it was done in Section 4.4.1 for the coolant-temperature coefficient. Because the perturbation only affects the coolant, the same arguments that were made in Section 4.4.1 apply here, and a formula similar to Eq. (4.5) can be used:

$$\frac{\partial \rho}{\partial D_{cool}} \cong \sum_{g=1}^{G} \sum_{g'=1}^{G} \frac{\delta\left(\Sigma_{s,g'\rightarrow g,cool} - \delta_{g'g}\Sigma_{tg,cool}\right)}{\delta D_{cool}} \sum_{r \in cool} \Phi_{g,r}^{0*} \Phi_{g',r}^{0} V_{r} \qquad (4.7)$$

Because the cross section derivative terms $\dfrac{\delta\left(\Sigma_{s,g'\rightarrow g,cool} - \delta_{g'g}\Sigma_{tg,cool}\right)}{\delta D_{cool}}$ are the same for the SCB and the MPB and independent of burnup, while the product of the adjoint with the direct flux depends on both bundle type and burnup, the differences between the coolant-density reactivity coefficients of the MPB and those of the SCB (bottom row of Table 4-4) are due solely to the differences between the reference coolant flux and adjoint of the MPB and those of the SCB. Similarly, the differences between the coolant-density reactivity coefficients at discharge-burnup and those at zero-burnup (right column of Table 4-4) are due solely to the differences between the reference coolant flux and adjoint at discharge burnup and those at zero burnup.

The coolant direct flux and adjoint for reference conditions are shown in Figure

4-16 and Figure 4-17, respectively, and a map of the $\dfrac{\delta\left(\Sigma_{s,g'\rightarrow g,cool} - \delta_{g'g}\Sigma_{tg,cool}\right)}{\delta D_{cool}}$ terms

is shown in Figure 4-22.

As can be seen from Figure 4-22, the macroscopic cross section derivatives have different values, and even different signs, at different (g, g') combinations. Consequently, differences (even subtle ones) in the direct flux and adjoint can induce differences in the reactivity coefficient calculated according to Eq. (4.7).

Table 4-4 shows that, at zero burnup, the magnitude of the coolant-density reactivity coefficient of the MPB is 1.4% smaller than that of the SCB, while at discharge burnup, the magnitude of the MPB coolant-density-reactivity coefficient is 2.4% smaller than that of the SCB. Such differences stem from the differences between the reference coolant flux and adjoint of the MPB and those of the SCB, as illustrated in Figure 4-16 and Figure 4-17.

Table 4-4 also shows that the coolant-density reactivity coefficients are negative for both bundle types at both zero burnup and discharge burnup and relatively close to each other. The absolute values of the reactivity coefficients are ~10% lower at discharge burnup than at zero burnup for both bundle types, and these differences are the consequence of differences between the reference coolant flux and adjoint at discharge burnup and those at zero burnup, as illustrated in Figure 4-16 and Figure 4-17.

Overall, the coolant-density reactivity coefficient shows a larger change when going from zero burnup to discharge burnup than when going from SCB to MPB. This is consistent with the fact that the reference flux and adjoint in the coolant change more when going from zero burnup to discharge burnup than when going from SCB to MPB (Figure 4-16 and Figure 4-17).

The coolant-density reactivity coefficients predicted by perturbation theory and summarized in Table 4-4 are consistent with the slopes of the coolant-density reactivity effect plots shown in Figure 4-6. Figure 4-6 also shows that the coolant-density reactivity effect is linear over a wide range of densities, a behavior consistent with the fact that the macroscopic cross section perturbations are linear in the atom density, and hence in the coolant density. It is important to stress that the coolant-density reactivity coefficients are determined by the same reference direct flux and adjoint that determine the coolant-temperature reactivity coefficients. However, unlike the coolant-temperature reactivity coefficients, they do not change sign with burnup. The different behaviour stems from the different cross section derivatives, illustrated by the differences between Figure 4-22 and Figure 4-20; in particular the fact that when density is changed, all macroscopic cross sections change by the same fractional amount, whereas when temperature is changed, cross sections change by different fractional amounts at different energies.

Table 4-4: Coolant-density Reactivity Coefficients (mk·g⁻¹·cm³)

	Zero burnup	Discharge burnup	% Difference
SCB	-2.40E-02	-2.15E-02	-10.5%
MPB	-2.37E-02	-2.10E-02	-11.3%
% Difference	-1.4%	-2.4%	
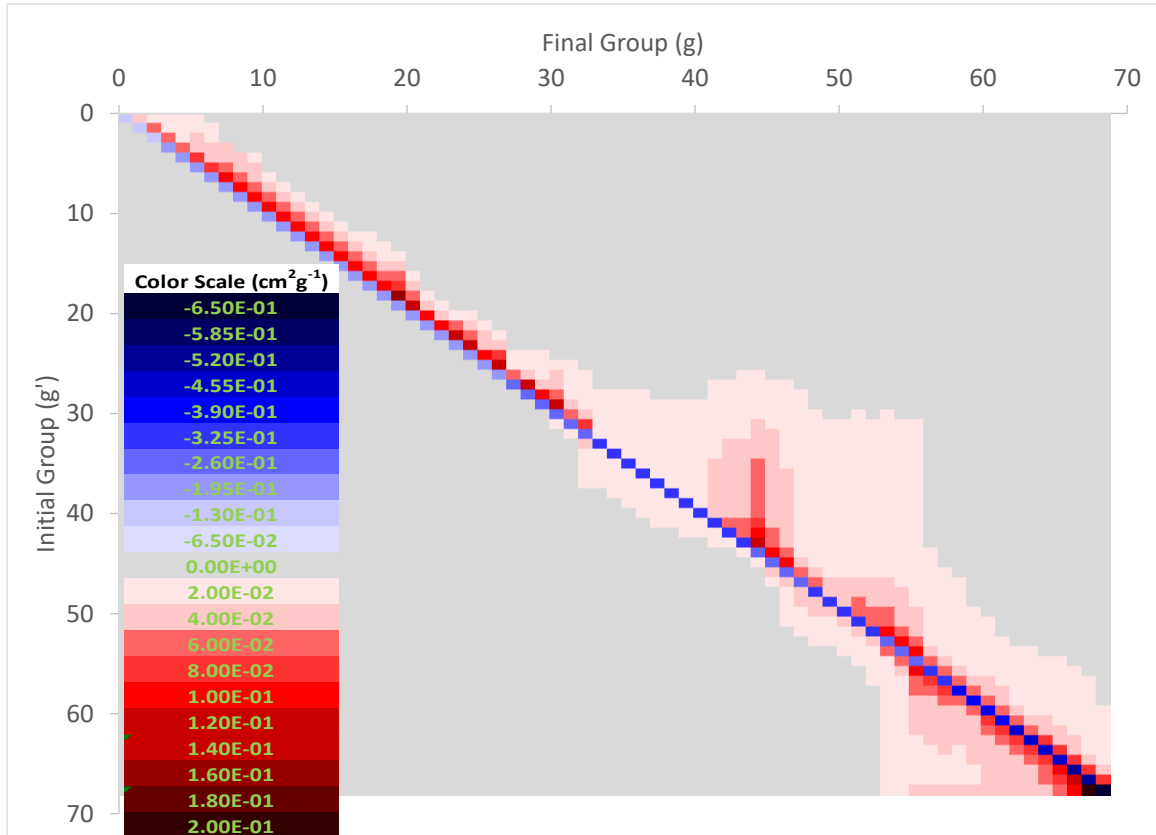
Figure 4-22: Map of the $\dfrac{\delta\left(\Sigma_{s,g'\to g,cool} - \delta_{g'g}\Sigma_{tg,cool}\right)}{\delta D_{cool}}$ *terms*

4.4.4 Moderator-Density Reactivity Effect

An analysis of the moderator-density reactivity effect can be performed by estimating the reactivity coefficients in the vicinity of the reference point using Eq. (4.3). Considering a 0.108 g/cm³ decrease in the moderator density from the reference value of 1.083 g/cm³ to 0.975 g/cm³, Eq. (4.3) can be used to evaluate the corresponding moderator-density reactivity coefficient for the zero-burnup SCB, the zero-burnup MPB, the discharge-burnup SCB, and discharge-burnup MPB. Results are shown in Table 4-5.

To understand what causes the differences in the moderator-density reactivity coefficient between the MPB and the SCB, as well as between zero burnup and discharge burnup, specific terms in Eq. (4.3) can be examined, just as it was done in Section 4.4.3 for the coolant-density coefficient. Because the perturbation only affects the moderator, the same arguments that were made in Section 4.4.3 apply here, and a formula similar to Eq. (4.6) can be used:

$$\frac{\partial \rho}{\partial D_{\text{mod}}} \cong \sum_{g=1}^{G} \sum_{g'=1}^{G} \frac{\delta\left(\Sigma_{s,g'\to g,\text{mod}} - \delta_{g'g}\Sigma_{tg,\text{mod}}\right)}{\delta D_{\text{mod}}} \sum_{r\in mod} \Phi_{g,r}^{0*}\Phi_{g',r}^{0}V_r \tag{4.8}$$

Because the cross section derivative terms $\dfrac{\delta\left(\Sigma_{s,g'\to g,\text{mod}} - \delta_{g'g}\Sigma_{tg,\text{mod}}\right)}{\delta D_{\text{mod}}}$ are the same for the SCB and the MPB and independent of burnup, while the product of the adjoint with the direct flux depends on both bundle type and burnup, the differences between the moderator-density reactivity coefficients of the MPB and those of the SCB (bottom row of Table 4-5) are due solely to the differences between the reference

moderator flux and adjoint of the MPB and those of the SCB. Similarly, the differences

between the moderator-density reactivity coefficients at discharge-burnup and those

at zero-burnup (right column of Table 4-5) are due solely to the differences between

the reference moderator flux and adjoint at discharge burnup and those at zero

burnup.

The moderator direct flux and adjoint for reference conditions are shown in

Figure 4-18 and Figure 4-19, respectively, and a map of the $\dfrac{\delta\left(\Sigma_{s,g'\to g,\text{mod}} - \delta_{g'g}\Sigma_{tg,\text{mod}}\right)}{\delta D_{\text{mod}}}$

terms is shown in Figure 4-23.

As can be seen from Figure 4-23, the macroscopic cross section derivatives have

different values, and even different signs, at different (g, g') combinations.

Consequently, differences (even subtle ones) in the direct flux and adjoint can induce

differences in the reactivity coefficient calculated according to Eq. (4.8).

Table 4-5 shows that, at zero burnup, the magnitude of the moderator-density

reactivity coefficient of the MPB is 4.1% smaller than that of the SCB, while at

discharge burnup, the magnitude of the MPB moderator-density-reactivity coefficient

is 1.5% smaller than that of the SCB. Such differences stem from the differences

between the reference moderator flux and adjoint of the MPB and those of the SCB, as

illustrated in Figure 4-18 and Figure 4-19.

Table 4-5 also shows that the moderator-density reactivity coefficients are

positive for both bundle types at both zero burnup and discharge burnup and

relatively close to each other. The absolute values of the SCB reactivity coefficients

are 12.9% larger at discharge burnup than at zero burnup and the MPB reactivity coefficients are 16.0% larger at discharge burnup than at zero burnup. These differences are the consequence of differences between the reference moderator flux and adjoint at discharge burnup and those at zero burnup, as illustrated in Figure 4-18 and Figure 4-19.

Overall, the moderator-density reactivity coefficient shows a larger change when going from zero burnup to discharge burnup than when going from SCB to MPB. This is consistent with the fact that the reference flux and adjoint in the moderator change more when going from zero burnup to discharge burnup than when going from SCB to MPB (Figure 4-18 and Figure 4-19).

The moderator-density reactivity coefficients predicted by perturbation theory and summarized in Table 4-5 are consistent with the slopes of the moderator-density reactivity effect plots shown in Figure 4-7. Figure 4-7 also shows that the effect becomes non-linear as the moderator density drops below 0.9 g/cm^3. This is explained by the fact that the linear perturbation formula does not apply for large perturbations. So, even if the macroscopic cross section perturbations are linear in the atom density, and hence in the moderator density, because the moderator represents such a large fraction of the cell volume, perturbing its density can lead to large reactivity effects, which cease to be linear. It is important to stress that the moderator-density reactivity coefficients are determined by the same reference direct flux and adjoint that determine the moderator-temperature reactivity coefficients. However, unlike the moderator-temperature reactivity coefficients, they

do not change sign with burnup. The different behaviour stems from the different

cross section derivatives, illustrated by the differences between Figure 4-23 and

Figure 4-21; in particular the fact that when density is changed, macroscopic cross

sections at all energies change by the same fractional amount, whereas when

temperature is changed, cross sections change by different fractional amounts at

different energies. It is also important to note that both the moderator-density

reactivity coefficients and the coolant-density reactivity coefficients are determined

by the cross-section derivatives (with respect to density) of heavy water (albeit at

different reference temperatures, namely the moderator and coolant temperature).

The main reasons why the moderator-density reactivity coefficients are very

different from the coolant-density reactivity coefficients (including having a different

sign) are (i) the differences between the moderator flux and adjoint and the coolant

flux and adjoint illustrated by Figure 4-16 to Figure 4-19, in particular the absence of

any high-energy flux peak in the moderator, and (ii) the much larger volume of the

moderator.

Table 4-5: Moderator-density Reactivity Coefficients (mk·g^{-1}·cm^3)

	Zero burnup	Discharge burnup	% Difference
SCB	+0.132	+0.149	12.9%
MPB	+0.127	+0.147	16.0%
% Difference	-4.1%	-1.5%	
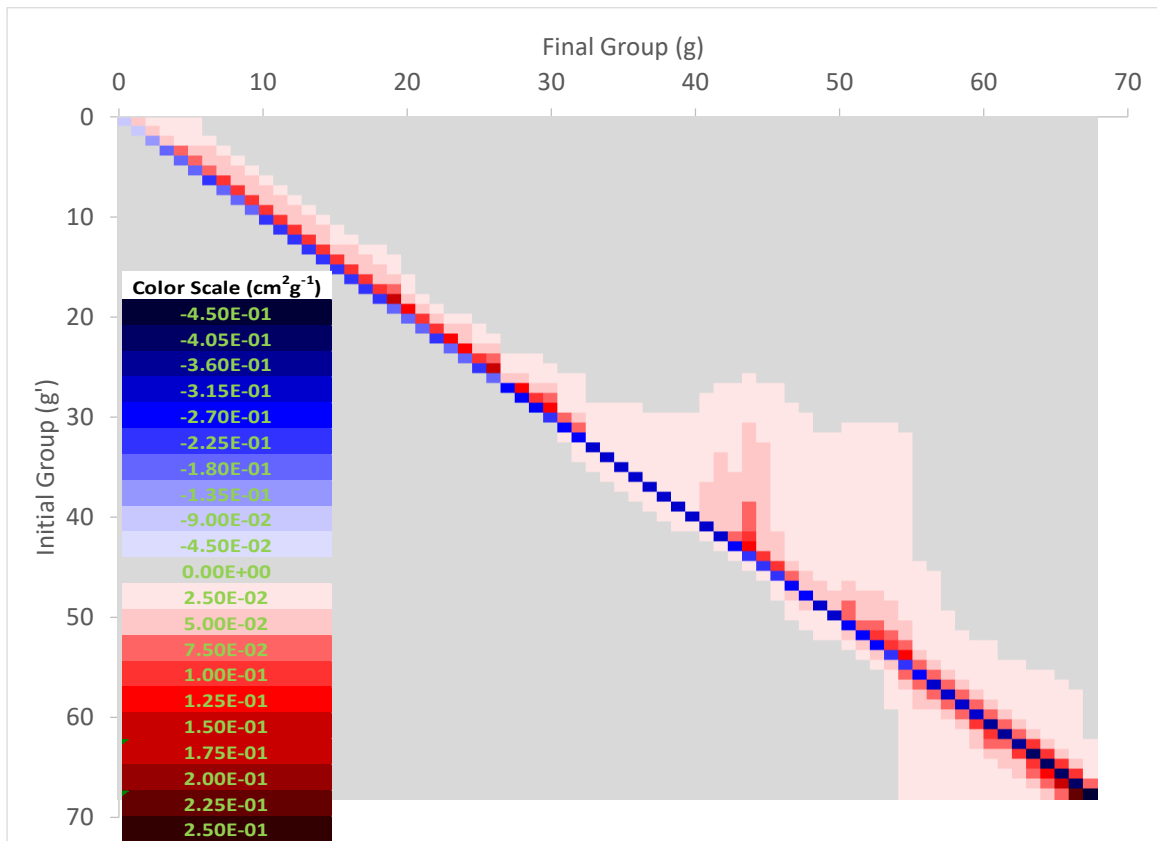
Figure 4-23: Map of the $\dfrac{\delta\left(\Sigma_{s,g'\to g,\text{mod}} - \delta_{g'g}\Sigma_{tg,\text{mod}}\right)}{\delta D_{\text{mod}}}$ *terms*

4.4.5 Fuel-Temperature Reactivity Effect

An analysis of the fuel-temperature reactivity effect can be performed by estimating the reactivity coefficients in the vicinity of the reference point using Eq. (4.3). Considering a 69 K increase in the outer fuel temperature, $T_{outer\text{-}fuel}$, from the reference value of 681 K to 750 K, Eq. (4.3) is used to evaluate the corresponding fuel-temperature reactivity coefficient for the zero-burnup SCB, the zero-burnup

MPB, the discharge-burnup SCB, and discharge-burnup MPB. Results are shown in Table 4-6.

To understand what causes the differences in the fuel-temperature reactivity coefficient between the MPB and the SCB, as well as between zero burnup and discharge burnup, Eq. (4.3) can be used. Because the perturbation affects the fuel, no terms in that equation vanish. Nonetheless, because the flux and adjoint are normalized such that the total production rate as well as the adjoint-weighted production rate (denominator in Eq. (4.3)) equal unity, Eq. (4.3) can still be partially simplified, to:

$$
\frac{\partial \rho}{\partial T_{outer-fuel}} \cong \sum_{g=1}^{G} \sum_{g'=1}^{G} \sum_{r \in fuel} \Phi_{g,r}^{0*} \Phi_{g',r}^{0} V_r \left[\frac{1}{k_{eff}^0} \frac{\delta\left(\chi_g \nu \Sigma_{fg',r}\right)}{\delta T_{outer-fuel}} + \frac{\delta\left(\Sigma_{s,g'\to g,r} - \delta_{g'g} \Sigma_{tg,r}\right)}{\delta T_{outer-fuel}} \right]
$$

$$(4.9)$$

The derivative terms $\dfrac{\delta\left(\chi_g \nu \Sigma_{fg',r}\right)}{\delta T_{outer-fuel}}$ and $\dfrac{\delta\left(\Sigma_{s,g'\to g,r} - \delta_{g'g} \Sigma_{tg,r}\right)}{\delta T_{outer-fuel}}$ will be different for the SCB and the MPB, will depend on burnup, and will be different in the inner and outer fuel regions. The derivative terms are different in each fuel region because, on one hand, the fuel composition in the MPB and SCB is different in different fuel regions and, on the other hand, because the temperature increase in each fuel region is different even if the outer fuel temperature increase is the same. Representative plots of the derivative of the production cross section, $\dfrac{\delta \nu \Sigma_{fg',r}}{\delta T_{outer-fuel}}$, in the inner and outer fuel regions are shown in Figure 4-24 and Figure 4-25, respectively.

The differences between the production derivative terms for the inner and outer fuel region of the SCB are caused, primarily, by the fact that the fuel temperature perturbation in the inner region of the fuel is larger than the fuel-temperature perturbation in the outer region of the fuel. The former is larger because of the radial fuel temperature profile which shows higher temperatures closer to the centerline and hence larger temperature variations in the inner fuel region compared to outer fuel region. The differences between the production derivative terms of the MPB and those of the SCB are due to differences in the fuel composition (the MPB uses depleted fuel in the inner region and enriched fuel in the outer region, while the SCB uses natural uranium in both regions). Finally, the differences between the production derivative terms at discharge burnup and those at zero burnup (for both bundle types and for both fuel regions) are due to the depletion of ^{235}U and buildup of ^{239}Pu. Both the depletion of ^{235}U and the buildup of ^{239}Pu are different for the MPB and the SCB because of their different initial fuel compositions.

The derivative terms $\dfrac{\delta\left(\Sigma_{s,g'\rightarrow g,r} - \delta_{g'g}\Sigma_{tg,r}\right)}{\delta T_{outer-fuel}}$ depend on the fuel region (inner or outer), bundle type (MPB or SCB) and burnup level (zero burnup or discharge burnup), for a total of eight different instances. For brevity, maps of these derivative terms are not included. It will only be noted that the derivative-term maps for the fuel temperature have the same general structure as those for the coolant or moderator temperature but, of course, the specific group-dependent values are different. The reason for the values being different is that in the case of the fuel, changes in macroscopic cross sections (especially the diagonal terms) are due primarily to the

Doppler widening of resonances, whereas the coolant and moderator cross sections have no resonances and hence changes induced by temperature variations are mostly due to the shift in the thermal neutron spectrum.

The overall reactivity effect of perturbing the (outer) fuel temperature is the result of the combined effect of changes in the removal cross section, the scattering cross section and the production cross section, weighted by the product of the direct flux and adjoint.

Table 4-6 shows that the fuel-temperature reactivity coefficients are always negative, for both the MPB and SCB, and both at zero burnup and discharge burnup. The absolute values of the reactivity coefficients are larger at discharge burnup by ~80% for both bundle types. At zero burnup, the magnitude of the reactivity coefficient of the MPB is 13.6% smaller than that of the SCB while, at discharge burnup, the magnitude of the MPB reactivity coefficient is 15.8% larger than that of the SCB.

Overall, the fuel-temperature reactivity coefficients show a larger change when going from zero burnup to discharge burnup than when going from SCB to MPB. This is consistent with the fact that the reference flux and adjoint in the fuel change more when going from zero burnup to discharge burnup than when going from SCB to MPB (Figure 4-12 to Figure 4-15).

Table 4-6: Fuel-temperature Reactivity Coefficients (mk/K)

	Zero burnup	Discharge burnup	% Difference
SCB	-2.69E-05	-3.83E-06	-85.8%
MPB	-2.32E-05	-4.43E-06	-80.9%
% Difference	-13.6%	15.8%	
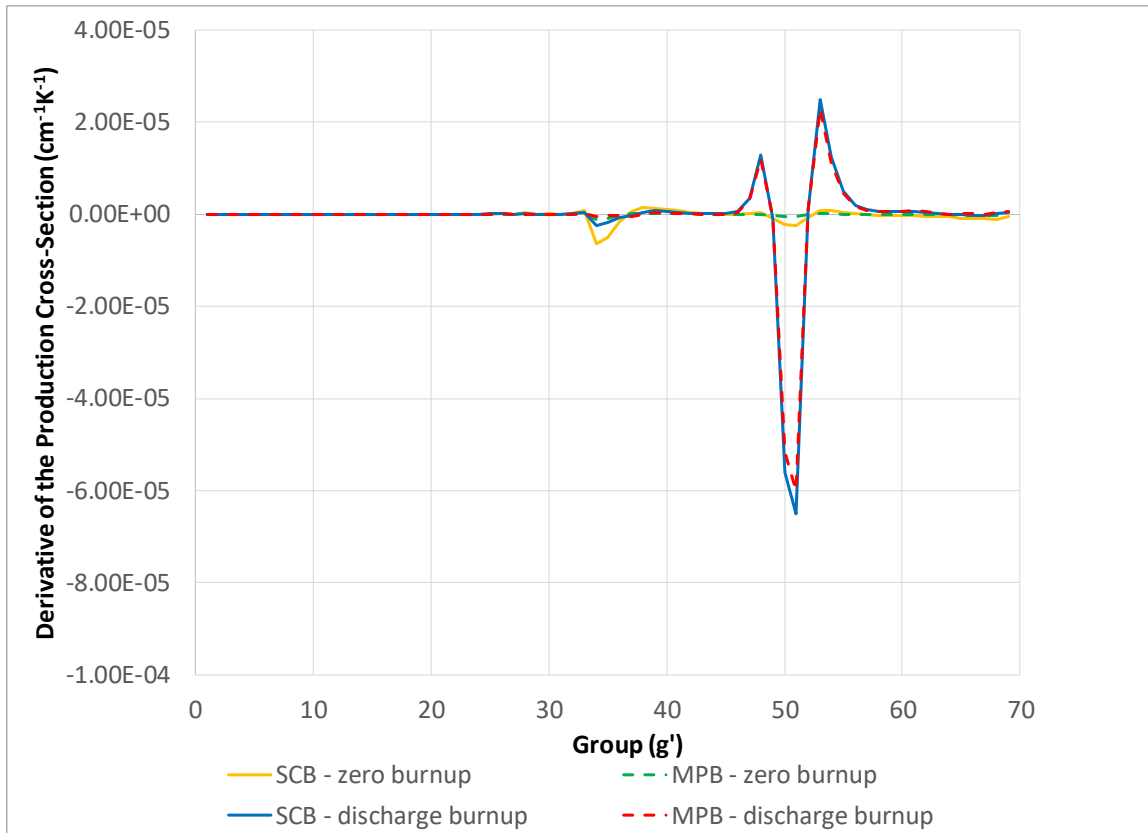
Figure 4-24: Plot of the $\dfrac{\delta\nu\Sigma_{fg',r}}{\delta T_{outer-fuel}}$ term in the inner fuel region

The fuel-temperature reactivity coefficients predicted by perturbation theory and summarized in Table 4-6 are consistent with the slopes of the fuel-temperature reactivity effect plots shown in Figure 4-9.
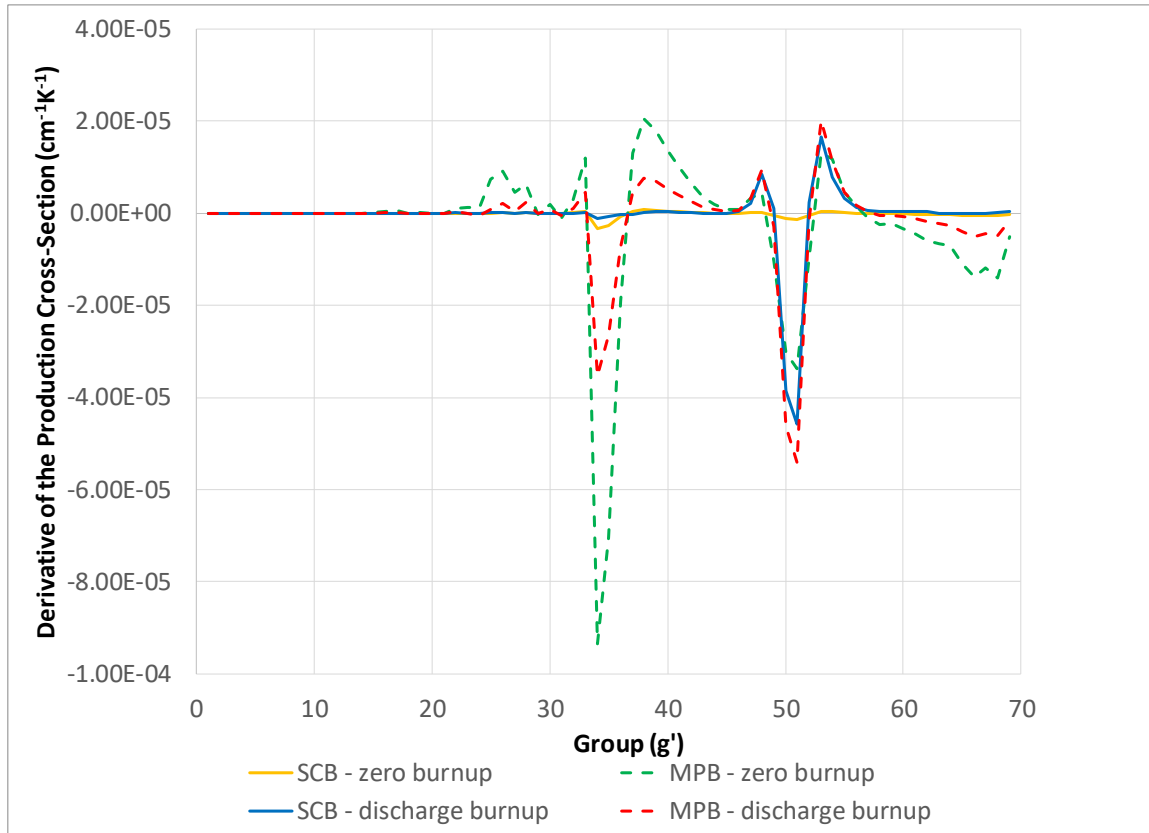
Figure 4-25: Plot of the $\dfrac{\delta \nu \Sigma_{fg',r}}{\delta T_{outer-fuel}}$ term in the outer fuel region

4.4.6 Moderator-Poison Reactivity Effect

An analysis of the moderator-poison reactivity effect, of the MPB and the SCB, at zero burnup and at discharge burnup, can be performed by estimating the reactivity coefficients in the vicinity of the reference point using Eq. (4.3). Considering a variation of the moderator-poison (B or Gd) concentration from zero to 1 ppm (by mass), Eq. (4.3) is used to evaluate the corresponding moderator-poison reactivity

coefficients for the zero-burnup SCB, the zero-burnup MPB, the discharge-burnup

SCB, and discharge-burnup MPB. Results are shown in Table 4-7 for boron and in

Table 4-8 for gadolinium.

To understand what causes the differences in the moderator-poison reactivity

coefficients between the MPB and the SCB, as well as between zero burnup and

discharge burnup, specific terms in Eq. (4.3) can be examined. Because the

perturbation only affects the moderator, the same arguments that were made in

Section 4.4.2 apply here, and Eq. (4.3) simplifies to:

$$\frac{\partial \rho}{\partial C_{B/Gd}} \cong \sum_{g=1}^{G} \sum_{g'=1}^{G} \frac{\delta\left(\Sigma_{s,g'\to g,\text{mod}} - \delta_{g'g}\Sigma_{tg,\text{mod}}\right)}{\delta C_{B/Gd}} \sum_{r\in \text{mod}} \Phi_{g,r}^{0*} \Phi_{g',r}^{0} V_r \qquad (3.10)$$

Because the cross section derivative terms $\dfrac{\delta\left(\Sigma_{s,g'\to g,\text{mod}} - \delta_{g'g}\Sigma_{tg,\text{mod}}\right)}{\delta C_{B/Gd}}$ are the

same for the SCB and the MPB and independent of burnup, while the product of the

adjoint with the direct flux depends on both bundle type and burnup, the differences

between the moderator-poison reactivity coefficients of the MPB and those of the SCB

(bottom rows of Table 4-7 and Table 4-8) are due solely to the differences between

the reference moderator flux and adjoint of the MPB and those of the SCB. Similarly,

the differences between the moderator-poison reactivity coefficients at discharge

burnup and those at zero burnup (right columns of Table 4-7 and Table 4-8) are due

solely to the differences between the reference moderator flux and adjoint at

discharge burnup and those at zero burnup. The moderator direct flux and adjoint for

reference conditions are shown in Figure 4-18 and Figure 4-19, respectively, and

maps of the $\dfrac{\delta\left(\Sigma_{s,g'\to g,\text{mod}} - \delta_{g'g}\Sigma_{tg,\text{mod}}\right)}{\delta C_{B/Gd}}$ derivative terms are shown in Figure 4-26 and

Figure 4-27.

Figure 4-26 and Figure 4-27 show that only the diagonal terms are affected by the addition of poison, which is to be expected as only the capture cross section (part of the removal cross section, which constitutes the diagonal terms) is increased by adding poison to the moderator, which leads to a negative contribution to the reactivity.

Table 4-7 and Table 4-8 show that the moderator-poison reactivity coefficients are negative for both bundle types at both zero burnup and discharge burnup; a fact explained by the increased absorption caused by the poison addition. The absolute values of the reactivity coefficients are ~13% smaller at discharge burnup than at zero burnup for both bundle types and both poison types. At zero burnup, the magnitude of the reactivity coefficient of the MPB is 1.4% smaller than that of the SCB for both boron and gadolinium. At discharge burnup, the magnitude of the reactivity coefficient of the MPB is 0.1% smaller than that of the SCB for both boron and gadolinium.

Overall, the moderator-poison reactivity coefficients show larger changes when going from zero burnup to discharge burnup than when going from SCB to MPB. This is consistent with the fact that the reference flux and adjoint in the moderator change more when going from zero burnup to discharge burnup than when going from SCB to MPB (Figure 4-18 and Figure 4-19).

Table 4-7: Moderator-poison (Boron) Reactivity Coefficients (mk/ppm)

	Zero burnup	**Discharge burnup**	**% Difference**
SCB	-8.52	-7.36	-13.6%
MPB	-8.40	-7.35	-12.5%
% Difference	-1.4%	-0.1%	
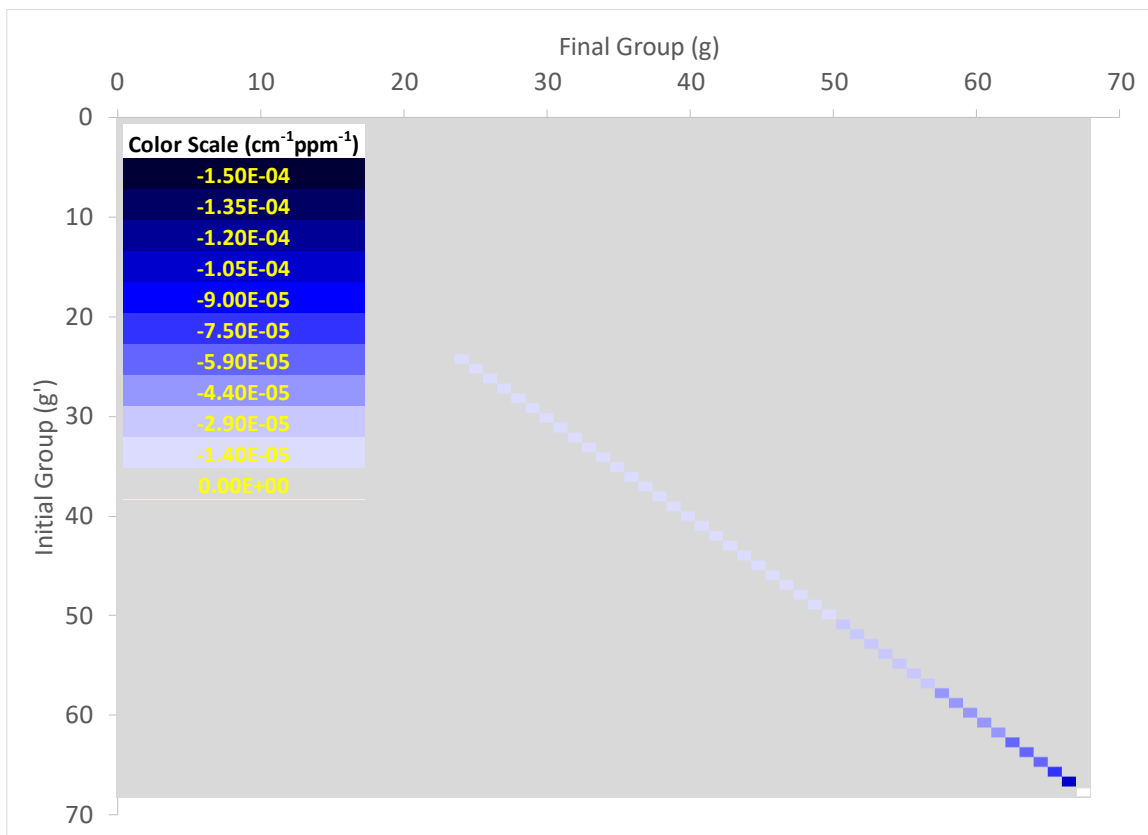
Figure 4-26: Map of the $\dfrac{\delta\left(\Sigma_{s,g'\to g,\mathrm{mod}} - \delta_{g'g}\Sigma_{tg,\mathrm{mod}}\right)}{\delta C_B}$ *terms*

Table 4-8: Moderator-poison (Gadolinium) Reactivity Coefficients (mk/ppm)

	Zero burnup	Discharge burnup	% Difference
SCB	-26.78	-23.01	-14.1%
MPB	-26.41	-22.98	-13.0%
% Difference	-1.4%	-0.1%	
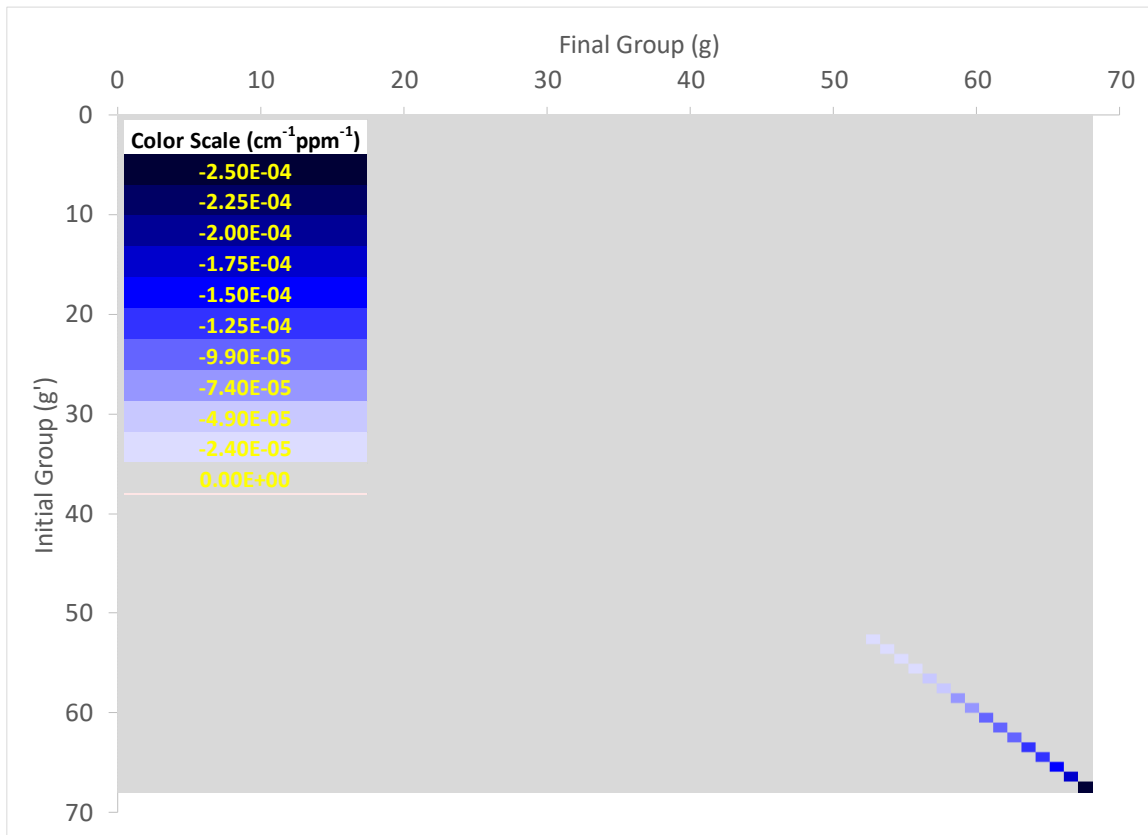
Figure 4-27: Map of the $\dfrac{\delta\left(\Sigma_{s,g'\to g,\mathrm{mod}} - \delta_{g'g}\Sigma_{tg,\mathrm{mod}}\right)}{\delta C_{Gd}}$ *terms*

It is important to note that the moderator-poison reactivity coefficients are determined by the same reference direct flux and adjoint as for the moderator-temperature and the moderator-density reactivity coefficients. However, they are different in both values and behaviour from those because of the simpler, diagonal-only, group dependence of the cross-section derivative terms.

The moderator-poison reactivity coefficients predicted by perturbation theory and summarized in Table 4-7 and Table 4-8 are consistent with the slopes of the moderator-poison reactivity effect plots shown in Figure 4-10 and Figure 4-11.

4.5 Conclusions

The study documented in this chapter shows that the MPB and the SCB have almost identical (within 1.5 mk) reactivity feedback effects when coolant density, moderator density, coolant temperature, moderator temperature, fuel temperature and moderator poison concentration are perturbed over wide ranges. Since the time dependence of core power during a transient induced by perturbing core parameters from their reference, steady-state, values, is determined by the respective reactivity effects, this constitutes a first step in proving that the MPB will have a very similar behaviour to that of the SCB for not only during steady-state operation as captured in Reference [3] but also during transients. It can therefore be concluded that employing MPBs in the core will maintain a comparable operational envelope to a standard natural uranium fuelled configuration

A high-fidelity lattice model comprising of 11 resonance domains for capturing self-shielding effects and 23 radial computational regions providing sufficiently-fine neutronic data is used. Due to the dissimilarities in the radial temperature profiles of the MPB and SCB, a unique radial temperature profile is calculated for each fuel-temperature perturbation case and for each burnup and applied in the lattice model, which allows for a more accurate prediction of the reactivity feedback effects compared to the use of an average fuel temperature as typically done in lattice calculations.

Furthermore, a first-of-a-kind application of the linear perturbation formulism is utilized to explain the small differences in the reactivity feedback effects. The study finds that the differences between the reactivity coefficients of the MPB and those of the SCB (at either zero or discharge burnup) are much smaller than the differences between the reactivity coefficients (of either SCB or MPB) at discharge burnup and those at zero burnup. The differences are explained (using perturbation theory) by the small dissimilarities in the reference flux and adjoint between the MPB and the SCB and the large dissimilarities in the reference flux and adjoint between discharge burnup and zero burnup.

Chapter 5: Reactivity-Device Incremental Cross Sections and Reactivities

This chapter investigates the effect of employing MPB in the core on the reactivity worth of reactivity devices. The study utilizes three-dimensional supercell configurations and the neutron transport code DRAGON to calculate and compare the incremental macroscopic cross sections and reactivity for adjuster absorbers, shutoff absorber rods and liquid zone controllers when surrounded by MPBs and by SCBs. Two geometrical representations of fuel bundles are used: a detailed, cluster, representation, whereby all fuel pins are modeled separately, and an annularized representation, whereby each ring of fuel pins and corresponding coolant is represented as a homogeneous annulus. The latter model is the one customarily used in production calculations for finding cross-section increments of reactivity devices.

CANDU reactors use reactivity devices that are vertically oriented and located between fuel channels. It is anticipated that at most, 4 MPBs will be present in a single fuel channel, located in central axial positions (positions 5 to 8), giving rise to the situation where two MPBs are side-by-side in two adjacent channels as shown in Figure 5-1. It is therefore possible that the reactivity worth of a device may be affected by the type of neighbouring fuel bundle (MPB or SCB) adjacent to it. For example, reactivity devices A and B in Figure 5-1 could potentially have different reactivity worths.
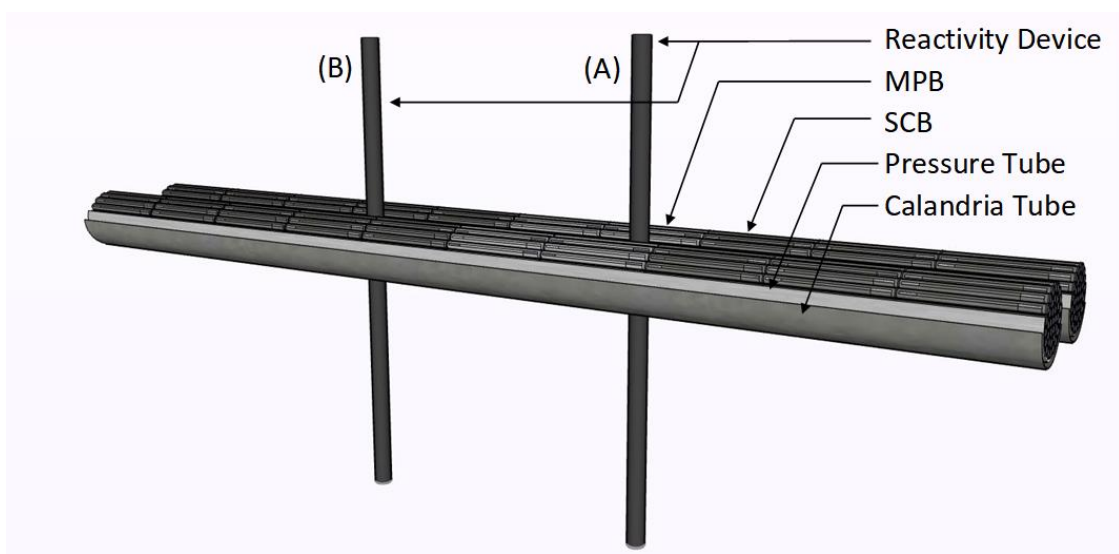
Figure 5-1: Reactivity devices located between CANDU fuel channels

Macroscopic-cross-section increments for reactivity devices located between fuel channels and perpendicular to the reactor axis are typically generated using a 3D supercell neutron transport calculation. The increment of a given macroscopic cross section for a particular reactivity device is defined as the difference between the homogenized supercell cross section in the presence of the reactivity device and the same cross section in the absence of the device. The cross-section increments for each reactivity device, along with the bare lattice two-group cross sections for appropriate burnup values, are the building blocks for the full-core neutron-diffusion model. In order to prove that employing MPBs in the core will not have any noticeable effects on reactor operations, both the bare-lattice macroscopic cross sections and the reactivity-device cross-section increments need to be similar. Previous work [3] has shown that the bare lattice macroscopic cross sections of the SCB are nearly identical to those of the SCB.

If reactivity-device macroscopic cross-section increments can also be demonstrated to be independent of the type of fuel adjacent to the reactivity device, the expectation is that the reactivity-device worth itself will be independent of the type of fuel adjacent to the device. This would be true for any depth of insertion of a given reactivity device and for any combination of reactivity devices present in the core at any given time. Therefore, a comparison of device cross-section increments is a prerequisite first step towards establishing that core reactivity for any combination of reactivity devices and depth of insertion is not significantly affected by the anticipated presence of MPBs in the proximity of reactivity devices. Should such increments be found to be unaffected by the proximity to MPBs, then only a limited number of full-core configurations would have to be analyzed, with the purpose of confirming that core reactivity and transient behavior are, indeed, unaffected by the proximity of MPBs to reactivity devices. Conversely, should such increments be found to be affected by the proximity to MPBs, a larger number of full-core calculations would be needed, to determine which reactivity device configuration is most affected and to adjust operational and control routines to account for the different device reactivity worth.

This chapter presents the results of comparing the reactivity-device incremental cross sections for supercell configurations with either two MPBs or two SCBs on adjacent sides of a reactivity-device. While in reality operators would try to avoid refuelling two adjacent channels with MPBs, such a configuration was chosen for this study because it represents the worst-case scenario from the perspective of potential changes in the reactivity-device worth as a consequence of refuelling with

MPBs. The mixed configuration with an MPB on one side and an SCB of the other side of a reactivity device is assumed to be bounded in macroscopic-cross-section increments by the MPB- and SCB-only configurations.

The reactivity devices that are studied are: stainless-steel adjuster absorbers (AAs), shutoff absorbers (SAs) and liquid zone controllers (LZCs). The MPB specifications used in this work is from the one presented in Chapter 2 and depicted in Figure 2-4.

5.1 CANDU Reactivity Devices

A CANDU reactor has four different reactivity control device systems: the AAs, SAs, LZCs and control absorbers (CAs), which are identical to SAs. Consequently, only the three distinct reactivity devices (AA, SA and LZC) are studied in this work.

The stainless-steel-based AAs are of a pin-in-tube design with a central pin surrounded by a hollow stainless-steel tube. The space between the pin and the tube is occupied by the moderator. The diameters of the pin and of the surrounding tube are constant everywhere along the length of the AA. AAs move within a perforated zirconium-alloy guide tube located in the moderator. There are six different types of AAs, each with a specific pin and tube thickness.

The SAs, which are identical to CAs, are comprised of a hollow tube of cadmium sandwiched between stainless steel layers. The thickness of the two layers of stainless steel, as well as that of the cadmium tube, is the same over the length of the tube. SAs move within a perforated zirconium alloy guide tube located in the moderator. The

geometries, dimensions and material compositions for SAs and AAs are taken from Reference [77], are shown in Figure 5-2, and listed in Table 5-1 and Table 5-2, respectively.

The LZCs consist of a cluster of tubes inside a zirconium-alloy outer tube. Each LZC compartment has at least one scavenger or feeder tube for H_2O and one bubbler or balance tube for Helium. The arrangement of the LZC inside the CANDU core is such that there are either three LZCs stacked on top of each other (central columns) or two LZCs stacked on top of each other (outer columns) resulting in LZC configurations which differ in the number of feeder/balance and scavenger/bubbler pipes that pass through the tank to supply other LZC compartments within the column. In total, there are three different LZC designs depending on the vertical location in the core. They are identified as Type 3S2F, Type 2S1F and Type 1S0F. The first digit in the LZC type corresponds to the number of the scavenger and bubbler tubes, and the second number corresponds to the number of feeder and balance tubes. All LZC compartments are assumed to be made of zirconium alloy with the same material composition as the one for AA and SA guide tubes. The design information for LZC is extracted from Reference [78]. A cross-sectional view of the LZC showing the arrangement of feeder and scavenger tubes within the LZC compartment is presented in Figure 5-3.

Table 5-1: Adjuster Absorber and Shutoff Absorber Design Specifications [77]

AA	SS Tube Outer Diameter (cm)	SS Tube Thickness (cm)	Central Rod Diameter (cm)
Type 1	3.810	0.132	0.577
Type 2	3.810	0.087	0.649
Type 3	3.810	0.185	1.069
Type 4	3.810	0.185	0.790
Type 5	3.810	0.061	0.500
Type 6	3.810	0.087	0.662
SA			
Inner SS Tube I.D. (cm)	**Cadmium Tube I.D. (cm)**	**Cadmium Tube O.D. (cm)**	**Outer SS Tube O.D. (cm)**
5.321	5.398	5.474	5.560

Table 5-2: Adjuster Absorber and Shutoff Absorber Material Compositions [77]

Stainless Steel	Fe = 69.936 wt% Cr = 18.198 wt% Ni = 8.893 wt% Mn = 1.680 wt% Si = 0.520 wt% Cu = 0.323 wt% Mo = 0.263 wt% Co = 0.070 wt% N = 0.057 wt% C = 0.022 wt%
Zirconium-II	Natural Zr = 98.209 wt% Fe = 0.135 wt% Cr = 0.100 wt% Ni = 0.055 wt%
Cadmium	Natural Cd = 100%
Guide Tube	Zirconium-II with 36% perforation
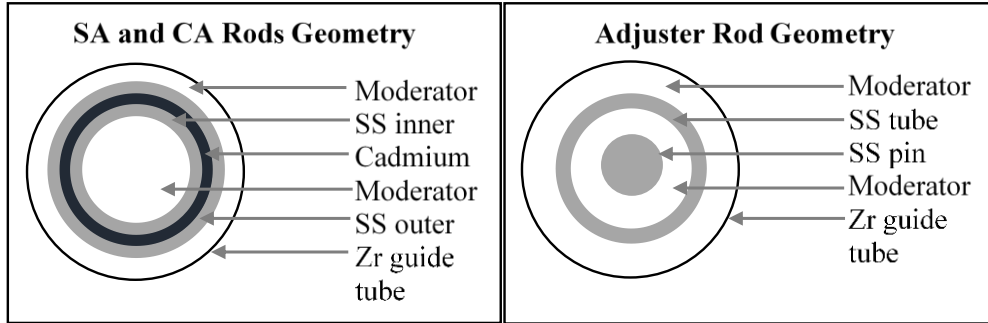
Figure 5-2: Cross-sectional view of CANDU adjuster absorber and shutoff absorber
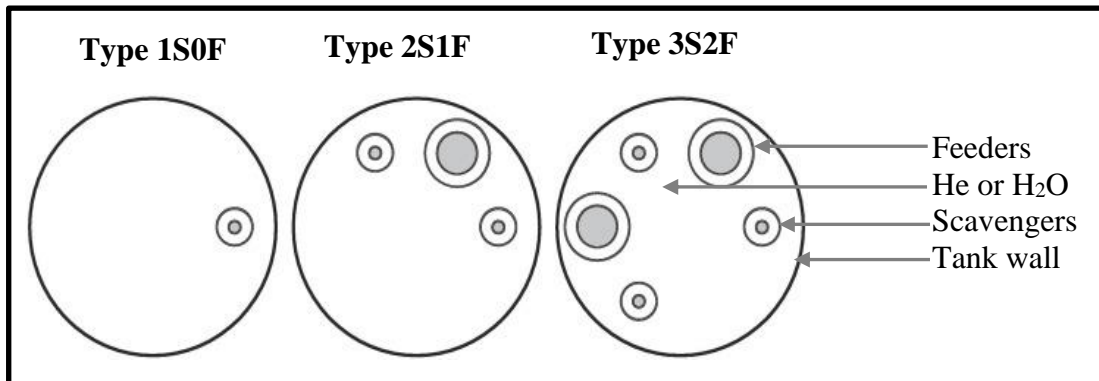
Figure 5-3: Cross-sectional view of CANDU liquid zone controllers

5.2   Three-Dimensional Supercell Model

As mentioned earlier, the orthogonal orientation of the CANDU reactivity control devices with respect to the fuel channel requires a full 3D model to capture the variations in neutron flux along the length of the fuel channel and locally, near

reactivity control device components. The 3D supercell model is illustrated in Figure

5-4.
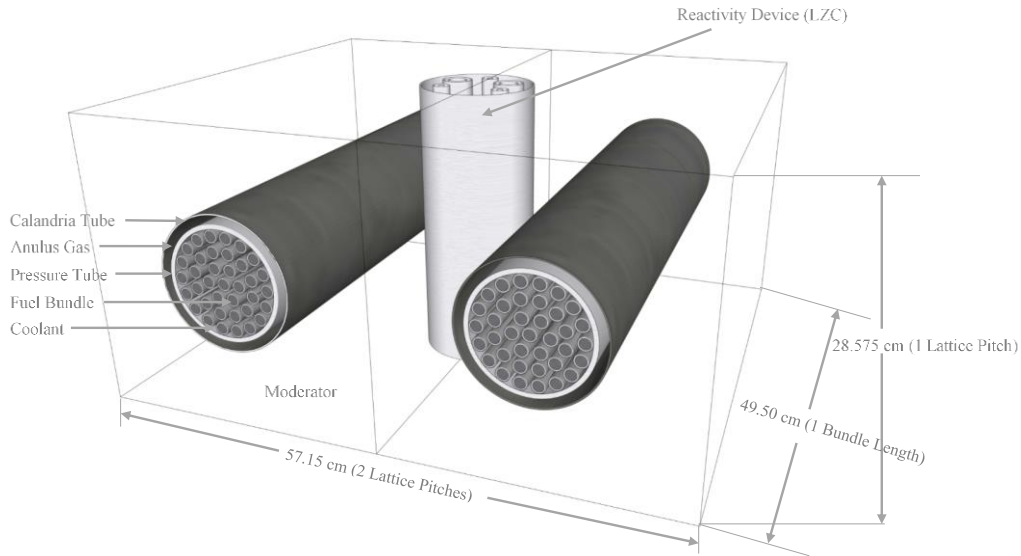
Figure 5-4: A 3D CANDU supercell configuration with two fuel lattices and a reactivity device (LZC) in the axial center

5.2.1   Homogenization Region

To capture the change in lattice homogenized macroscopic cross sections induced by the presence of a reactivity device (cross-section increments), two different regions are defined: an inner region and an outer region, as shown in Figure 5-5, each with a volume equal to that of a 3D lattice cell of size 28.75 cm × 28.75 cm × 49.50 cm. The inner region extends from the first bundle mid-plane to the second bundle mid-plane. The outer region consists of the two regions extending from each

bundle mid-plane to the respective model boundary. Only the inner region is specified as the region-of-interest and is used to homogenize and energy-condense macroscopic cross sections in order to calculate the incremental cross sections and supercell reactivity in the presence of a reactivity device.

Two sets of homogenized cross sections are calculated: one in the absence of the reactivity device, and one in its presence. The absence of the reactivity device is defined as rod removed for AA and SA and as fully drained for LZC. The presence of the reactivity device is defined as rod inserted for AA and SA and as completely filled with light water for LZC.
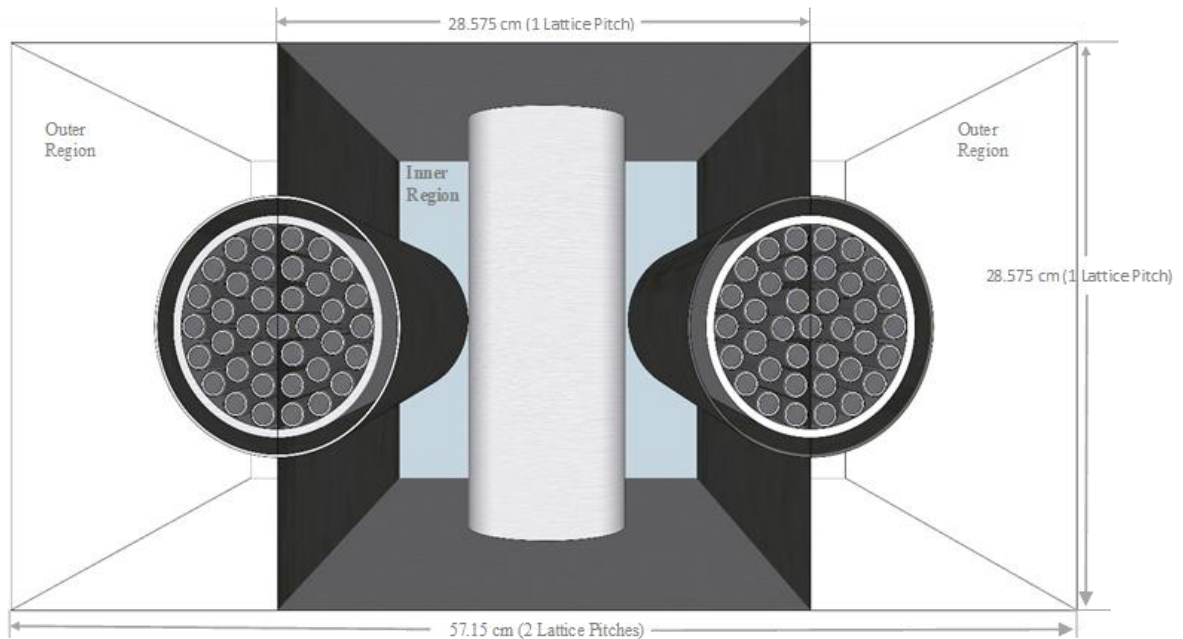
Figure 5-5: CANDU 3D supercell face view and homogenized central region

5.2.2   Representation of Fuel-Bundle Geometry

Latest versions of the DRAGON code are capable of using explicit, cluster, representations of the 37 fuel elements in each of the two fuel bundles included in the supercell model, whereas, traditional 3D models of CANDU reactivity devices, developed in the late 1990s, have used simplified geometries of fuel bundles. Such models are still used in routine production calculations as described in Reference [50]. The region inside the pressure tube is usually pre-homogenized into four concentric annuli, each corresponding to a fuel ring. The homogenized properties of each annulus are determined by flux-volume homogenization of fuel, cladding and coolant using the flux solutions of an equivalent problem in 2D geometry. This work calculates incremental cross sections using both a detailed model and an annularized model of the fuel bundles in order to investigate any differences between the two sets of calculated cross-section increments.

5.3   DRAGON Model and Calculations

Calculations of the incremental cross sections for reactivity devices are performed using DRAGON ver. 3.06 [25] and the 69-group IAEA WLUP microscopic cross library [53]. For the current analysis, the 69-energy-group CP method was applied to a 3D supercell configuration comprising of two side-by-side fuel lattices oriented parallel to the reactor axis and a reactivity device perpendicular to the reactor axis, located between the two cells, midway along the axial length of the fuel bundles, as shown in Figure 5-4.

5.3.1 Detailed Bundle Model

Fuel pins in each bundle are represented explicitly, using the "CLUSTER" geometry type in DRAGON. Similar to Section 4.2, the fuel pins are discretized into 11 radial regions and the modified Stamm'ler method [75] is used to perform resonance treatment treating each radial region as a distinct resonance domain. Because the MPB and SCB have identical geometries, the same 3D models can be used to represent either fuel bundle, with only the composition of the fuel material in each region being different. The outermost region of the MPB contains enriched fuel and the 10 remaining regions contain depleted fuel. All SCB regions contain natural uranium.

No additional spatial discretization is added in the fuel or other parts of the model due to the complex and computationally intensive nature of the 3D transport solution. Reflective boundaries are used on all six boundaries of the supercell model, thus simulating an infinite repeated array of the base supercell configuration consisting of two fuel bundles and a control device.

The fuel temperatures in each discrete region of the pin are set, for each bundle type, according to the calculated radial temperature profiles as presented in Section 4.2 given at zero burnup or 20-day burnup. Given that the radial temperature profile for the MPB is significantly different from that for the SCB, the use of correct radial variation of the fuel temperatures ensures more accurate prediction of the reactivity device incremental cross sections compared to the use of a uniform fuel temperature as typically done in supercell calculations.

5.3.2   Annularized-Bundle Model

The annularized model is obtained by first performing 2D neutron transport calculations in 69-energy groups (including self-shielding), followed by material homogenization into annuli. Four different fuel "pastes" are computed, one for each annular region corresponding to each fuel ring. Each paste is obtained by homogenizing fuel, cladding and coolant materials. From the 2D calculation step, a new set of 69-group macroscopic cross sections is formed for each paste, which is then used in the 3D calculation. The cluster geometry of the 37-element fuel pins and the annularized geometry with concentric homogenized annuli are depicted in Figure 5-6. Aside from the homogenization of the fuel, cladding and coolant, the annularized-model parameters such as spatial discretization and tracking path density are the same as for the detailed model.
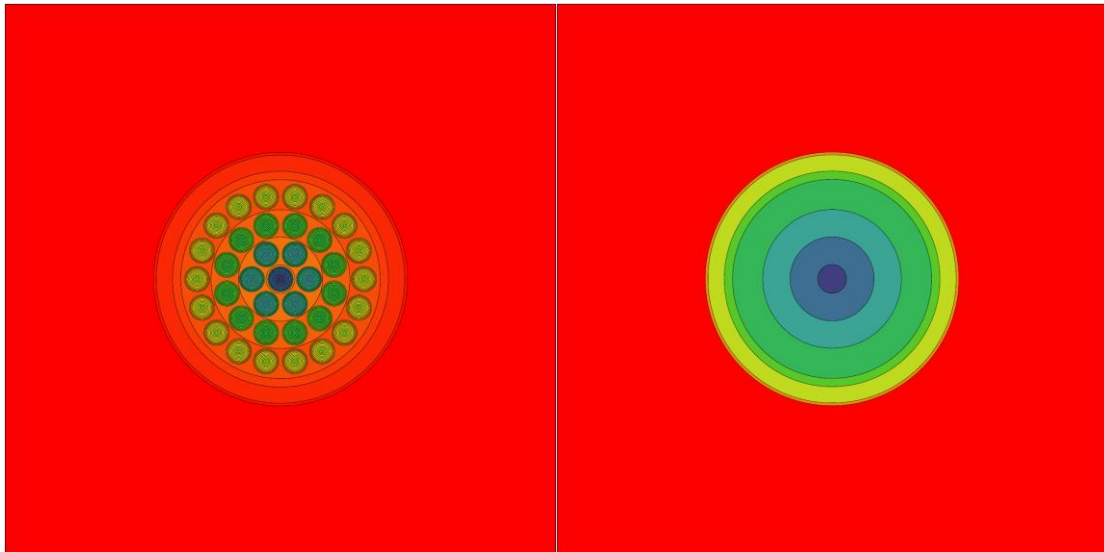
Figure 5-6: 37-Element explicit (left) and annularized (right) models

5.3.3 Supercell Calculations

Three-dimensional supercell calculations are performed for the MPB, as well as the SCB, at zero burnup and 20-day burnup (906.62 MWd/t(U)) which corresponds to the maximum residence time of the MPB inside the core. To ensure accurate representation of the fuel compositions at 20-day burnup, burnup calculations are performed for both MPB and SCB using 2D lattice models and small burnup steps as described in Section 4.2. Detailed fuel compositions in each fuel ring are then transferred to the 3D supercell models to determine the incremental cross sections and reactivity changes for AA, SA and LZC.

Three cases are analyzed for each reactivity device and for each bundle type: 1) two bundles, 2) two bundles and guide tube in place, 3) two bundles, guide tube and reactivity device in place. Macroscopic cross sections are calculated in 69-energy groups then condensed into two energy groups and spatially homogenized. In total, for each reactivity device, two sets of incremental cross sections are defined:

(1) $\Delta\Sigma^{\text{Guide Tube}}$ – Incremental cross sections for a (empty) tube", unoccupied by the movable absorber that is part of the reactivity device. For liquid zone controllers, the tube represents the outer LZC compartment and the inner scavenger and feeder tubes. The part of LZC that is inside the outer tube and outside the scavenger/feeder tubes is filled with helium. For solid control rods, the tube is the guide tube. The guide tube is filled with moderator.

(2) $\Delta\Sigma^{Device}$ – Incremental cross sections for a rod-based reactivity device that is

   fully inserted or a LZC that is completely filled with light water within the cell

   limits.

   Table 5-3 shows the set of eight incremental cross sections that are computed

with reference to the MPB and the SCB. For the sake of comparison, incremental cross

sections (for both SCB and MPB) are calculated using both the detailed model which

uses the explicit "cluster" geometry available in DRAGON and the simplified

(annularized) fuel-bundle model used in production calculations.

Table 5-3: Set of Incremental Macroscopic Cross Sections

Incremental	Description of cross section
$\Delta\Sigma_{tr1}$	Incremental fast transport cross section (cm^{-1})
$\Delta\Sigma_{tr2}$	Incremental thermal transport cross section (cm^{-1})
$\Delta\Sigma_{a1}$	Incremental fast absorption cross section (cm^{-1})
$\Delta\Sigma_{a2}$	Incremental thermal absorption cross section (cm^{-1})
$\Delta\Sigma_{s12}$	Incremental scattering cross section from group 1 to 2 (down-scattering) (cm^{-1})
$\Delta\Sigma_{s21}$	Incremental scattering cross section from group 2 to 1 (up-scattering) (cm^{-1})
$\Delta\nu\Sigma_{f1}$	Incremental fast production cross section (cm^{-1})
$\Delta\nu\Sigma_{f2}$	Incremental thermal production cross section (cm^{-1})

5.4   Simulation Results

   Incremental macroscopic cross sections and corresponding supercell reactivity

increments are presented in Table 5-4 to Table 5-14 for both MPB and SCB.

Differences are presented as MPB value – SCB value, while percentage differences are

presented as (MPB value – SCB value)/SCB value ×100%. Because guide tubes for different AA types are identical, their incremental properties are only presented once.

It is worth noting that because the supercell boundary conditions are periodic, the supercell reactivity increment corresponding to the insertion of the reactivity device does not represent the reactivity worth of a single device, but rather the reactivity worth of an array of devices repeated every two lattice pitches, in an infinite lattice. Nonetheless, the percent differences between the MPB- and SCB-based supercell reactivity increments are representative of the percent difference between the device reactivity worth when located near a MPB or a SCB.

5.4.1   Incremental Cross Sections and Reactivities at Zero Burnup

The two-group homogenized incremental cross sections, $\Delta\Sigma^{Device}$, and incremental supercell reactivity for AA, SA and LZC are first calculated using fuel properties corresponding to zero burnup and presented in Table 5-4, Table 5-5, and Table 5-6, respectively. The reference supercell reactivity is 42.36 mk for the SCB and 43.20 mk for the MPB.

The incremental macroscopic cross sections of all reactivity devices are very similar for the two bundle types. It bears mentioning that such cross-section increments represent merely a convenient mathematical way of modelling a reactivity device in a two-group diffusion calculation and cannot be directly related to the neutron cross sections of the material making up the device. It is obvious, for example, that fission and production cross sections for the reactivity-device materials are zero, whereas increments for such average macroscopic cross sections can be

non-zero. This is due to the fact that the homogenization volume includes fuel. Differences between device cross-section increments obtained for the two fuel types do not, therefore, have any operational implications. The operationally-meaningful quantity is the percent difference between the supercell reactivity increments. It is desirable that the supercell reactivity increments corresponding to a device's insertion be very similar for the two bundle types.

When comparing the calculated supercell reactivity increments for the MPB and the SCB, they are found to be very similar for all reactivity devices, with the difference being less than 2.0% (Table 5-4, Table 5-5, and Table 5-6). The largest difference for AA occurs for Type 3, whereby the difference is 3.94 mk (-1.9%). For SA, the difference is 19.71 mk (-1.7%). The highest difference for LZC occurs for Type 1S0F whereby the difference is 1.58 mk (-0.6%).

The incremental cross sections and incremental supercell reactivity for guide tubes at zero burnup are shown in Table 5-7 and are very similar for both bundle types. The calculated MPB-to-SCB supercell reactivity-increment differences are less than 5.0% for all guide tubes.

Table 5-4: Adjuster Absorbers Homogenized Incremental Cross Sections at Zero Burnup

	$\Delta\Sigma_{tr1}$ (cm^{-1})	$\Delta\Sigma_{tr2}$ (cm^{-1})	$\Delta\Sigma_{a1}$ (cm^{-1})	$\Delta\Sigma_{a2}$ (cm^{-1})	$\Delta\Sigma_{s12}$ (cm^{-1})	$\Delta\Sigma_{s21}$ (cm^{-1})	$\Delta\nu\Sigma_{f1}$ (cm^{-1})	$\Delta\nu\Sigma_{f2}$ (cm^{-1})	$\Delta\rho$ (mk)
Type 1									
MPB	1.5333E-03	1.4322E-03	2.5687E-05	5.6128E-04	-2.6015E-05	9.4300E-06	-8.2033E-07	5.2822E-05	-1.3094E+02
SCB	1.5334E-03	1.4295E-03	2.5574E-05	5.5968E-04	-2.6166E-05	1.0615E-05	-9.7293E-07	5.2250E-05	-1.3340E+02
Diff.	-0.01%	0.19%	0.44%	0.29%	-0.58%	-11.17%	-15.68%	1.09%	-1.88%
Type 2									
MPB	1.2486E-03	1.1635E-03	2.0934E-05	4.5767E-04	-2.1236E-05	7.6802E-06	-6.6879E-07	4.3536E-05	-1.0702E+02
SCB	1.2487E-03	1.1613E-03	2.0844E-05	4.5637E-04	-2.1361E-05	8.6481E-06	-7.9413E-07	4.3076E-05	-1.0905E+02
Diff.	-0.01%	0.20%	0.44%	0.28%	-0.59%	-11.19%	-15.78%	1.07%	-1.89%
Type 3									
MPB	2.8979E-03	2.4280E-03	4.7973E-05	9.1200E-04	-4.9809E-05	1.5628E-05	-1.4046E-06	8.9294E-05	-2.1110E+02
SCB	2.8983E-03	2.4236E-03	4.7772E-05	9.0949E-04	-5.0028E-05	1.7566E-05	-1.6540E-06	8.8379E-05	-2.1503E+02
Diff.	-0.02%	0.18%	0.42%	0.28%	-0.44%	-11.03%	-15.07%	1.04%	-1.86%
Type 4									
MPB	2.3143E-03	2.0531E-03	3.8553E-05	7.8637E-04	-3.9519E-05	1.3350E-05	-1.1783E-06	7.5364E-05	-1.8242E+02
SCB	2.3146E-03	2.0494E-03	3.8386E-05	7.8415E-04	-3.9719E-05	1.5015E-05	-1.3917E-06	7.4544E-05	-1.8584E+02
Diff.	-0.01%	0.18%	0.43%	0.28%	-0.50%	-11.09%	-15.33%	1.10%	-1.87%
Type 5									
MPB	8.2469E-04	7.9526E-04	1.3879E-05	3.1787E-04	-1.3967E-05	5.2998E-06	-4.5702E-07	2.9904E-05	-7.4602E+01
SCB	8.2474E-04	7.9361E-04	1.3819E-05	3.1698E-04	-1.4055E-05	5.9718E-06	-5.4452E-07	2.9603E-05	-7.6017E+01
Diff.	-0.01%	0.21%	0.44%	0.28%	-0.63%	-11.25%	-16.07%	1.01%	-1.90%
Type 6									
MPB	1.268E-03	1.178E-03	2.125E-05	4.630E-04	-2.158E-05	7.772E-06	-6.7750E-07	4.4102E-05	-1.0825E+02
SCB	1.268E-03	1.176E-03	2.116E-05	4.616E-04	-2.170E-05	8.752E-06	-8.0423E-07	4.3634E-05	-1.1029E+02
Diff.	-0.01%	0.20%	0.43%	0.28%	-0.58%	-11.19%	-15.76%	1.07%	-1.89%

Table 5-5: Shutoff Absorber Homogenized Incremental Cross Sections at Zero Burnup

	$\Delta\Sigma_{tr1}$ (cm^{-1})	$\Delta\Sigma_{tr2}$ (cm^{-1})	$\Delta\Sigma_{a1}$ (cm^{-1})	$\Delta\Sigma_{a2}$ (cm^{-1})	$\Delta\Sigma_{s12}$ (cm^{-1})	$\Delta\Sigma_{s21}$ (cm^{-1})	$\Delta\nu\Sigma_{f1}$ (cm^{-1})	$\Delta\nu\Sigma_{f2}$ (cm^{-1})	$\Delta\rho$ (mk)
MPB	1.8937E-03	1.2541E-03	6.8438E-05	6.2005E-03	-4.9434E-05	9.3150E-05	-5.0218E-06	5.6479E-04	-1.1514E+03
SCB	1.8891E-03	1.2417E-03	6.7981E-05	6.1902E-03	-5.0472E-05	1.0608E-04	-6.2747E-06	5.5907E-04	-1.1711E+03
Diff.	0.24%	1.00%	0.67%	0.17%	-2.06%	-12.19%	-19.97%	1.02%	-1.68%

Table 5-6: Liquid Zone Controllers Homogenized Incremental Cross Sections at Zero Burnup

	$\Delta\Sigma_{tr1}$ (cm^{-1})	$\Delta\Sigma_{tr2}$ (cm^{-1})	$\Delta\Sigma_{a1}$ (cm^{-1})	$\Delta\Sigma_{a2}$ (cm^{-1})	$\Delta\Sigma_{s12}$ (cm^{-1})	$\Delta\Sigma_{s21}$ (cm^{-1})	$\Delta\nu\Sigma_{f1}$ (cm^{-1})	$\Delta\nu\Sigma_{f2}$ (cm^{-1})	$\Delta\rho$ (mk)
Type 3S2F									
MPB	1.7552E-02	1.4925E-01	1.0018E-04	1.0703E-03	2.1011E-03	2.8279E-06	8.5348E-05	1.1101E-05	-2.0041E+02
SCB	1.7580E-02	1.4883E-01	1.0171E-04	1.0675E-03	2.1028E-03	2.7034E-06	8.7936E-05	1.1999E-05	-2.0177E+02
Diff.	-0.16%	0.28%	-1.51%	0.26%	-0.08%	4.61%	-2.94%	-7.48%	-0.68%
Type 2S1F									
MPB	2.0220E-02	1.6689E-01	1.1507E-04	1.1950E-03	2.4215E-03	3.0946E-06	9.8186E-05	1.2183E-05	-2.2215E+02
SCB	2.0251E-02	1.6645E-01	1.1679E-04	1.1922E-03	2.4233E-03	2.9197E-06	1.0118E-04	1.3209E-05	-2.2365E+02
Diff.	-0.15%	0.27%	-1.47%	0.24%	-0.07%	5.99%	-2.96%	-7.77%	-0.67%
Type 1S0F									
MPB	2.2959E-02	1.8422E-01	1.3059E-04	1.3172E-03	2.7513E-03	3.3359E-06	1.1145E-04	1.2836E-05	-2.4303E+02
SCB	2.2992E-02	1.8373E-01	1.3251E-04	1.3141E-03	2.7531E-03	3.1029E-06	1.1486E-04	1.4103E-05	-2.4461E+02
Diff.	-0.14%	0.27%	-1.45%	0.23%	-0.06%	7.51%	-2.96%	-8.98%	-0.65%

Table 5-7: Guide Tubes Homogenized Incremental Cross Sections at Zero Burnup

	$\Delta\Sigma_{tr1}$ (cm^{-1})	$\Delta\Sigma_{tr2}$ (cm^{-1})	$\Delta\Sigma_{a1}$ (cm^{-1})	$\Delta\Sigma_{a2}$ (cm^{-1})	$\Delta\Sigma_{s12}$ (cm^{-1})	$\Delta\Sigma_{s21}$ (cm^{-1})	$\Delta\nu\Sigma_{f1}$ (cm^{-1})	$\Delta\nu\Sigma_{f2}$ (cm^{-1})	$\Delta\rho$ (mk)
				AA-Guide Tube					
MPB	-3.9092E-02	-9.9461E-02	-6.9678E-05	2.7504E-06	-3.4567E-03	3.2313E-05	-1.9559E-04	-1.6347E-05	-1.1491E+02
SCB	-3.9142E-02	-9.9389E-02	-7.3125E-05	3.2889E-06	-3.4616E-03	3.7221E-05	-2.0322E-04	-1.5636E-05	-1.2003E+02
Diff.	-0.13%	0.07%	-4.71%	-16.37%	-0.14%	-13.18%	-3.76%	4.54%	-4.46%
				SA-Guide Tube					
MPB	-3.9217E-02	-9.9432E-02	-7.2286E-05	-7.6344E-06	-3.4477E-03	3.2019E-05	-1.9531E-04	-1.7894E-05	-1.1180E+02
SCB	-3.9266E-02	-9.9360E-02	-7.5731E-05	-7.0236E-06	-3.4526E-03	3.6897E-05	-2.0293E-04	-1.7120E-05	-1.1685E+02
Diff.	-0.13%	0.07%	-4.55%	8.70%	-0.14%	-13.22%	-3.76%	4.52%	-4.52%
				LZC-3S2F Outer/Scavenger/Feeder Tubes					
MPB	-1.1222E-02	-8.0591E-03	-2.7121E-07	2.3108E-04	-1.8487E-04	-6.0337E-09	-6.7994E-06	3.1768E-05	-4.9715E+01
SCB	-1.1236E-02	-8.0632E-03	-1.1058E-06	2.3023E-04	-1.8496E-04	3.6373E-07	-7.1015E-06	3.1258E-05	-5.0517E+01
Diff.	-0.12%	-0.05%	-75.48%	0.37%	-0.05%	-101.66%	-4.25%	1.633%	-1.61%
				LZC-2S1F Outer/Scavenger/Feeder Tubes					
MPB	-1.3602E-02	-1.8604E-02	-1.3272E-05	1.5275E-04	-4.6217E-04	-3.7461E-08	-1.7781E-05	3.5278E-05	-3.6188E+01
SCB	-1.3618E-02	-1.8600E-02	-1.4227E-05	1.5180E-04	-4.6226E-04	4.0940E-07	-1.8435E-05	3.4510E-05	-3.6938E+01
Diff.	-0.11%	0.02%	-6.71%	0.63%	-0.02%	-109.15%	-3.55%	2.22%	-2.07%
				LZC-1S0F Outer/Scavenger Tubes					
MPB	-1.6063E-02	-2.9077E-02	-2.6923E-05	7.5303E-05	-7.5074E-04	-4.5693E-08	-2.9254E-05	3.9335E-05	-2.3130E+01
SCB	-1.6080E-02	-2.9067E-02	-2.8013E-05	7.4241E-05	-7.5080E-04	4.8715E-07	-3.0277E-05	3.8316E-05	-2.3842E+01
Diff.	-0.10%	0.03%	-3.89%	1.43%	-0.01%	-109.38%	-3.38%	2.66%	-3.08%

5.4.2   Incremental Cross Sections and Reactivities at 20-Day Burnup

For 20-day burnup, the 2-group homogenized incremental reactivity device cross sections, $\Delta\Sigma^{Device}$, and incremental supercell reactivity for AA, SA and LZC are presented in Table 5-8, Table 5-9 and Table 5-10. The reference supercell reactivity is 13.73 mk for the SCB and 14.00 mk for the MPB.

Just like in the zero-burnup case, the incremental macroscopic cross sections of all reactivity devices at 20-day burnup are very similar for the two bundle types. The difference in incremental supercell reactivity between the MPB and SCB is less than 1.5% for all reactivity devices. The highest incremental-reactivity difference for AA occurs for Type 3 whereby the difference is 2.18 mk (-1.1%). For SA, the incremental-reactivity difference is 11.11 mk (-1.0%). The highest incremental-reactivity difference for LZC occurs for Type 3S2F whereby the difference is 0.20 mk (-0.1%).

The incremental cross sections and incremental supercell reactivity for guide tubes at 20-day burnup are given in Table 5-11 and are very similar for both bundles. The calculated difference in incremental supercell reactivity between the MPB and SCB is less than 4.0% for all guide tubes.

Table 5-8: Adjuster Absorbers Homogenized Incremental Cross Sections at 20-day Burnup

	$\Delta\Sigma_{tr1}$ (cm^{-1})	$\Delta\Sigma_{tr2}$ (cm^{-1})	$\Delta\Sigma_{a1}$ (cm^{-1})	$\Delta\Sigma_{a2}$ (cm^{-1})	$\Delta\Sigma_{s12}$ (cm^{-1})	$\Delta\Sigma_{s21}$ (cm^{-1})	$\Delta\nu\Sigma_{f1}$ (cm^{-1})	$\Delta\nu\Sigma_{f2}$ (cm^{-1})	$\Delta\rho$ (mk)
					Type 1				
MPB	1.5336E-03	1.4505E-03	2.5638E-05	5.7174E-04	-2.6009E-05	9.9516E-06	-8.3585E-07	6.4852E-05	-1.2415E+02
SCB	1.5336E-03	1.4491E-03	2.5535E-05	5.7069E-04	-2.6105E-05	1.0949E-05	-9.7009E-07	6.4603E-05	-1.2551E+02
Diff.	0.00%	0.10%	0.40%	0.18%	-0.37%	-9.11%	-13.84%	0.38%	-1.08%
					Type 2				
MPB	1.2489E-03	1.1785E-03	2.0895E-05	4.6625E-04	-2.1230E-05	8.1062E-06	-6.8162E-07	5.3373E-05	-1.0150E+02
SCB	1.2489E-03	1.1772E-03	2.0813E-05	4.6540E-04	-2.1310E-05	8.9206E-06	-7.9163E-07	5.3174E-05	-1.0262E+02
Diff.	0.00%	0.11%	0.39%	0.18%	-0.37%	-9.13%	-13.90%	0.37%	-1.09%
					Type 3				
MPB	2.8986E-03	2.4606E-03	4.7880E-05	9.2961E-04	-4.9790E-05	1.6510E-05	-1.4324E-06	1.0912E-04	-2.0023E+02
SCB	2.8988E-03	2.4583E-03	4.7699E-05	9.2798E-04	-4.9928E-05	1.8142E-05	-1.6508E-06	1.0872E-04	-2.0241E+02
Diff.	-0.01%	0.10%	0.38%	0.18%	-0.28%	-9.00%	-13.23%	0.37%	-1.08%
					Type 4				
MPB	2.3148E-03	2.0801E-03	3.8476E-05	8.0126E-04	-3.9510E-05	1.4094E-05	-1.2003E-06	9.2295E-05	-1.7299E+02
SCB	2.3149E-03	2.0781E-03	3.8327E-05	7.9983E-04	-3.9635E-05	1.5497E-05	-1.3883E-06	9.1956E-05	-1.7487E+02
Diff.	-0.00%	0.10%	0.39%	0.18%	-0.31%	-9.05%	-13.54%	0.37%	-1.08%
					Type 5				
MPB	8.2487E-04	8.0531E-04	1.3854E-05	3.2376E-04	-1.3961E-05	5.5920E-06	-4.6559E-07	3.6708E-05	-7.0744E+01
SCB	8.2484E-04	8.0437E-04	1.3800E-05	3.2318E-04	-1.4018E-05	6.1572E-06	-5.4247E-07	3.6585E-05	-7.1525E+01
Diff.	0.00%	0.12%	0.40%	0.18%	-0.40%	-9.18%	-14.17%	0.34%	-1.09%
					Type 6				
MPB	1.268E-03	1.193E-03	2.121E-05	4.716E-04	-2.157E-05	8.204E-06	-6.9050E-07	5.4057E-05	-1.0266E+02
SCB	1.268E-03	1.192E-03	2.113E-05	4.708E-04	-2.165E-05	9.028E-06	-8.0178E-07	5.3854E-05	-1.0379E+02
Diff.	0.00%	0.11%	0.39%	0.18%	-0.37%	-9.13%	-13.88%	0.38%	-1.09%

Table 5-9: Shutoff Absorber Homogenized Incremental Cross Sections at 20-day Burnup

	$\Delta\Sigma_{tr1}$ (cm^{-1})	$\Delta\Sigma_{tr2}$ (cm^{-1})	$\Delta\Sigma_{a1}$ (cm^{-1})	$\Delta\Sigma_{a2}$ (cm^{-1})	$\Delta\Sigma_{s12}$ (cm^{-1})	$\Delta\Sigma_{s21}$ (cm^{-1})	$\Delta\nu\Sigma_{f1}$ (cm^{-1})	$\Delta\nu\Sigma_{f2}$ (cm^{-1})	$\Delta\rho$ (mk)
MPB	1.8920E-03	1.3296E-03	6.8300E-05	6.3302E-03	-4.9510E-05	9.8135E-05	-5.1987E-06	6.8544E-04	-1.0864E+03
SCB	1.8874E-03	1.3219E-03	6.7863E-05	6.3245E-03	-5.0212E-05	1.0899E-04	-6.2975E-06	6.8268E-04	-1.0975E+03
Diff.	0.24%	0.58%	0.64%	0.09%	-1.40%	-9.96%	-17.45%	0.41%	-1.01%

Table 5-10: Liquid Zone Controllers Homogenized Incremental Cross Sections at 20-day Burnup

	$\Delta\Sigma_{tr1}$ (cm^{-1})	$\Delta\Sigma_{tr2}$ (cm^{-1})	$\Delta\Sigma_{a1}$ (cm^{-1})	$\Delta\Sigma_{a2}$ (cm^{-1})	$\Delta\Sigma_{s12}$ (cm^{-1})	$\Delta\Sigma_{s21}$ (cm^{-1})	$\Delta\nu\Sigma_{f1}$ (cm^{-1})	$\Delta\nu\Sigma_{f2}$ (cm^{-1})	$\Delta\rho$ (mk)
Type 3S2F									
MPB	1.7564E-02	1.5232E-01	1.0030E-04	1.0865E-03	2.1023E-03	2.3976E-06	8.5825E-05	-4.8987E-07	-1.9462E+02
SCB	1.7587E-02	1.5213E-01	1.0152E-04	1.0853E-03	2.1036E-03	2.1955E-06	8.7946E-05	1.7260E-08	-1.9482E+02
Diff.	-0.13%	0.13%	-1.20%	0.11%	-0.06%	9.21%	-2.41%	-2938.18%	-0.10%
Type 2S1F									
MPB	2.0233E-02	1.7030E-01	1.1523E-04	1.2125E-03	2.4227E-03	2.5898E-06	9.8737E-05	-1.2936E-06	-2.1550E+02
SCB	2.0258E-02	1.7009E-01	1.1660E-04	1.2112E-03	2.4241E-03	2.3295E-06	1.0119E-04	-7.2274E-07	-2.1567E+02
Diff.	-0.12%	0.12%	-1.17%	0.11%	-0.06%	11.17%	-2.42%	78.98%	-0.08%
Type 1S0F									
MPB	2.2973E-02	1.8793E-01	1.3080E-04	1.3355E-03	2.7525E-03	2.7500E-06	1.1208E-04	-2.6190E-06	-2.3542E+02
SCB	2.2999E-02	1.8770E-01	1.3234E-04	1.3342E-03	2.7539E-03	2.4260E-06	1.1487E-04	-1.8997E-06	-2.3556E+02
Diff.	-0.11%	0.12%	-1.16%	0.10%	-0.05%	13.36%	-2.43%	37.87%	-0.06%

Table 5-11: Guide Tubes Homogenized Incremental Cross Sections at 20-day Burnup

	$\Delta\Sigma_{tr1}$ (cm^{-1})	$\Delta\Sigma_{tr2}$ (cm^{-1})	$\Delta\Sigma_{a1}$ (cm^{-1})	$\Delta\Sigma_{a2}$ (cm^{-1})	$\Delta\Sigma_{s12}$ (cm^{-1})	$\Delta\Sigma_{s21}$ (cm^{-1})	$\Delta\nu\Sigma_{f1}$ (cm^{-1})	$\Delta\nu\Sigma_{f2}$ (cm^{-1})	$\Delta\rho$ (mk)
					AA-Guide Tube				
MPB	-3.9114E-02	-9.9793E-02	-7.1129E-05	3.0360E-05	-3.4577E-03	3.6221E-05	-1.9690E-04	3.5271E-05	-1.1662E+02
SCB	-3.9154E-02	-9.9753E-02	-7.4066E-05	3.0710E-05	-3.4614E-03	4.0708E-05	-2.0317E-04	3.5751E-05	-1.2093E+02
Diff.	-0.10%	0.04%	-3.97%	-1.14%	-0.11%	-11.02%	-3.09%	-1.34%	-3.70%
					SA-Guide Tube				
MPB	-3.9239E-02	-9.9764E-02	-7.3735E-05	1.9662E-05	-3.4488E-03	3.5903E-05	-1.9662E-04	3.3347E-05	-1.1360E+02
SCB	-3.9279E-02	-9.9724E-02	-7.6669E-05	2.0047E-05	-3.4524E-03	4.0362E-05	-2.0288E-04	3.3849E-05	-1.1787E+02
Diff.	-0.10%	0.04%	-3.83%	-1.92%	-0.11%	-11.05%	-3.08%	-1.48%	-3.76%
					LZC-3S2F Outer/Scavenger/Feeder Tubes				
MPB	-1.1230E-02	-8.0817E-03	-6.6342E-07	2.3611E-04	-1.8466E-04	-5.8804E-08	-6.8344E-06	3.6229E-05	-4.7858E+01
SCB	-1.1241E-02	-8.0854E-03	-1.3575E-06	2.3560E-04	-1.8470E-04	2.4311E-07	-7.0826E-06	3.6009E-05	-4.8281E+01
Diff.	-0.10%	-0.05%	-51.13%	0.22%	-0.02%	-124.19%	-3.50%	0.61%	-0.88%
					LZC-2S1F Outer/Scavenger/Feeder Tubes				
MPB	-1.3610E-02	-1.8686E-02	-1.3685E-05	1.5864E-04	-4.6196E-04	-6.2042E-09	-1.7882E-05	4.1720E-05	-3.5187E+01
SCB	-1.3623E-02	-1.8686E-02	-1.4476E-05	1.5809E-04	-4.6199E-04	3.7644E-07	-1.8421E-05	4.1403E-05	-3.5663E+01
Diff.	-0.09%	-0.00%	-5.46%	0.35%	-0.01%	-101.65%	-2.93%	0.77%	-1.35%
					LZC-1S0F Outer/Scavenger Tubes				
MPB	-1.6072E-02	-2.9209E-02	-2.7367E-05	8.2356E-05	-7.5050E-04	7.9465E-08	-2.9427E-05	4.8068E-05	-2.3033E+01
SCB	-1.6085E-02	-2.9206E-02	-2.8270E-05	8.1685E-05	-7.5049E-04	5.4848E-07	-3.0267E-05	4.7556E-05	-2.3577E+01
Diff.	-0.08%	0.01%	-3.19%	0.82%	0.00%	-85.51%	-2.78%	1.08%	-2.36%

5.4.3 Comparison of Incremental Cross Sections and Incremental Supercell

Reactivities Between Cluster Fuel Model Versus Annularized Fuel Model

Production supercell calculations have been customarily performed using the annularized fuel-bundle geometry [50] because three-dimensional transport calculations for the detailed model are computationally expensive. In this section, the reactivity device incremental cross sections and incremental supercell reactivities obtained using the annularized fuel-bundle model are compared with those obtained using the detailed fuel-bundle model. The modelling of the reactivity devices in this comparison is the same, namely concentric cylindrical representation is used to model AA and SA, and cluster geometry to model multiple feeders and scavenger tubes of the LZC.

Table 5-12, Table 5-13 and Table 5-14 present the incremental cross sections using the annularized fuel geometry at zero burnup for AA, SA and LZC, respectively. Results are consistent with results obtained using the detailed-geometry (cluster) model, in that for both fuel types, the calculated difference in incremental supercell reactivity between the MPB and SCB is less than 1.5% for all reactivity devices. Similar to when using the detailed, cluster, geometry, the highest reactivity difference for AA occurs for Type 3 whereby the incremental-reactivity difference is 2.48 mk (-1.3%). For SA, the difference is 11.23 mk (-1.1%). The highest difference for LZC occurs for Type 1S0F whereby the difference is 1.01 mk (-0.4%), a result similar to the one obtained using the detailed, cluster, geometry.

A comparison of the cluster geometry representation with the annularized representation for AA, SA and LZC is presented in Table 5-15, Table 5-16 and Table 5-17, respectively, where differences in the two-group homogenized incremental cross sections and incremental supercell reactivity are given in percentage difference, defined as (annularized geometry - cluster geometry)/cluster geometry ×100%.

Table 5-15 and Table 5-16 show that the supercell reactivity increments for AA and SA can differ substantially (reactivity difference is between 7.0% to 10.0% for AA and between 10.0% to 11.0% for SA) for the two geometric representations and these differences exist for both bundle types. For LZC, the supercell reactivity increments are closer (less than 1.0% difference) for the two geometric representations, as shown in Table 5-17.

The highest % reactivity-increment difference for AA is -9.1% for MBP and -9.6% for SCB, for SA is -10.4% for MPB and -11.0% for SCB, and for LZC is -0.4% for MPB and -0.6% for SCB. The negative sign of the % reactivity-increment difference between the two modeling choices indicates that the annularized representation of fuel pins underestimates the supercell reactivity increment, and hence the device reactivity worth, compared to that calculated by the cluster representation. The magnitude of the underestimation is highest for SA, which has the highest calculated supercell reactivity, following AA and then LZC.

Table 5-12: Annularized Model Adjuster Absorbers Homogenized Incremental Cross Sections at Zero Burnup

	$\Delta\Sigma_{tr1}$ (cm^{-1})	$\Delta\Sigma_{tr2}$ (cm^{-1})	$\Delta\Sigma_{a1}$ (cm^{-1})	$\Delta\Sigma_{a2}$ (cm^{-1})	$\Delta\Sigma_{s12}$ (cm^{-1})	$\Delta\Sigma_{s21}$ (cm^{-1})	$\Delta\nu\Sigma_{f1}$ (cm^{-1})	$\Delta\nu\Sigma_{f2}$ (cm^{-1})	$\Delta\rho$ (mk)
Type 1									
MPB	1.3029E-03	7.6349E-04	2.5462E-05	5.9316E-04	-3.6007E-05	6.8638E-06	-1.4135E-06	7.1864E-05	-1.2107E+02
SCB	1.3038E-03	7.5990E-04	2.5452E-05	5.9166E-04	-3.6278E-05	7.6954E-06	-1.4999E-06	7.1318E-05	-1.2266E+02
Diff.	-0.07%	0.47%	0.04%	0.25%	-0.75%	-10.81%	-5.76%	0.77%	-1.29%
Type 2									
MPB	1.0599E-03	6.1790E-04	2.0722E-05	4.8447E-04	-2.9268E-05	5.6003E-06	-1.1560E-06	5.9312E-05	-9.9136E+01
SCB	1.0607E-03	6.1490E-04	2.0714E-05	4.8324E-04	-2.9493E-05	6.2802E-06	-1.2268E-06	5.8860E-05	-1.0044E+02
Diff.	-0.07%	0.49%	0.04%	0.25%	-0.76%	-10.83%	-5.78%	0.77%	-1.30%
Type 3									
MPB	2.4617E-03	1.2973E-03	4.7449E-05	9.5111E-04	-6.9530E-05	1.1240E-05	-2.4663E-06	1.1911E-04	-1.9184E+02
SCB	2.4635E-03	1.2914E-03	4.7423E-05	9.4870E-04	-6.9948E-05	1.2582E-05	-2.6104E-06	1.1819E-04	-1.9432E+02
Diff.	-0.07%	0.45%	0.06%	0.25%	-0.60%	-10.67%	-5.52%	0.78%	-1.28%
Type 4									
MPB	1.9666E-03	1.0970E-03	3.8184E-05	8.2519E-04	-5.4988E-05	9.6540E-06	-2.0460E-06	1.0143E-04	-1.6714E+02
SCB	1.9679E-03	1.0920E-03	3.8165E-05	8.2310E-04	-5.5353E-05	1.0814E-05	-2.1683E-06	1.0065E-04	-1.6931E+02
Diff.	-0.07%	0.46%	0.05%	0.25%	-0.66%	-10.73%	-5.64%	0.77%	-1.28%
Type 5									
MPB	7.0018E-04	4.2107E-04	1.3744E-05	3.3803E-04	-1.9164E-05	3.8816E-06	-7.8721E-07	4.1032E-05	-6.9513E+01
SCB	7.0065E-04	4.1914E-04	1.3739E-05	3.3715E-04	-1.9329E-05	4.3543E-06	-8.3535E-07	4.0692E-05	-7.0437E+01
Diff.	-0.07%	0.46%	0.04%	0.26%	-0.85%	-10.86%	-5.76%	0.84%	-1.31%
Type 6									
MPB	1.076E-03	6.257E-04	2.104E-05	4.899E-04	-2.974E-05	5.666E-06	-1.1715E-06	6.0053E-05	-1.0023E+02
SCB	1.077E-03	6.227E-04	2.103E-05	4.887E-04	-2.997E-05	6.354E-06	-1.2432E-06	5.9594E-05	-1.0155E+02
Diff.	-0.07%	0.49%	0.04%	0.25%	-0.76%	-10.82%	-5.77%	0.77%	-1.30%

Table 5-13: Annularized Model Shutoff Absorber Homogenized Incremental Cross Sections at Zero Burnup

	$\Delta\Sigma_{tr1}$ (cm^{-1})	$\Delta\Sigma_{tr2}$ (cm^{-1})	$\Delta\Sigma_{a1}$ (cm^{-1})	$\Delta\Sigma_{a2}$ (cm^{-1})	$\Delta\Sigma_{s12}$ (cm^{-1})	$\Delta\Sigma_{s21}$ (cm^{-1})	$\Delta\nu\Sigma_{f1}$ (cm^{-1})	$\Delta\nu\Sigma_{f2}$ (cm^{-1})	$\Delta\rho$ (mk)
MPB	1.5864E-03	-2.2761E-03	7.0239E-05	6.1912E-03	-5.6377E-05	6.4630E-05	-7.4331E-06	6.9041E-04	-1.0315E+03
SCB	1.5871E-03	-2.2968E-03	7.0362E-05	6.1796E-03	-5.7901E-05	7.3147E-05	-7.9601E-06	6.8550E-04	-1.0427E+03
Diff.	-0.04%	-0.90%	-0.18%	0.19%	-2.63%	-11.64%	-6.62%	0.72%	-1.08%

Table 5-14: Annularized Model Liquid Zone Controllers Homogenized Incremental Cross Sections at Zero Burnup

	$\Delta\Sigma_{tr1}$ (cm^{-1})	$\Delta\Sigma_{tr2}$ (cm^{-1})	$\Delta\Sigma_{a1}$ (cm^{-1})	$\Delta\Sigma_{a2}$ (cm^{-1})	$\Delta\Sigma_{s12}$ (cm^{-1})	$\Delta\Sigma_{s21}$ (cm^{-1})	$\Delta\nu\Sigma_{f1}$ (cm^{-1})	$\Delta\nu\Sigma_{f2}$ (cm^{-1})	$\Delta\rho$ (mk)
					Type 3S2F				
MPB	1.7558E-02	1.4946E-01	1.0038E-04	1.0713E-03	2.1025E-03	2.7919E-06	8.4457E-05	1.0231E-05	-1.9973E+02
SCB	1.7584E-02	1.4910E-01	1.0207E-04	1.0689E-03	2.1039E-03	2.6419E-06	8.7423E-05	1.0869E-05	-2.0065E+02
Diff.	-0.15%	0.24%	-1.66%	0.23%	-0.07%	5.68%	-3.39%	-5.86%	-0.46%
					Type 2S1F				
MPB	2.0227E-02	1.6713E-01	1.1525E-04	1.1962E-03	2.4230E-03	3.0549E-06	9.7158E-05	1.1292E-05	-2.2135E+02
SCB	2.0255E-02	1.6675E-01	1.1714E-04	1.1936E-03	2.4245E-03	2.8481E-06	1.0057E-04	1.1928E-05	-2.2236E+02
Diff.	-0.14%	0.23%	-1.61%	0.22%	-0.06%	7.26%	-3.40%	-5.33%	-0.45%
					Type 1S0F				
MPB	2.2965E-02	1.8447E-01	1.3075E-04	1.3185E-03	2.7528E-03	3.2917E-06	1.1028E-04	1.1874E-05	-2.4211E+02
SCB	2.2995E-02	1.8405E-01	1.3286E-04	1.3156E-03	2.7544E-03	3.0212E-06	1.1416E-04	1.2710E-05	-2.4312E+02
Diff.	-0.13%	0.23%	-1.59%	0.22%	-0.06%	8.95%	-3.39%	-6.58%	-0.41%

Table 5-15: Cluster versus Annularized Homogenized Incremental Cross Sections for Adjuster Rods at Zero Burnup

	Type 1	**Type 2**	**Type 3**	**Type4**	**Type 6**	**Type 6**
% Differences for MPB						
$\Delta\Sigma_{tr1}$	-15.03	-15.11	-15.05	-15.03	-15.10	-15.12
$\Delta\Sigma_{tr2}$	-46.69	-46.90	-46.57	-46.57	-47.05	-46.89
$\Delta\Sigma_{a1}$	-0.88	-1.02	-1.09	-0.96	-0.98	-1.03
$\Delta\Sigma_{a2}$	5.68	5.86	4.29	4.94	6.34	5.83
$\Delta\Sigma_{s12}$	38.41	37.83	39.59	39.14	37.22	37.84
$\Delta\Sigma_{s21}$	-27.21	-27.08	-28.08	-27.69	-26.76	-27.10
$\Delta\nu\Sigma_{f1}$	72.31	72.84	75.58	73.64	72.25	72.92
$\Delta\nu\Sigma_{f2}$	36.05	36.24	33.39	34.59	37.21	36.17
$\Delta\rho$	-7.54	-7.37	-9.12	-8.38	-6.82	-7.40
% Differences for SCB						
$\Delta\Sigma_{tr1}$	-14.97	-15.06	-15.00	-14.98	-15.05	-15.07
$\Delta\Sigma_{tr2}$	-46.84	-47.05	-46.72	-46.72	-47.19	-47.05
$\Delta\Sigma_{a1}$	-0.48	-0.62	-0.73	-0.57	-0.58	-0.63
$\Delta\Sigma_{a2}$	5.71	5.89	4.31	4.97	6.37	5.86
$\Delta\Sigma_{s12}$	38.65	38.07	39.82	39.36	37.52	38.09
$\Delta\Sigma_{s21}$	-27.51	-27.38	-28.37	-27.97	-27.09	-27.40
$\Delta\nu\Sigma_{f1}$	54.16	54.49	57.83	55.80	53.41	54.59
$\Delta\nu\Sigma_{f2}$	36.49	36.64	33.73	35.03	37.46	36.58
$\Delta\rho$	-8.05	-7.89	-9.63	-8.89	-7.34	-7.92

Table 5-16: Cluster versus Annularized Homogenized Incremental Cross Sections for Shutoff Absorber at Zero Burnup

	% Differences for MPB	**% Differences for SCB**
$\Delta\Sigma_{tr1}$	-16.23	-15.98
$\Delta\Sigma_{tr2}$	-281.50	-284.97
$\Delta\Sigma_{a1}$	2.63	3.50
$\Delta\Sigma_{a2}$	-0.15	-0.17
$\Delta\Sigma_{s12}$	14.05	14.72
$\Delta\Sigma_{s21}$	-30.62	-31.05
$\Delta\nu\Sigma_{f1}$	48.02	26.86
$\Delta\nu\Sigma_{f2}$	22.24	22.61
$\Delta\rho$	-10.42	-10.97

Table 5-17: Cluster versus Annularized Homogenized Incremental Cross Sections for Liquid Zone Controllers at Zero Burnup

	3S2F	2S1F	1S0F	3S2F	2S1F	1S0F
	% Differences for MPB			% Differences for SCB		
$\Delta\Sigma_{tr1}$	0.04	0.03	0.03	0.02	0.02	0.02
$\Delta\Sigma_{tr2}$	0.14	0.14	0.14	0.18	0.18	0.17
$\Delta\Sigma_{a1}$	0.19	0.16	0.12	0.35	0.31	0.27
$\Delta\Sigma_{a2}$	0.10	0.10	0.10	0.13	0.12	0.12
$\Delta\Sigma_{s12}$	0.06	0.06	0.06	0.05	0.05	0.05
$\Delta\Sigma_{s21}$	-1.27	-1.28	-1.32	-2.27	-2.45	-2.63
$\Delta\nu\Sigma_{f1}$	-1.04	-1.05	-1.05	-0.58	-0.60	-0.61
$\Delta\nu\Sigma_{f2}$	-7.83	-7.32	-7.49	-9.42	-9.70	-9.88
$\Delta\rho$	-0.34	-0.36	-0.38	-0.56	-0.58	-0.61

5.5   Conclusions

Results show that the incremental macroscopic cross sections of CANDU reactivity devices are very similar for MPB and SCB designs. Maximum differences in reactivity-device supercell reactivity increments, and hence in device reactivity worth, are less than 2% for any given device at zero burnup and less than 1.5% at 20-day burnup. Consequently, these differences have no operational implication. While a 2% across-the board reactivity-device difference might be thought to have some impact on the achievable burnup, it is noteworthy that only four MPBs by three or four fuel channels are expected to be in the core at any given time (as will be discussed in Chapter 6) and, therefore, only a small number of reactivity devices will have their reactivity worth altered by their proximity to an MPB. As a result, the difference in the overall core reactivity will be negligible and no discernible effect on the achievable burnup is expected. It is therefore concluded that the use of up to 12 or 16 MPBs in a CANDU core is entirely compatible with the current reactivity devices

and it is anticipated that no changes to reactivity devices will be necessary to allow

the use of MPBs.

Results also show that the use of the annularized bundle geometry to calculate

reactivity-device incremental cross-sections underestimates the supercell reactivity

increment and hence the device reactivity worth. Consequently, the use of the

annularized model is conservative. However, for a more accurate core reactivity

calculation especially during fast transients, a detailed, cluster, representation of the

bundle is recommended.

Chapter 6: Refuelling Considerations for Molybdenum Producing Bundle

For MPBs, an irradiation period of approximately 20 days is sufficient to reach the maximum attainable activity of ^{99}Mo in the enriched outer region of the fuel pins. If MPBs are to be employed in a CANDU reactor, departure from the standard fuelling scheme will be unavoidable for one or more fuel channels in the core. In this chapter, a modified fuelling scheme is developed that is suitable for the purpose of irradiating MPBs in the core and harvesting of ^{99}Mo thereafter. The modified fuelling scheme is assessed by performing full-core time-average calculations.

The MPB has been shown to produce approximately 4000 six-day Curies of ^{99}Mo activity per bundle when irradiated in the peak-power channel of a CANDU reactor [3]. Accounting for the lower channel flux away from the core center, a production rate of ~4 bundles per week is estimated to meet the global demand of ^{99}Mo, which is estimated to be 12,000 six-day Curies as noted in Section 2.2.

6.1 Fuelling Scheme for Channels Containing MPB

The horizontal cylindrical vessel of a CANDU reactor contains 380 horizontal fuel channels placed on a square lattice pitch of 28.575 cm. Each channel holds 12 fuel bundles that are 49.53 cm in length. Coolant flows in opposite directions in adjacent channels, in a checkerboard pattern. Refuelling of a channel is carried out by 2 fuelling

machines that are attached to each end of the channel. The insertion of fresh bundles

is performed in the coolant flow direction, where one of the fuelling machines pushes

fresh fuel bundles in the channel while the other fuelling machine recovers irradiated

bundles. Usually, eight bundles are replaced in a refuelling operation known as an

8-bundle shift.

In the modified fuelling scheme proposed herein, an *MPB-fuelled* channel does

not contain just MPBs, but rather contains 4 MPBs and 8 SCBs. The MPBs occupy the

4 positions in the middle of the channel (5-8) and the SCBs occupy the inlet 4 positions

(1-4) and outlet 4 positions (9-12). The 8-bundle shift refuelling procedure for an

MPB-fuelled channel using 4 MPBs and 4 SCBs is depicted in Figure 6-1. MPBs

removed from the channel (positions 5-8) are sent for ^{99}Mo harvesting, while SCBs

removed from the channel (positions 9-12), which have not reached their discharge

burnup limit, can be either discharged or reloaded into the core. This work assumes

that the SCBs removed from the channel are discharged.
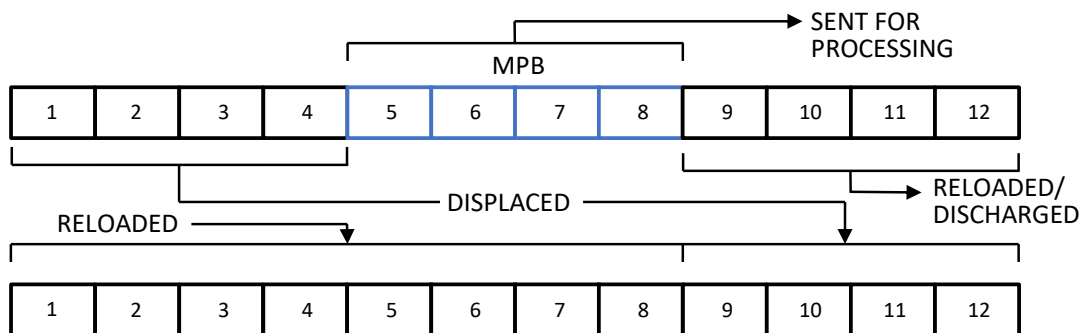
Figure 6-1: CANDU 8-bundle shift scheme incorporating MPBs

6.2 MPB Channel Pools

For a core refuelled exclusively with SCBs, a channel is refuelled, on average, every 180 full-power days, which corresponds to approximately two channels being refuelled each day. In other words, the dwell time for an *SCB-fuelled* channel is T_{SCB}=180 days. For MPBs, a 20-day irradiation time is sufficient to reach the maximum attainable activity of ^{99}Mo in the fuel pins. Consequently, for an *MPB-fuelled* channel, the dwell time is T_{MPB}=20 days. If a given channel was refuelled with MPBs at every refuelling operation, its refuelling frequency would be nine times higher than the average refuelling frequency, which would result in excessive wear and tear on the channel end fittings. To avoid excessive wear and tear from frequent refuelling, MPB fuelling can be rotated among channels in a pool designated for MPB production. The larger the number of channels in the pool, the less frequent a channel's turn to be refuelled using MPBs will be, and the smaller the increase in its average refuelling frequency. If every channel in the pool undergoes a cycle consisting of one MPB refuelling followed by n SCB refuellings, its average refuelling frequency, $\overline{R}$, will be:

$$\overline{R} = \frac{n+1}{nT_{SCB} + T_{MPB}}$$

(6.1)

After a channel in the pool has gone through one MPB refuelling, it will experience n SCB refuellings before it can be refuelled with MPB again. Therefore, the total length of the cycle for a subsequent MPB refuelling, which is T_{MPB} multiplied by

the number of channels in the pool, N_p, is larger than (or at least equal to) the channel refuelling cycle. That is:

$$T_{MPB}N_p \geq T_{MPB} + nT_{SCB} \tag{6.2}$$

The minimum number of channels in the pool, N_p, can be calculated as:

$$N_p = 1 + n\frac{T_{SCB}}{T_{MPB}} \tag{6.3}$$

At any given time, one and only one channel in the pool will contain MPBs. If, at any given time, more than one channel needs to contain MPBs, then more than one MPB refuelling pool is necessary.

This work aims to have the refuelling frequency increased by no more than 25% compared to the usual refuelling frequency for SCBs, that is:

$$\overline{R} \times T_{SCB} < 1.25 \tag{6.4}$$

Consequently, for each channel, the number of SCB refuelling operations separating MPB refuelling operations has to satisfy:

$$\frac{n+1}{nT_{SCB} + T_{MPB}} \times T_{SCB} < 1.25 \tag{6.5}$$

That target of 25% increase in the refuelling frequency is based on best judgement, rather than on empirical data or operational experiences from refuelling activities at CANDU stations. It can be easily verified that the lowest integer value to satisfy inequality (6.5) is $n=4$, which corresponds to a 22% increase in the average refuelling rate. Therefore, the minimum number of channels in the pool is:

$$N_p = 1 + 4\frac{180d}{20d} = 37 \qquad\qquad\qquad (6.6)$$

Because, on average, 4 MPBs need to be discharged per week to satisfy the world demand of ^{99}Mo, approximately 12 MPBs need to be discharged every T_{MPB}=20 days, which means that three channels in the core need to irradiate MPBs at any given time. Consequently, three 37-channel pools need to be set up for the MPB refuelling operation. At any given time, one channel in each pool will contain 4 MPBs in the center and all other channels will contain only SCBs.

Figure 6-2 displays one possible arrangement, which has four 37-channel MPB-refuelling pools and the selection of channels inside the core is performed in a symmetrical manner. Of the 4 channel pools, only three will be active. As can be seen from Figure 6-2, the channels designated for MPB production are located in the inner region of the core and hence are exposed to a high neutron flux. Efforts are made, as much as possible, to prevent loading of MPBs in two adjacent channels while, at the same time, ensuring that the MPB channel pools are located in the inner burnup region.

It is noteworthy that the 4th pool of 37 channels may be used to increase the supply of molybdenum in the future or be utilized as a backup to further reduce the strain caused by increased frequency of fuelling for an active pool by switching the MPB production from an active pool to the back-up pool. These possibilities are not investigated in this work.

	1	2	3	4	5	6	7	8	9	10	11	12	13	14	15	16	17	18	19	20	21	22
A									***	***	***	***	***	***								
B						***	***	***	***	***	***	***	***	***	***	***	***					
C					***	***	***	***	***	***	***	***	***	***	***	***	***	***				
D				***	***	***	***	***	***	***	***	***	***	***	***	***	***	***	***			
E			***	***	***	***	***	1	2	3	4	4	3	2	1	***	***	***	***	***		
F			***	***	***	10	9	8	7	6	5	5	6	7	8	9	10	***	***	***		
G		***	***	***	***	11	12	13	14	15	16	16	15	14	13	12	11	***	***	***	***	
H		***	***	***	22	21	20	19	18	17			17	18	19	20	21	22	***	***	***	
J	***	***	***	***	23	24	25	26	27	28			28	27	26	25	24	23	***	***	***	***
K	***	***	***	***	34	33	32	31	30	29			29	30	31	32	33	34	***	***	***	***
L	***	***	***	***	35	36	37									37	36	35	***	***	***	***
M	***	***	***	***	35	36	37									37	36	35	***	***	***	***
N	***	***	***	***	34	33	32	31	30	29			29	30	31	32	33	34	***	***	***	***
O	***	***	***	***	23	24	25	26	27	28			28	27	26	25	24	23	***	***	***	***
P		***	***	***	22	21	20	19	18	17			17	18	19	20	21	22	***	***	***	
Q		***	***	***	***	11	12	13	14	15	16	16	15	14	13	12	11	***	***	***	***	
R			***	***	***	10	9	8	7	6	5	5	6	7	8	9	10	***	***	***		
S			***	***	***	***	***	1	2	3	4	4	3	2	1	***	***	***	***	***		
T				***	***	***	***	***	***	***	***	***	***	***	***	***	***	***	***			
U					***	***	***	***	***	***	***	***	***	***	***	***	***	***				
V						***	***	***	***	***	***	***	***	***	***	***	***	***				
W									***	***	***	***	***	***								

Figure 6-2: Four 37-channel pools for molybdenum production

6.3 Diffusion Code and Time-average Calculations

The general effects of MPB loading in some of the channels can be studied using a *time-average* core calculation. Such a calculation determines the *time-average* value of the core reactivity, as well as time-average values of burnup, macroscopic cross sections, neutron flux and power for each bundle position, based on the fuel type, refuelling scheme and prescribed discharge burnup for each fuel channel.

A time-average calculation assumes that each fuel channel is always refuelled with the same fuel combination and at the same time interval, equal to the dwell time for that channel. Such a calculation is well suited for studying a configuration whereby

three channels in the core are always fuelled with MPBs every 20 days, while all the other channels are refuelled exclusively with SCBs at channel-specific time intervals which average approximately 180 days. The time-average calculation is unable to directly model the rotation of the MPB-bearing channels among the 37-channels in each MPB pool. However, if operational limits are not exceeded when any of the 37 channels is refuelled continuously with MPBs, it can be inferred that rotating the MPB-bearing channel among the channels in the pool will not cause operational limits to be exceeded either.

The neutron diffusion code DONJON ver. 5 [79] is used to perform time-average calculations. The core model used in this study utilizes burnup-dependent bare-lattice two-group homogenized cross sections and reactivity device incremental cross sections from Chapter 5, which were obtained using the lattice code DRAGON.

The time-average calculation is performed considering the bidirectional nature of the refuelling scheme of CANDU and assuming that all channels employ the 8-bundle shift refuelling scheme. The core is divided into two separate burnup regions: outer and inner. The boundary of the inner region coincides with the combined outer boundary of the four MPB producing channel pools as shown in Figure 6-2. The exit burnups used in the time-average simulations are provided in Table 6-1. The flux is normalized to a total reactor power of 2,061 MW.

In addition to specifying the fuel type, the time-average calculation has two main free variables that need to be provided by the user, namely the refuelling scheme and the target exit burnup of each fuel channel. When the target exit burnups

are provided for each fuel channel, the exact burnup integration limits for each fuel

bundle are unknown and need to be determined. The burnup integration limits are a

function of the normalized axial power shape which depends on the flux solution over

the reactor core. Moreover, the flux solution depends on the fuel properties, which in

turns depends on the burnup integration limits for each fuel bundle. Consequently,

the time-average calculation is an iterative process of repeating steps required for the

axial power shape computation. The process is repeated until the relative error

between two successive axial power shape calculations is smaller than a

user-specified value. In this case, a convergence limit of 1.0×10^{-4} is used. A flow chart

of the DONJON iterative calculations for time-average simulations is shown in Figure

6-3.

The reference time-average calculation scheme is repeated many times while

adjusting the exit burnups and liquid zone controller levels until an acceptable

effective multiplication factor and power profile are achieved.

Table 6-1: Exit Burnups for Different Core Regions

Region	Burnup [MWd/t(U)]
Inner	7,806
Outer	7,253
MPB Channels	1,125[†]

[†] Exit burnup of MPB channels is selected to ensure the average burnup of MPBs at positions 5-8 are as close as possible to 906.62 MWd/t(U)
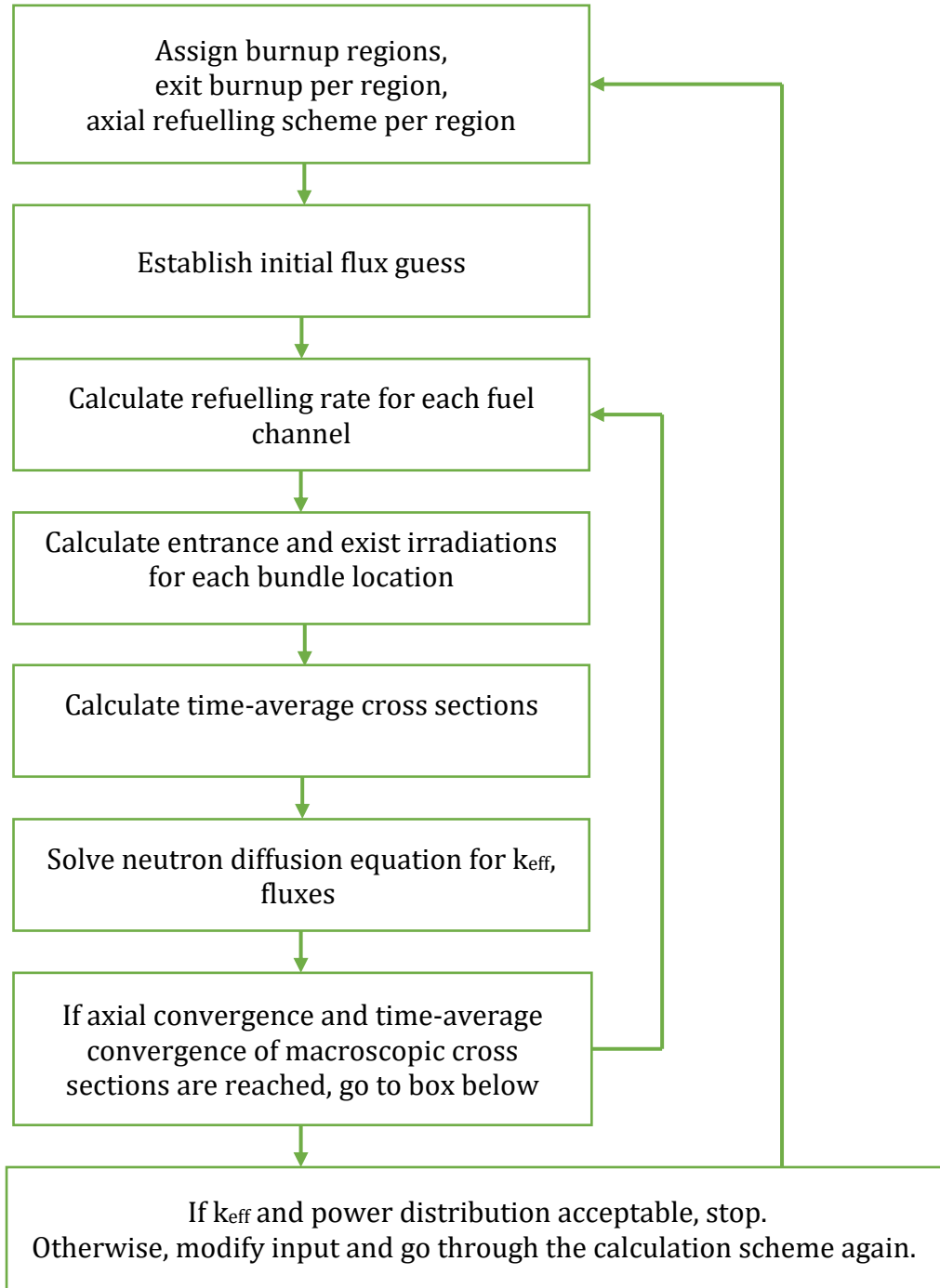
Figure 6-3: Flow chart of iterative scheme for time average calculations

6.4 Results and Interpretation

An initial time-average simulation is done for a CANDU core fuelled entirely with SCBs to establish a reference. The effective multiplication factor for the reference core is calculated to be 1.00001. The corresponding time-average properties for a core in which, at any given time, 3 channels (one in each pool) contain a set of 4 MPBs, depends on which specific channels contain these bundles.

Figure 6-4 shows the core effective multiplication factor for the reference core and for the time-average simulation as a function of the position of the MPB-bearing channel in each of the three pools. In addition to the reference case, a total of 37 time-average simulations are performed where 4 MPBs are placed in positions 5-8, in series, starting from pool-channel # 1 and ending with #37 for MPB channel pools 1, 2 and 3, as depicted in Figure 6-2. Additional results for these 37 time-average simulations are recorded in Table 6-2, which includes the overall core reactivity and the core average exit burnup.

As can be seen from Table 6-2, a slight increase in the core reactivity is observed, which is due to the higher refuelling frequency in the three MPB-bearing channels. The magnitude of the reactivity increases when averaged over the 37 positions in the 3 MPB pools is 0.31 mk, which can be easily compensated by the zone-control units. The core-average exit burnup is decreased slightly due to the short residence time for MPB-bearing channels. The reference core-average exit burnup is 7,517 MWd/t(U), whereas the value of the core-average exit burnup averaged over the 37 time-average simulations is 7142 MWd/t(U), which is a relative decrease of 5.0%. It is noteworthy

that the increase in reactivity mentioned earlier and the decrease in the core-average exit burnup can be completely eliminated by increasing the discharge burnup values in all SCB-fuelled channels.

A sensitivity study is performed where the target burnup values are increased 0.65% from those listed in Table 6-1 to 7,856 MWd/t(U) for the inner region and 7,301 MWd/t(U) for the outer region. The target burnup for MPB-bearing channels is not modified in this case. Figure 6-5 shows the core effective multiplication factor as a function of the position of the MPB-bearing channel in each of the three pools for the sensitivity case. As can be seen from Figure 6-5, the reduction in core reactivity is achievable by increasing the discharge burnup values in SCB-fuelled channels in the core, thus also improving slightly the fuel utilization in the reactor.

Table 6-2: Time-average Results for Reference Case and 37 Time-average Simulations Employing 4 MPBs per Three Selected Channels

Case #	K$_{eff}$	Reactivity (mk)	Core Avg. Exit Burnup [MWd/t(U)]
Reference	1.00001	0	7,517
1	1.00038	0.37	7,107
2	1.00037	0.37	7,107
3	1.00036	0.36	7,112
4	1.00035	0.34	7,123
5	1.00030	0.29	7,149
6	1.00031	0.30	7,144
7	1.00032	0.32	7,135
8	1.00035	0.35	7,119
9	1.00036	0.35	7,118
10	1.00035	0.34	7,129
11	1.00036	0.35	7,119
12	1.00035	0.34	7,120
13	1.00034	0.33	7,129
14	1.00030	0.30	7,151
15	1.00029	0.28	7,161
16	1.00029	0.28	7,158
17	1.00027	0.27	7,173
18	1.00029	0.28	7,164
19	1.00031	0.31	7,143
20	1.00034	0.33	7,129
21	1.00036	0.35	7,118
22	1.00037	0.36	7,116
23	1.00035	0.35	7,122
24	1.00033	0.32	7,133
25	1.00030	0.29	7,148
26	1.00029	0.28	7,162
27	1.00027	0.26	7,177
28	1.00026	0.25	7,183
29	1.00025	0.24	7,189
30	1.00026	0.25	7,184
31	1.00027	0.27	7,171
32	1.00029	0.28	7,158
33	1.00030	0.29	7,146
34	1.00033	0.32	7,130
35	1.00035	0.34	7,118
36	1.00032	0.31	7,138

37	1.00029	0.28	7,156
Average		**0.31**	**7142**
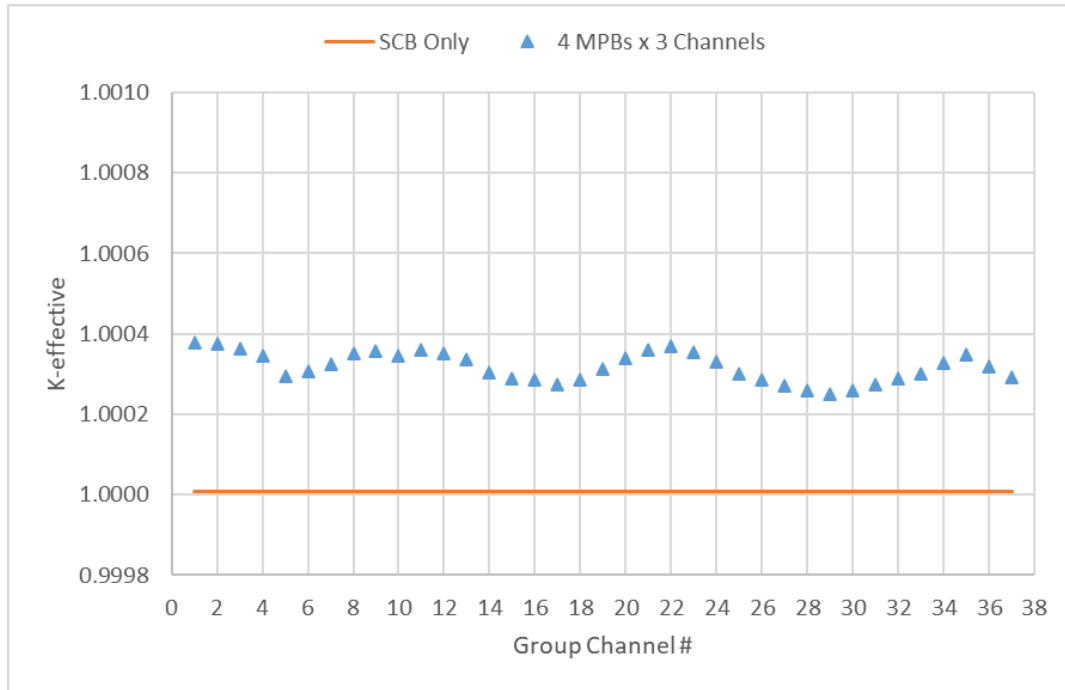
Figure 6-4: Core effective multiplication factor for reference case and 37 time-average simulations

The largest change in core reactivity for the reference time-average simulations (Table 6-2) is seen for Case 1 whereby 4 MPBs are loaded inside channel position 1 in each of the 3 MPB channel pools, namely channels E8, E15 and S8. Figure 6-6 shows a comparison of the channel powers for a core fuelled with SCBs only and for Case 1.

As can be seen in Figure 6-6, the maximum increase in channel power is 8.3 %, which is not expected to create any fuelling related operational difficulties as it is within the limits of channel power increase immediately following standard refuelling.

171
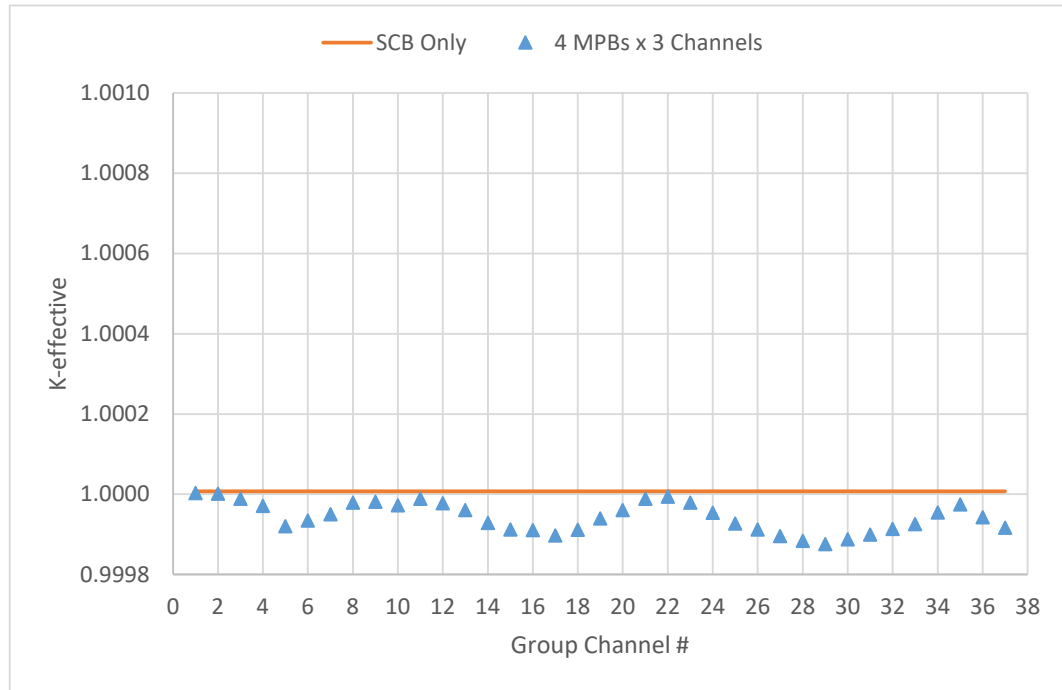
Figure 6-5: Core effective multiplication factor for reference case and 37 time-average simulations with 0.65% increase in target burnups for inner and outer regions

The prescribed fuelling scheme proposes that MPBs will occupy the 4 positions in the middle of the active MPB-bearing channel (bundle position 5-8). The average bundle power for these centrally positioned bundles in the 4 MPB channel pools is determined to be 655 kW. The ^{99}Mo yield for MPB bundles being irradiated in the inner region of the core is proportional to the bundle power. At a rated bundle power of 655 kW it is calculated to be 2,970 six-day Curies. This means that at a production rate of 4 MPB bundles per week, the proposed refuelling scheme will produce approximately 11,880 six-day Curies per week, which is very close to the global demand of 12,000 six-day Curies per week [6].

	1	2	3	4	5	6	7	8	9	10	11
A									3579	3742	3791
B						3303	3986	4527	4804	4963	4963
C					3715	4421	5101	5563	5814	5885	5804
D				3890	4666	5382	5960	6283	6394	6335	6116
E			3755	4713	5477	6046	6430	6523	6444	6262	5936
F			4538	5430	6033	6355	6453	6363	6018	5775	5553
G		4057	5105	5923	6332	6461	6387	6173	5750	5520	5453
H		4561	5557	6197	6331	6328	6169	5920	5521	5326	5306
J	3679	4899	5854	6298	6091	5939	5772	5561	5299	5156	5142
K	3928	5168	6053	6365	5927	5687	5568	5377	5161	5045	5039
L	4086	5317	6186	6493	6130	5848	5575	5336	5117	5007	5004

	1	2	3	4	5	6	7	8	9	10	11
A									3700	3863	3910
B						3409	4124	4689	4971	5128	5121
C					3818	4563	5287	5782	6029	6086	5991
D				3972	4786	5554	6195	6583	6654	6558	6312
E			3807	4795	5601	6227	6706	7064	6734	6479	6117
F			4582	5501	6139	6504	6655	6619	6225	5942	5696
G		4072	5135	5974	6409	6568	6522	6326	5887	5638	5558
H		4562	5567	6223	6375	6393	6250	6009	5603	5400	5372
J	3666	4885	5844	6298	6105	5966	5809	5603	5340	5191	5172
K	3905	5140	6026	6343	5915	5684	5572	5385	5169	5049	5037
L	4055	5277	6144	6454	6099	5824	5557	5321	5101	4987	4978

	1	2	3	4	5	6	7	8	9	10	11
A									3.4%	3.2%	3.1%
B						3.2%	3.5%	3.6%	3.5%	3.3%	3.2%
C					2.8%	3.2%	3.7%	3.9%	3.7%	3.4%	3.2%
D				2.1%	2.6%	3.2%	3.9%	4.8%	4.1%	3.5%	3.2%
E			1.4%	1.7%	2.3%	3.0%	4.3%	8.3%	4.5%	3.5%	3.1%
F			1.0%	1.3%	1.8%	2.4%	3.1%	4.0%	3.4%	2.9%	2.6%
G		0.4%	0.6%	0.9%	1.2%	1.7%	2.1%	2.5%	2.4%	2.1%	1.9%
H		0.0%	0.2%	0.4%	0.7%	1.0%	1.3%	1.5%	1.5%	1.4%	1.2%
J	-0.4%	-0.3%	-0.2%	0.0%	0.2%	0.4%	0.6%	0.8%	0.8%	0.7%	0.6%
K	-0.6%	-0.5%	-0.5%	-0.3%	-0.2%	0.0%	0.1%	0.2%	0.2%	0.1%	0.0%
L	-0.8%	-0.7%	-0.7%	-0.6%	-0.5%	-0.4%	-0.3%	-0.3%	-0.3%	-0.4%	-0.5%

Figure 6-6: Quarter-core view of reference channel powers (top), quarter-core view of position 1 (Ch. E8) fuelled with 4 MPBs (middle), and percent channel-power differences (bottom)

6.5 Conclusions

The work documented in this chapter demonstrates that the shorter dwell time required by MPBs (20 days) can be accommodated without inducing excessive wear and tear to channel end fittings by rotating the MPB-bearing channels within three pools of 37 channels located in the inner region of the core. A series of 37 time-average calculations when compared to the reference case with only SCBs, indicate that a slight increase in the core reactivity can be expected when 3 fuel channels containing a total of 12 MPBs and where the three MPB-bearing fuel channels are refuelled after roughly 20 days. The study also shows that reactivity increase in the core can be eliminated by slightly increasing the discharge burnup in the SCB channels.

These preliminary time-average calculations indicate that no major changes in the channel power map are to be expected from the use of MPBs. The case with the highest core reactivity change results in an 8.3% change in the maximum channel power as compared to the reference case, hence indicating that no fuelling related operational difficulties are to be expected as it is within the limits of channel power increase immediately following refuelling for SCB channels in the high-power region of the core.

The calculated ^{99}Mo yield corresponds to approximately the world weekly demand. A production rate of 4 bundles per week will be able to satisfy the global demand of ^{99}Mo. Overall, the proposed refuelling scheme ensures the feasibility of producing significant and continuous quantities of ^{99}Mo in a CANDU reactor. The

continuous and reliable supply of ^{99}Mo will ensure the availability of life saving

medical procedures for millions of patients around the globe.

Chapter 7:   Summary and Future Work

The research presented in this dissertation is composed of three main research segments. The integrated work presented herein and the precursor work documented in Reference [3] ensure the comprehensiveness of the research and support the development and neutronic assessment of the MPB in a manner consistent with standard industry practices.

The multi-phase analysis began with the design of the MPB composition and bundle geometry as presented in Reference [3] and, as presented in Chapter 4, assessment of single lattice reactivity feedback effects is performed for key reactor parameters and comparison of the results are made between the MPB and SCB. Since the preliminary assessment of the fuel pin radial temperatures in the two bundles were calculated to be significantly different, this work employed a detailed lattice model utilizing the variation in the radial fuel pin temperatures for more accurate predictions of the reactivity feedback. A first-of-a-kind application of the linear perturbation theory is applied to explain the small variation in the reactivity effects between the two bundles.

The key focus of the study was to assess whether the reactivity effects of the MPB and SCB are similar without necessarily assessing the magnitude of the reactivity feedback effects. The study presented in Chapter 4 is limited by the use of a single-cell two-dimensional model and by the fact that it does not address combined effects of possibly large perturbations occurring under specific transient scenarios.

However, the advantage of using individual parametric reactivity effects is that, as long as perturbations are small, arbitrary combined effects can be reconstructed by simply adding the individual effects.

Given that all individual reactivity effects are shown to be quasi-identical for the two bundles, any combined reactivity effect can also be expected to be quasi-identical (for small perturbations). This extends to perturbations where multiple parameters vary simultaneously, such as a power increase accompanied by fuel-temperature increase, coolant-temperature increase and average coolant density decrease due to partial boiling. Of course, if perturbations become large, reactivity effects will stop being additive and detailed calculations for the specific scenario under investigation (e.g., loss of coolant) need to be performed.

Showing that the single-parameter reactivity effects are very close is a first and necessary step in showing equivalence between the two bundles for transient conditions. To gain full confidence in the equivalence of the reactivity feedback effects in the two bundle types under transient scenarios, future work will have to include detailed, three-dimensional simulations of transients of interest, including the coupling between thermal-hydraulic and neutronic analyses.

Chapter 5 presented the incremental effects of CANDU reactivity devices on lattice properties which are determined to be very similar for MPB and SCB. A comparison of the detailed cluster representation of the fuel bundle and the reactivity devices was made with the standard annularized fuel bundle model that has been

used in the industry. The use of the standard model is determined to be conservative compared to the fully explicit supercell model.

For future work, it is recommended to perform transient analyses to ascertain the difference in transient simulation results between the case when cross-section increments are calculated using the standard annularized fuel-bundle geometry and the case when cross-section increments are calculated using a detailed, cluster, fuel-bundle geometry.

This work and its finding are based solely on 3D lattice calculations. The focus of the work is on reactivity-device increments, not on the actual reactivity worth of individual devices. Focusing on increments allows one to draw more general conclusions (i.e., covering, at least in principle, any reactivity device combination and any depth of insertion) than it is possible when analyzing individual reactivity-device worth. The study concludes that device reactivity worths are expected to be only marginally affected by the presence of MPBs because cross sections and supercell reactivity increments are only marginally affected by the presence of MPBs. Confirmatory full-core analyses are anticipated in the future to determine the actual reactivity worths and the effect the proximity of an MPB may have on individual reactivity devices.

The work of Chapter 6 involved developing a full-core 3D model using 2 neutron group properties with all relevant structures, devices and reactor core geometry. The full-core model used a detailed 3D representation of generic CANDU-6 reactor specifications. A suitable fuelling strategy is developed to achieve the desired weekly

yield of ^{99}Mo. The adequacy of the proposed refuelling scheme is evaluated using time-average properties.

In future work, the findings based on a time-average method will have to be confirmed by detailed, core-follow calculations, whereby the detailed sequence of channels being refuelled is simulated and where detailed bundle and channel power distributions are calculated for each resulting core configuration.

Future work will also have to include additional refuelling schemes, as well as fuel manufacturing and irradiated fuel processing aspects. This will ensure that ^{99}Mo can be safely and reliably produced in the MPB inside CANDU by maintaining a comparable operational envelope to a standard natural uranium fuelled configuration.

Chapter 8: References

[1] Ad Hoc Health Experts Working Group on Medical Isotopes, "Lessons Learned from the Shutdown of the Chalk River Reactor," 2008. [Online]. Available: https://www.canada.ca/content/dam/hc-sc/migration/hc-sc/hcs-sss/alt_formats/hpb-dgps/pdf/pubs/2008-med-isotope/2008-med-isotope-eng.pdf. [Accessed July 2022].

[2] International Atomic Energy Agency, "Manual for Reactor Produced Radioisotopes," IAEA-TECDOC-1340, Vienna, 2003.

[3] E. Nichita and J. Haroon, "Molybdenum-99-Producing 37-Element Fuel Bundle Neutronically and Thermal-Hydraulically Equivalent to a Standard CANDU fuel Bundle," *Nuclear Engineering and Design,* vol. 307, pp. 86-95, 2016.

[4] Korea Atomic Energy Research Institute, "Nuclear Data Center at KAERI," [Online]. Available: https://atom.kaeri.re.kr/. [Accessed August 2022].

[5] International Atomic Energy Agency, "Non-HEU Production Technologies for Molybdenum-99 and Technetium-99m, IAEA-No. NF-T-5.4," Vienna, 2013.

[6] OECD/NEA, "The Supply of Medical: An Economic Diagnosis and Possible Solutions," OECD Publishing, Paris, 2019.

[7] Committee on State of Molybdenum-99 Production and Utilization, et al., "Molybdenum-99 for Medical Imaging," Washington (DC): National Academies Press, 2016.

[8]   A. C. Morreale et al., "The Potential Production of Molybdenum 99 in CANDU Reactors," in *Proceedings of 32nd Annual Conference of the Canadian Nuclear Society*, Niagara Falls, 2011.

[9]   National Research Council, "Medical Isotope Production Without Highly Enriched Uranium," The National Academies Press, Washington (DC), 2009.

[10] World Nuclear Association, "Radioisotopes in Medicine," April 2022. [Online]. Available: https://world-nuclear.org/information-library/non-power-nuclear-applications/radioisotopes-research/radioisotopes-in-medicine.aspx. [Accessed August 2022].

[11] D. Banks, "Canada's Neutron Source, the NRU Reactor, Closes," *Neutron News,* vol. 29, no. 2, pp. 25-31, 2018.

[12] W. Forrest, "Can Nuclear Medicine Avoid Another Mo-99 Shortage?," 2019. [Online]. Available: https://physicsworld.com/a/can-nuclear-medicine-avoid-another-mo-99-shortage/. [Accessed August 2022].

[13] International Atomic Energy Agency, "Production and Supply of Molybdenum-99 (annex to the Nuclear Technology Review 2010)," IAEA, 2010. [Online]. Available: https://www.iaea.org/sites/default/files/gc/gc54inf-3-att7_en.pdf. [Accessed August 2022].

[14] International Atomic Energy Agency, "Research Reactor Database," [Online]. Available: http://nucleus.iaea.org/RRDB/RR/ReactorSearch.aspx?rf=1. [Accessed August 2022].

[15] S. C. van der Marck et al., "The Options for the Future Production of the Medical Isotope ^{99}Mo," *European Journal of Nuclear Medicine and Molecular Imaging,* vol. 37, no. 10, pp. 1817-1820, 2010.

[16] Report of the Task Force on Alternatives for Medical-Isotope Production, "Making Medical Isotopes," TRIUMF, Vancouver, 2008.

[17] A. Mushtaq, "Producing Radioisotopes in Power Reactors," *Journal of Radioanalytical and Nuclear Chemistry,* vol. 292, pp. 793-802, 2011.

[18] World Nuclear News, "Bruce Power, Isogen Look to Build on Radioisotope Success," 28 June 2022. [Online]. Available: https://www.world-nuclear-news.org/Articles/Bruce-Power,-Isogen-look-to-build-on-radioisotope. [Accessed August 2088].

[19] Canadian Nuclear Safety Commission, "Record of Decision," 26 October 2021. [Online].   Available: https://www.nuclearsafety.gc.ca/eng/the-commission/pdf/Decision-OPG-Mo-99-CMD21-H107-e.pdf.

[20] J. M. Cuttler, "Producing Molybdenum-99 in CANDU Reactors," in *Proceedings of 31st Annual Conference of the Canadian Nuclear Society*, Montreal, 2010.

[21] A. C. Morreale et al., "Strategy for Intensive Production of Molybdenum-99 Isotopes for Nuclear Medicine Using CANDU Reactors," *Applied Radiation and Isotopes,* vol. 70, pp. 20-34, 2012.

[22] Z. XingGuan et al., "Physics Codes and Methods for CANDU Reactor," Atomic Energy of Canada Limited, 1996.

[23] J. V. Donnelly et al., "Modelling of CANDU Reactivity Devices with WIMS-AECL/MULTICELL and Superhomogenization," in *Proceedings of the 17th Annual Canadian Nuclear Society conference*, Fredericton, 1996.

[24] A. Dimitar, "New Capabilities of the Lattice Code WIMS-AECL," in *International Conference on the Physics of Reactors 2008, PHYSOR 08*, Interlaken, 2008.

[25] G. Marleau et al., "A User Guide for DRAGON Release 3.06O," Ecole Polytechnique de Montreal, Montreal, 2016.

[26] KAERI, "Validation of WIMS-AECL Reactivity Device Calculation for CANDU Reactor," KAERI/TR-876/97, 1997.

[27] W. Shen et al., "Validation of DRAGON Side-Step Method for Bruce-A Restart Phase-B Physics Tests," in *25th Annual Conference of the Canadian Nuclear Society*, Toronto, 2004.

[28] A. Eckhardt et al., "Study of Local Fuel Temperature Distribution Effects Using Coupled Lattice Physics and Thermal Hydraulics Codes," in *37th Annual Conference of the Canadian Nuclear Society and 41st Annual CNS/CNA Student Conference*, Niagara Falls, 2017.

[29] M. H. M. Roshd, "The Physics of CANDU Reactor Design," in *American Nuclear Society Conference*, Toronto, 1976.

[30] D. S. Craig, "A Comparison of Lattice Parameters for CANDU-Type Lattices obtained using MCNP, WIMS, and WIMS with resonance Reaction Rates from MCNP," Atomic Energy of Canada Limited, Chalk River, 1989.

[31] H. Choi et al., "Temperature Effect of DUPIC Fuel in CANDU Reactor," Korea Atomic Energy Research Institute, 1997.

[32] K. S. Kozier, "Comparison of MCNP4B and WIMS-AECL Calculations of Coolant-Void-Reactivity Effects for Uniform Lattices of CANDU® Fuel," in *20th Annual Conference of the Canadian Nuclear Society*, Montreal, 1999.

[33] P. S. W. Chan et al., "Reactor Physics of NG CANDU," in *22nd Annual Conference of the Canadian Nuclear Society*, Toronto, 2001.

[34] J. Whitlock et al., "Effects Contributing to Positive Coolant Void Reactivity in CANDU," in *American Nuclear Society Annual Meeting*, Philadelphia, 1995.

[35] J. F. Valko et al., "Calculation of the Void Reactivity of CANDU Lattices Using the Scale Code System," *Annals of Nuclear Energy,* vol. 159, no. 2-3, pp. 225-231, 1995.

[36] F. Rahnema et al., "Void Reactivity Calculations in a Typical CANDU Cell Using MCNP and Helios," in *International Conference on the Physics of Nuclear Science and Technology*, Long Island, 1998.

[37] M. Constantin and V. Balaceanu, "Void Reactivity and Pin Power Calculation for a Typical CANDU Cell using CPs and a Two-Stratified Coolant Model," *Annals of Nuclear Energy,* vol. 29, no. 7, pp. 791-803, 2002.

[38] C. A. Cotton et al., "Coolant Void Reactivity Analysis of CANDU and ACR-700 Lattices," in *American Nuclear Society Annual Meeting*, Pittsburgh, 2004.

[39] J. Park et al., "Physics Study of Canada Deuterium Uranium Lattice with Coolant Void Reactivity Analysis," *Nuclear Engineering and Technology,* vol. 49, no. 1, pp. 6-16, 2016.

[40] G. Marleau et al., "New Computational Methods Used in the Lattice Code DRAGON," in *Topical Meeting on Advances in Reactor Physics*, Charleston, 1992.

[41] J. D. Irish et al., "Validation of WIMS-IST," in *23rd Annual Conference of the Canadian Nuclear Society*, Toronto, 2002.

[42] J. Haroon et al., "Comparison of the Reactivity Effects Calculated by DRAGON and Serpent for a PHWR 37-Element Fuel Bundle," *Journal of Nuclear Engineering and Radiation Science,* vol. 3, no. 1, p. 011011, 2016.

[43] CANTEACH, "Nuclear Physics and Reactor Theory," Module 12, 1996.

[44] J. J. Whitlock, "Reduction of The Coolant Void Reactivity Effect in a CANDU Lattice Cell," PhD Dissertation, Hamilton: McMaster University, 1995.

[45] W. M. Stacey, "Nuclear Reactor Physics," 2nd Edition ed., Winheim: WILEY-VCH Verlag GmbH & Co, 2007.

[46] R. Roy et al., "Modelling of CANDU Reactivity Control Devices with the Lattice Code DRAGON," *Annals of Nuclear Energy,* vol. 21, no. 2, pp. 115-132, 1994.

[47] B. J. Min et al., "WIMS-AECL/MULTICELL Calculations with SPH for Wolsong-1 Reactivity Devices," in *Proceedings of the Korean Nuclear Society Spring Meeting*, Cheju, 1996.

[48] B. J. Min and J. V. Donnelly, "Validation of WIMS-AECL Reactivity Device Calculations for CANDU Reactor," Korea Atomic Energy Research Institute, Daeduk, 1997.

[49] R. S. Davis, "Qualification of DRAGON for Reactivity Device Calculations in the Industry Standard Toolset," in *25th Annual Conference of the Canadian Nuclear Society*, Toronto, 2004.

[50] M. Ovanes and J. V. Donnelly, "Validation of 3-Dimensional Neutron-Transport Calculations of CANDU Reactivity Devices," in *Canadian Nuclear Society 21st Nuclear Simulation Symposium*, Ottawa, 2000.

[51] M. Dahmani et al., "WIMS-IST/DRAGON-IST Side-Step Calculation of Reactivity Device and Structural Material Incremental Cross Sections for Wolsong NPP Unit 1," in *23rd CNS Nuclear Simulation Symposium*, Ottawa, 2008.

[52] R. Le Tellier et al., "The Implementation of a 3D Characteristics Solver for the Generation of Incremental Cross Sections for Reactivity Devices in a CANDU Reactor," in *PHYSOR-2006 - ANS Topical Meeting on Reactor Physics*, Vancouver, 2006.

[53] International Atomic Energy Agency, "WIMS-D Library Update," STI/PUB/1264, Vienna, 2007.

[54] M. Dahmani et al., "Modeling Reactivity Devices for Advanced CANDU Reactors using the Code DRAGON," *Annals of Nuclear Energy,* vol. 35, pp. 804-812, 2008.

[55] W. J. Garland, Editor-in-Chief, "The Essential CANDU, A Text book on the CANDU Nuclear Power Technology," Chapter 18, University Network of Excellence in Nuclear Engineering, ISBN 0-9730040, 2016.

[56] P. Reid et al., "The ACR-1000 Fuel Bundle Design," in *Proceedings of the 10th International Conference on CANDU Fuel*, Mississauga, 2008.

[57] P. G. Boczar and J. D. Sullivan, "Low Void Reactivity Fuel," in *Proceedings of the 25th Annual Conference of the Canadian Nuclear Society*, Toronto, 2004.

[58] M. Ovanes et al., "Reactor Physics Innovations in ACR-700 Design for Next CANDU Generation," in *Proceedings of the 23th Annual Conference of the Canadian Nuclear Society*, Toronto, 2002.

[59] J. Pencer et al., "Comparison of WIMS-AECL/DRAGON/RFSP and MCNP Results with ZED-2 Measurements for Control Device Worth and Reactor Kinetics," in *PHYSOR 2010 - Advances in Reactor Physics to Power the Nuclear Renaissance*, Pittsburgh, 2010.

[60] P. G. Boczar et al., "Recovered Uranium in CANDU - A Strategic Opportunity," in *Proceedings of International Nuclear Conference and Exhibition*, Toronto, 1993.

[61] P. G. Boczar et al., "Considerations in Recycling Used Natural Uranium Fuel from CANDU Reactors in Canada," in *Proceedings of the 31st Annual Conference of the Canadian Nuclear Society*, Montreal, 2010.

[62] D. H. Kim and H. Choi, "Composition Heterogeneity Analysis for Direct Use of Spent Pressurized Water Reactor Fuel in CANDU Reactors (DUPIC) - I:

Deterministic Analysis," *Nuclear Science and Engineering,* vol. 137, pp. 23-37, 2001.

[63] W. I. Ko and H. D. Kim, "Analysis of Nuclear Proliferation Resistance of DUPIC Fuel Cycle," *Nuclear Science and Technology,* vol. 38, no. 9, pp. 757-765, 2001.

[64] C. M. Cottrell et al., "Natural Uranium Equivalent (NUE) Fuel: Full Core Use of Recycled Uranium and Depleted Uranium in CANDU Reactors," in *Proceedings of the 21st International Conference on Nuclear Engineering*, Chengdu, 2013.

[65] A. C. Radut et al., "Assessment of NUE Fuel Element Performance in Normal Operating Conditions," *Nuclear Research and Development,* vol. 51, no. 33, 2018.

[66] L. Q. Yuan et al., "Investigation of Critical Heat Flux for Plutonium-Based Mixed Oxide Advanced Fuel Bundle Design," *Nuclear Engineering and Radiation Science,* vol. 8, no. 1, 2022.

[67] Y. Akter et al., "Assessment of the Burnup Characteristics of UO_2 and MOX Fuel in the Mixed Solid and Annular Rod Configuration," *Nuclear Engineering and Design,* vol. 381, 2021.

[68] OECD/NEA and International Atomic Energy Agency, "Uranium 2016: Resources, Production and Demand," Organisation for Economic Co-Operation And Development, Paris, 2016.

[69] P. G. Boczar et al., "Qualification of Reactor Physics Toolset for a Thorium-Fuelled CANDU Reactor," in *Proceedings of the 18th International Conference on Nuclear Engineering*, Xi'an, 2010.

[70] A. V. Colton et al., "Evaluation of Uranium-Based Fuels Augmented by Low Levels of Thorium for Near-Term Implementation in Pressure Tube Heavy Water Reactors," *Nuclear Science and Engineering,* vol. 186, pp. 48-65, 2017.

[71] A. V. Colton and B. P. Bromley, "Full-Core Evaluation of Uranium-Based Fuels Augmented with Small Amounts of Thorium in Pressure Tube Heavy Water Reactors," *Nuclear Technology,* vol. 196, pp. 1-12, 2016.

[72] B. Hyland and B. Gihm, "Scenarios for the Transmutation of Actinides in CANDU Reactors," *Nuclear Engineering and Design,* vol. 241, pp. 4794-4802, 2011.

[73] A. C. Morreale et al., "The Effects of Fuel Burnup on Incremental Cross Sections in Actinide Fuels in CANDU Reactors," in *33rd Annual Conference of the Canadian Nuclear Society*, Saskatoon, 2011.

[74] A. C. Morreale et al., "The Effects of Actinide Based Fuels on Incremental Cross Sections in a CANDU Reactor," in *International Conference on Mathematics and Computational Methods Applied to Nuclear Science and Engineering*, Rio de Janeiro, 2011.

[75] A. Hebert and G. Marleau, "Generalization of the Stamm'ler Method for the Selfshielding of Resonant Isotopes in Arbitrary Geometries," *Nuclear Science and Engineering,* vol. 108, pp. 230-239, 2003.

[76] T. Courau and G. Marleau, "Perturbation Theory for Lattice Cell Calculations," *Nuclear Science and Engineering,* vol. 143, pp. 19-32, 2003.

[77] C. Carre, "Feasibility Study of Recycling Uranium Retreatment," Ecole Polytechnique De Montreal, Montreal, 2011.

[78] D. Cho et al., "Sensitivity of Physics Parameters for Establishment of a Burned CANDU Full-Core Model for Decommissioning Waste Characterization," *Journal of Nuclear Science and Technology,* vol. 48, no. 2, pp. 215-226, 2012.

[79] A. Hebert et al., "A User's Guide for DONJON Version 5," Ecole Polytechnique de Montreal, Montreal, 2022.